

SANDIA REPORT

SAND2016-10094
Unlimited Release
Printed October 2016

Advanced WEC Dynamics & Controls FY16 Testing Report

Ryan G. Coe, Giorgio Bacelli, David Patterson, David G. Wilson

Prepared by
Sandia National Laboratories
Albuquerque, New Mexico 87185 and Livermore, California 94550

Sandia National Laboratories is a multi-mission laboratory managed and operated by Sandia Corporation, a wholly owned subsidiary of Lockheed Martin Corporation, for the U.S. Department of Energy's National Nuclear Security Administration under contract DE-AC04-94AL85000.

Approved for public release; further dissemination unlimited.



Sandia National Laboratories

Issued by Sandia National Laboratories, operated for the United States Department of Energy by Sandia Corporation.

NOTICE: This report was prepared as an account of work sponsored by an agency of the United States Government. Neither the United States Government, nor any agency thereof, nor any of their employees, nor any of their contractors, subcontractors, or their employees, make any warranty, express or implied, or assume any legal liability or responsibility for the accuracy, completeness, or usefulness of any information, apparatus, product, or process disclosed, or represent that its use would not infringe privately owned rights. Reference herein to any specific commercial product, process, or service by trade name, trademark, manufacturer, or otherwise, does not necessarily constitute or imply its endorsement, recommendation, or favoring by the United States Government, any agency thereof, or any of their contractors or subcontractors. The views and opinions expressed herein do not necessarily state or reflect those of the United States Government, any agency thereof, or any of their contractors.

Printed in the United States of America. This report has been reproduced directly from the best available copy.

Available to DOE and DOE contractors from
U.S. Department of Energy
Office of Scientific and Technical Information
P.O. Box 62
Oak Ridge, TN 37831

Telephone: (865) 576-8401
Facsimile: (865) 576-5728
E-Mail: reports@adonis.osti.gov
Online ordering: <http://www.osti.gov/bridge>

Available to the public from
U.S. Department of Commerce
National Technical Information Service
5285 Port Royal Rd
Springfield, VA 22161

Telephone: (800) 553-6847
Facsimile: (703) 605-6900
E-Mail: orders@ntis.fedworld.gov
Online ordering: <http://www.ntis.gov/help/ordermethods.asp?loc=7-4-0#online>



Advanced WEC Dynamics & Controls FY16 Testing Report

Ryan G. Coe
Sandia National Laboratories
P.O. Box 5800, MS 1124
Albuquerque, NM 87185-9999
rcoe@sandia.gov

David Patterson
Sandia National Laboratories
P.O. Box 5800, MS 1124
Albuquerque, NM 87185-9999
dcpatte@sandia.gov

Giorgio Bacelli
Sandia National Laboratories
P.O. Box 5800, MS 1124
Albuquerque, NM 87185-9999
gbacell@sandia.gov

David G. Wilson
Sandia National Laboratories
P.O. Box 5800, MS 1152
Albuquerque, NM 87185-9999
dwilso@sandia.gov

Acknowledgment

This study was supported by the Department of Energy (DOE), Office of Energy Efficiency and Renewable Energy (EERE), Wind and Water Power Technologies Office (WWPTO). Sandia National Laboratories is a multi-mission laboratory managed and operated by Sandia Corporation, a wholly owned subsidiary of Lockheed Martin Corporation, for the U.S. Department of Energy's National Nuclear Security Administration under contract DE-AC04-94AL85000. Dave Newborn and Miguel Quintero from the Naval Surface Warfare Center, Carderock Division assisted in test design, planning and execution. Kevin Dullea (Sandia National Labs) led the mechanical design and fabrication of testing hardware. Mark Monda, Steven Spencer, Tim Blada, Pat Barney, Mike Kuehl and Dennis Wilder of Sandia supported hardware design, fabrication and bench-testing. Osama Abdelkhalik (Michigan Tech.), Rush Robinett (Michigan Tech.) and Umesh Korde (South Dakota School of Mines) performed related control design research. ATA Engineering performed experimental and numerical structural dynamics testing of the MASK basin bridge. Chris Sharp, a PhD student from Oregon State University, assisted in control performance comparison work.

Contents

- Executive Summary** **13**

- 1 Background** **15**
 - 1.1 Introduction 15
 - 1.2 Experimental setup & Hardware 15
 - 1.2.1 Test device 15
 - 1.2.2 Wave tank 17
 - 1.2.3 Wave Maker 18
 - 1.2.4 Sensors & data acquisition 26
 - 1.2.4.1 Data acquisition & Control 26
 - 1.2.4.2 Device actuator 28
 - 1.2.4.3 Load cells 28
 - 1.2.4.4 Pressure sensors 31
 - 1.2.4.5 Structural vibration sensors 32
 - 1.2.4.6 NaturalPoint tracking 34
 - 1.2.4.7 Video recordings 34
 - 1.2.4.8 Wave sensors 35
 - 1.3 Experimental Design 37
 - 1.3.1 Experiment types 38
 - 1.3.2 Input signals 38
 - 1.4 Data synthesis 40

2	System Identification	43
2.1	Radiation model	43
2.1.1	Nonparametric models	43
2.1.1.1	Input force: White multisine	46
2.1.1.2	Input force: Pink multisine	50
2.1.1.3	Input force: sinusoidal	53
2.1.2	Parametric models	54
2.1.2.1	Identification using periodic signals	54
2.1.2.2	Identification using non-periodic signals	55
2.2	Excitation model	59
2.2.1	Diffraction tests with multisines	59
2.2.2	Diffraction tests with monochromatic sinusoids	59
2.2.3	Model separation from forced response tests	60
2.3	WEC model	61
2.3.1	Radiation / diffraction model validation	61
2.3.2	MISO system ID (2-input/1-output)	62
2.3.2.1	MISO, wave elevation / actuator	63
2.3.2.2	MISO, pressure / actuator	64
2.4	Conclusions	65
3	Control performance comparison	67
	References	72
	Appendix	
A	Testing Log & Procedures	73

A.1	Test Log	73
A.2	Procedures	78
A.2.1	Test procedures	78
A.2.2	Entrance criteria	78
A.2.3	Exit criteria	78
A.2.4	General daily procedures	79
A.3	Safety analysis	79
B	Sensors Locations and Calibrations	81
C	Structural Dynamics Report	89

List of Figures

1.1	Test device diagram.	16
1.2	Exploded view of float components.	19
1.3	Photo during float construction showing internal plywood skeleton, foam and tubing for pressure sensors.....	20
1.4	Float during ballasting. Lead ingots partially installed in outer cavities. Plate weights installed on float floor and secured on threaded rods with wing nuts/washers.	21
1.5	Test device structure from CAD rendering.	21
1.6	Test device and hardware installed in MASK basin.	22
1.7	Top view schematic of bridge and MASK basin.....	23
1.8	Side view schematic of bridge and MASK basin.	24
1.9	MASK reference orientation.	24
1.10	General view of new segmented wavemaker in MASK Wavemaking Facility. Paddles are highlighted in red and the control cabinets are highlighted in bright blue. .	25
1.11	Mask wave maker diagram.	25
1.12	Sensor and DAQ layout (sensor and DAQ locations are not to scale). (Markers for “BP#” indicate locations of “bridge-probe” acoustic wave sensors.)	26
1.13	Layout of collection systems and triggering mechanisms.	27
1.14	Layout of SNL data acquisition, hardware and cabling along MASK bridge.	28
1.15	Layout of sensors on weldment.	29
1.16	Pitch lock-out load cell installed on float.	30
1.17	The fit for each load cell is shown as the dashed line and the points of calibration are the circular markers. The load applied was measured in newtons and the output of the devices was measured in volts.	30

1.18	Pressure sensor locations and numbering convention. A red sensor denotes a Transducers Direct TDH-40, a blue sensor denotes an Omega PX-459, and a green sensor denotes an Amphenol NPI-19B. The larger grey sensors denote locations of the slam panels, sensors designed to measure slamming impacts on the device.	31
1.19	Pressure sensor ports on hull of device.	32
1.20	Pressure sensor calibrations: factory calibration readings are shown as dots, hydrostatic pressures (calculated) are shown as lines. In (a), PT02 is a faulty sensor which reads close to zero.	33
1.21	Location of triaxial accelerometer at base of PTO tower.	34
1.22	NaturalPoint optical tracking probes on float.	35
1.23	Screen shot for testing video recordings.	35
1.24	Wave sensor and device locations within MASK basin. See Table B.1 for tabulated locations.	36
1.25	Wave sensor arrays used in testing.	37
1.26	Spectral density of pseudo-random (2 hour repeat, 30 minute wave) and periodic (5 minute repeat, 15 minute wave) Bretschneider ($H_s = 0.192$ m, $T_p = 4.00$ s) wave realizations.	41
2.1	Spectra of the input force: white (flat) multisine.	44
2.2	Spectra of the input force: “pink” multisine.	44
2.3	Spectra of the buoy velocity for “white” multisine input force.	45
2.4	Spectra of the buoy velocity for “pink” multisine input force.	45
2.5	Magnitude and phase of intrinsic impedance for a white multisine input force. The estimated linear friction is $B_f = 460$ Ns/m.	46
2.6	Real and Imaginary part of intrinsic impedance for a white multisine input force. The estimated linear friction is $B_f = 460$ Ns/m. It is interesting to verify from the plot of the imaginary part that the resonance frequency is approximately 0.63 Hz ($\text{Im}[Z_i(\omega)]_{\omega=\omega_{res}} = 0$).	47
2.7	Estimated radiation damping and added mass. The input force is a white multisine (Figure 2.1) and the estimated linear friction is $B_f = 460$ Ns/m	47
2.8	Phase and magnitude, input signal is white multisine, actuator gain 1.5 (50% greater than in Figure 2.8). Estimated linear damping is $B_f = 320$ Ns/m.	48

2.9	Phase and magnitude, input signal is white multisine, actuator gain 1.5 (50% greater than in Figure 2.9). Estimated linear damping is $B_f = 320$ Ns/m.	48
2.10	Radiation damping and added mass, input signal is white multisine, actuator gain 1.5 (50% greater than in Figure 2.10). Estimated linear friction is $B_f = 320$ Ns/m.	49
2.11	Magnitude and phase of intrinsic impedance for a pink multisine input force. The estimated linear friction is $B_f = 460$ Ns/m.	50
2.12	Real and Imaginary part of intrinsic impedance for a pink multisine input force. The estimated linear friction is $B_f = 460$ Ns/m. It is interesting to verify from the plot of the imaginary part that the resonance frequency is approximately 0.63 Hz ($\text{Im}[Z_i(\omega)]_{\omega=\omega_{res}} = 0$).	50
2.13	Estimated radiation damping and added mass. The input force is a pink multisine (Figure 2.1) and the estimated linear friction is $B_f = 460$ Ns/m	51
2.14	Phase and magnitude, input signal is pink multisine, actuator gain 1.5 (50% greater than in Figure 2.11). Estimated linear damping is $B_f = 320$ Ns/m.	51
2.15	Phase and magnitude, input signal is pink multisine, actuator gain 1.5 (50% greater than in Figure 2.12). Estimated linear damping is $B_f = 320$ Ns/m.	52
2.16	Radiation damping and added mass, input signal is pink multisine, actuator gain 1.5 (50% greater than in Figure 2.13). Estimated linear friction is $B_f = 320$ Ns/m.	52
2.17	Intrinsic impedance calculated using sinusoidal input signals.	53
2.18	Added mass and damping calculated using sinusoidal signal of different amplitudes.	53
2.19	Added mass and damping. The plot shows the smoothed experimental data, the parametric model and the data obtained from WAMIT.	54
2.20	Frequency response of the intrinsic impedance, for both the parametric and non-parametric models. Both curves have been obtained from experimental data.	55
2.21	Periodic radiation model validation comparison: measured and simulated time series of the heave velocity ($1 - \text{NRMSE} = 89.3\%$).	55
2.22	Spectral components of the actuator force.	56
2.23	Spectral components of the heave velocity.	56
2.24	Block diagram describing “black box” approach for identification of the inverse intrinsic impedance.	56
2.25	Pole-zero map of the parametric model for the inverse intrinsic impedance.	57
2.26	Real and imaginary part of the inverse intrinsic impedance.	57

2.27	Magnitude and phase of the inverse intrinsic impedance.	58
2.28	Non-periodic radiation model validation comparison: Comparison of simulated and measured velocities (1 – NRMSE = 91.2%).	58
2.29	Pink spectra of wave elevation. Note: very good repeatability and no spectrum leakage.	60
2.30	Excitation force FRFs calculated using signals from multiple waveprobes (“Staff1,” “Staff2,” . . .).	60
2.31	Excitation FRFs using sinusoidal waves compared to pink multisine and WAMIT.	61
2.32	Comparison of excitation FRFs obtained using WAMIT, dedicated diffraction tests (“Diffraction”) and separation from radiation and dynamic tests (“Dynamic”).	62
2.33	Block diagram of the WEC base on radiation/diffraction model. The wave elevation is denoted by η , the actuator force is F_a and the velocity is v	62
2.34	Radiation/diffraction model validation: time series detail of measured (experimental) velocity compared to simulated velocity (1 – NRMSE = 71.6%).	63
2.35	Block diagram for the 2-input, 1-output model structure: force and wave elevation are the inputs, velocity is the output.	63
2.36	Bode plot of the 2-Input, 1-Output model for the WEC. The wave elevation is measured in inches and the force in kN.	64
2.37	Comparison of measured and simulated velocities for the MISO, elevation / actuator model (1 – NRMSE = 67%).	64
2.38	Block diagram for the 2-input, 1-output model structure: force and pressure are the inputs, velocity is the output.	65
2.39	Bode plot of the 2-input, 1-output model for the WEC. The unit of the force is kN and of the pressure is kPa.	65
2.40	Comparison of measured and simulated velocities for the MISO, pressure / actuator model (1 – NRMSE = 87%).	66

List of Tables

1.1	Model-scale WEC physical parameters.	16
1.2	Idealized ocean spectra (Bretschneider) tested.	39
2.1	Model validation performance comparison.	66
3.1	List of the 17 irregular sea-states simulated to characterize controller performance for Newport, OR (NDBC 46050) deployment [1].	68
3.2	Performance comparison of control strategies in irregular waves.	70
A.1	Wave tank testing log.	74
A.2	Failure modes effects analysis from the Advanced WEC Dynamics and Controls safety procedures.	80
B.1	Wave sensor locations within MASK basin.	81
B.2	General wave sensor calibration factors.	84
B.3	WaveWire sensor calibration factors.	85
B.4	Locations of the Pressure Sensors with respect to the center of the base.	86
B.5	Pressure transducer calibration curves.	87
B.6	Calibration curves for test load cells.	87

Executive Summary

A model-scale wave tank test was conducted in the interest of improving control systems design of wave energy converters (WECs). The success of most control strategies is based directly upon the availability of a reduced-order model with the ability to capture the dynamics of the system with sufficient accuracy. For this reason, the test described in this report, which is the first in a series of planned tests on WEC controls, focused on system identification (system ID) and model validation.

In this study, two high-level categories of system ID approaches were utilized to obtain reduced-order numerical models for the data collected in wave tank testing: (1) “traditional” wave tank testing, based on monochromatic tests in the diffraction (excitation) and radiation regimes and (2) approaches based more generally on practices used across a wide range of engineering disciplines, which employ broad-banded periodic excitation signals. The comparison of these approaches shows that general system ID approaches have a number of advantages over the more traditional wave tank testing practices. The general system ID approach produces richer models with higher frequency resolution as well as estimates of model uncertainty and indications of nonlinearities in the system. In addition, these general system ID approaches can be executed in much less time: a model produced with 10 minutes of data via this general broadband approach will likely be more accurate and have higher resolution than a model constructed from an entire day’s worth of testing via a monochromatic (“traditional”) wave tank approach. Additionally, this testing campaign focused on the development of methods to support the full scale modeling and control of WECs in open-ocean environments. In particular, testing and analysis procedures to obtain a WEC’s excitation model without the need for dedicated diffraction testing (in which the device must be locked in place) have been studied and applied. This study also considers the problem of designing and implementing real-time control in an open-ocean environment with limited sensor availability and quality. Initial results show that pressure measurements may simplify modeling procedures in addition to improving accuracy of the dynamic model and state estimation process when compared with wave elevation. These developments will be critical in realizing the implementation of advanced control on full-scale WECs.

Validation tests of the best models produce by this study show 85+% agreement with the experimental data. These models are detailed in this report for use by the general research community. In addition to providing a demonstration of the utility of the system ID approaches, the results of this round of wave tank testing will support ongoing work to implement and study advanced WEC control on large scale, real-time and realistic WEC systems.

Chapter 1 of this test report covers test setup, experimental cases. Data analysis and conclusions are covered in Chapter 2. Using one of the models developed from the wave tank testing data, a numerical study on control strategy performance was conducted. A summary of this comparison is presented in Chapter 3. Full datasets from the testing are available at <https://mhkdr.openei.org/submissions/151> for further use by researchers and WEC developers.

Chapter 1

Background

1.1 Introduction

Numerous studies have shown that advanced control of a wave energy converter's (WECs) power take off (PTO) can provide significant increases (on the order of 200-300%) in WEC energy absorption [2, 3]. Transitioning these control approaches from simplified paper studies to application in full-scale devices remains an open and extremely challenging problem that will be central to creating economically competitive WECs and delivering clean renewable energy to the US electrical grid. The Advanced WEC Dynamics and Controls project is targeted on assisting WEC developers to apply novel control systems for their devices, thus achieving major increases in performance and economic viability.

This report focuses on the challenge of producing reduced-order WEC dynamics models based on empirical testing for use in control design, including state estimation. A model-scale WEC was designed and fabricated for use in studies to advance the state-of-the-art in WEC controls. Tests were performed to provide data for system identification (system ID) and model validation. This Chapter summarizes the experimental design and testing procedures.

1.2 Experimental setup & Hardware

1.2.1 Test device

A model-scale WEC device was designed to provide dynamics ranging from mostly-linear in a single degree-of-freedom to increasingly nonlinear in multiple degrees-of-freedom [4]. This device was designed to be 1/17th a full-scale equivalent WEC. A diagram of the device is shown in Figure 1.1; pertinent parameters for this device are listed in Table 1.1. Note that two rigid-body masses are given in Table 1.1: m_f is the rigid-body mass of the float alone while m_3 is the rigid-body mass of the float and actuator slider which sits on top of it. When considering the rigid-body inertia of the body in heave, the later of these (m_3) is the pertinent value. The mass of displaced water, with the system fully assembled, is also m_3 . This WEC device was designed not towards development of an equivalent full-scale commercial WEC, but instead as a "test bed" for the study

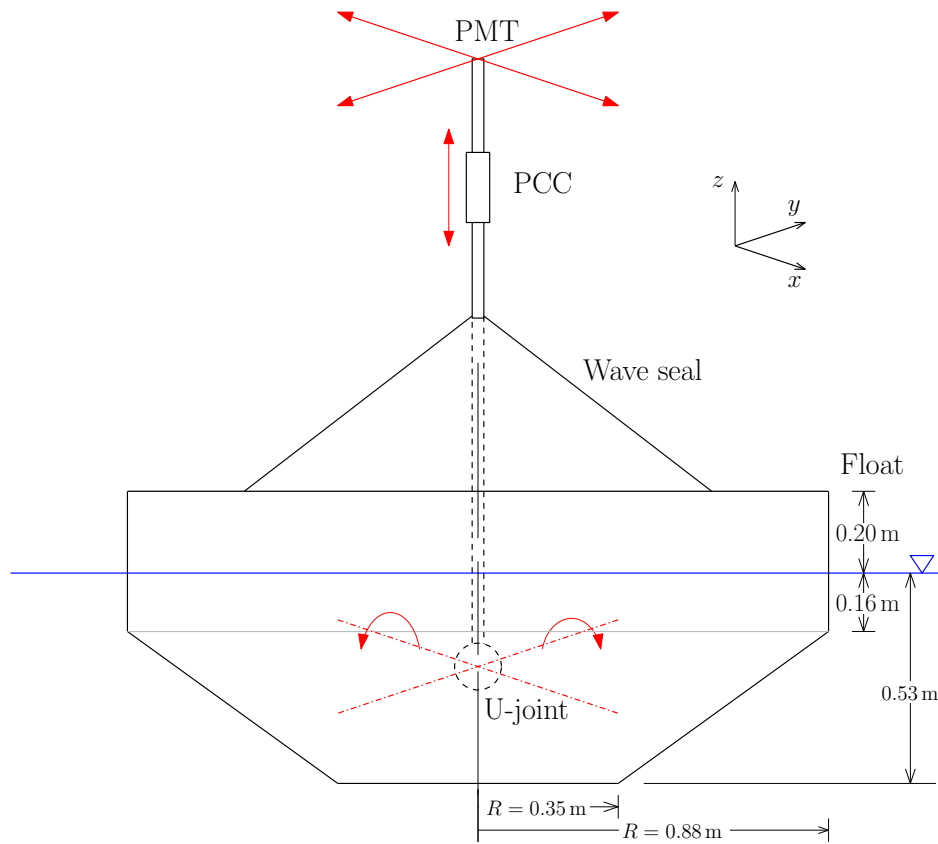


Figure 1.1: Test device diagram.

of WEC dynamics modeling and control. The multiple degrees of freedom can be locked and unlocked to provide a system means of considering configurations with a range of complexities. This device can also be deballasted to provide a system in which the hydrostatics of the device are more strongly nonlinear.

The float portion of the device (the floating body) is constructed of a marine-grade plywood skeleton with foam to form the remainder of the structure. Figure 1.2 shows an exploded view of the float with its different foam and plywood components. The plywood sections were cut to

Table 1.1: Model-scale WEC physical parameters.

Parameter	Value
Rigid-body mass (float only), m_f (kg)	660
Rigid-body mass (float & slider), m_3 (kg)	858
Displaced volume, ∇ (m^3)	0.858
Float radius, r (m)	0.88
Float draft, T (m)	0.53
Water density, ρ (kg/m^3)	1000
Water depth, h (m)	6.1

shape with a water jet to include mortise and tendon style joints. Figure 1.3 shows the float during the fabrication process. Without ballast, the float has a mass of 160 kg. To bring the device to its design waterline, 500 kg of ballast, in the form of twenty-four 14.5 kg lead ingots and thirty-three 4.5 kg (10 lb) plate weights, were added. As shown in Figure 1.4, the lead ingots were housed in twelve cavities around the perimeter of the float. Plate weights were located at the bottom of the float. The ballast weights were arranged so as to counter the asymmetric distribution of sensors and thus achieve a symmetric trim (i.e. no static heel or trim) for the float.

A CAD model rendering of the full device is shown in Figure 1.5. The mechanisms that allow for the float to translate in all degrees of freedom are located above the water and suspended from the gantry bridge which spans the basin (see Section 1.2.2). This removes the need for waterproofing/sealing of key components and allows for easy access to perform tuning and troubleshooting. The PTO tower, which houses a set of roller bearings, supports the actuator that acts as the device's power take-off (PTO) in heave. A planar motion table (PMT), which suspends the entire PTO tower on a set of horizontally oriented roller bearings, allows for the device to move in surge. Figure 1.6 shows the final installation of the test device in the MASK basin.

The model-scale WEC shown in Figure 1.5 and 1.6 was designed to move in three degrees-of-freedom: heave, surge and pitch. For this study, most of the testing focused only on single degree-of-freedom (heave) motion. (However, some initial testing was performed with pitch and/or surge motion.) As shown in Figures 1.5 and 1.6, a series of "lock-out" bars were used to restrict the pitch motion of the float. Similarly, a bolted connection was used to lock-out surge. For diffraction style tests, the heave degree-of-freedom mechanically locked out, removing the actuator from the system. In some tests, these lock-out mechanisms incorporated load cells to measure the forces required to restrict the device's motion (see Section 1.2.4.3 for more details).

1.2.2 Wave tank

All testing was conducted in the Maneuvering and Seakeeping basin (MASK) at Carderock Division, Naval Surface Warfare Center located in Bethesda, Maryland. The MASK is an indoor basin with an overall length of 110 m (360 ft), a width of 73 m (240 ft) and a depth of 6.1 m (20 ft) except for a 10.7 m (35 ft) deep trench that is 15.2 m (50 ft) wide and parallel to the long side of the basin (on the south side). The basin is spanned by a 115 m (376 ft) bridge. The bridge is supported on a rail system that permits it to transverse to the center of the basin width as well as to rotate up to 45° from the centerline as seen in Figure 1.7 and 1.8. (Figure 1.7 and 1.8 do not include the physical update of this wavemaker system, but a drawing of the new paddle layout can be seen in Figure 1.10.) The MASK Carriage is suspended beneath the bridge and can travel along the rails by the rollers and drive system. There is an arresting gear to prevent the carriage from hitting the end stops and this limits the travel along the bridge. The carriage has 6 × 10 ft moon bay in the center, which allows for models and instrumentation to be mounted. Along the two edges of the basin opposite of the wavemakers are artificial beaches with a 12° slope. The beaches are composed of seven concrete layers and are effective in mitigating the mass flux of water back into the tank during wave generation. The hydrodynamic properties of the beaches are detailed in Brownell [5].

The reference frame used for the MASK basin is illustrated in Figure 1.9. Its operational origin is located at the interior intersection of the northwest and northeast walls and vertically at the nominal 6.1 m water level. The positive x -axis is aligned along the shorter northwest wall and the positive y -axis along the longer northeast wall. Waves propagating parallel with the x -axis (toward the long beach) are defined as having a mean wave direction, β_0 , of 0° and waves propagating parallel with the y -axis as 90° . This convention defines the wave direction as the direction the waves are traveling toward.

1.2.3 Wave Maker

The MASK wavemaker system consists of 216 paddles. There are 108 paddles along the North edge of the basin ($x = 0$ in Figure 1.9), 60 paddles in a ninety degree arc, and 48 paddles along the West edge of the basin ($y = 0$ in Figure 1.9). The paddles are grouped into sets of eight paddles, with each set controlled by a single control cabinet. The 27 control cabinets are then joined via three marshaling cabinets, and ultimately the marshaling cabinets are connected to the main control station at the second floor of the MASK control room. Figure 1.10 shows an overview schematic of the wave maker and paddle layout.

A more up-close diagram of the wave makers is shown in Figure 1.11. The paddles have a hinge depth of 2.5 m (8.2 ft) and a pitch (centerline to centerline spacing) of 0.658 m (25.9 in.). The wavemaker system is a dry back, force feedback system. The paddles are moved using hydrostatic compensation with air tanks and bellows and with sectors attached to the wavemakers with an A-frame type structure. Each sector has a drive belt which runs along its topside. The drive belt runs through a pulley box powered with an encoder controlled motor. The motor is used to control the real-time motions of the paddle. The force feedback of the paddle is provided via a force transducer mounted at the bellows and sector interface to the paddle. The wavemaker is controlled via Edinburgh Designs Limited (EDL) runtime software located on the main control computer. The wavemaking system can output data at rates given by a power of 2. For this study, paddle data was collected at 32 Hz.

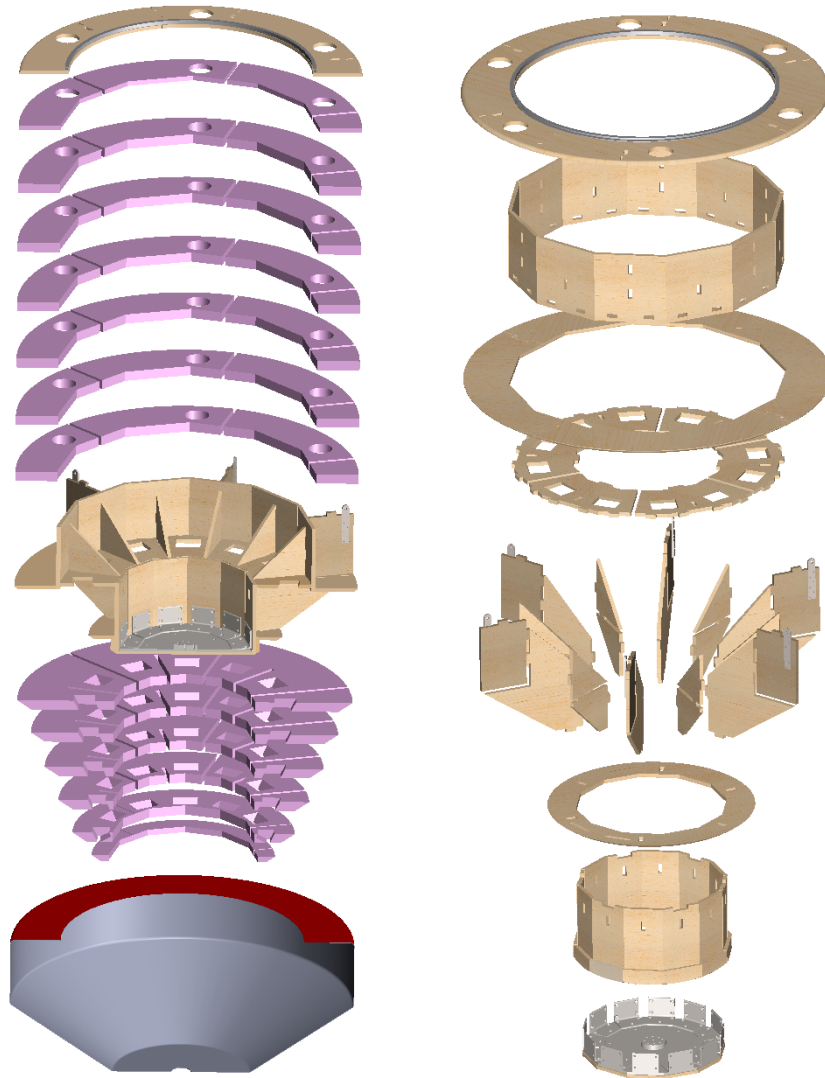


Figure 1.2: Exploded view of float components.



Figure 1.3: Photo during float construction showing internal plywood skeleton, foam and tubing for pressure sensors.



Figure 1.4: Float during ballasting. Lead ingots partially installed in outer cavities. Plate weights installed on float floor and secured on threaded rods with wing nuts/washers.

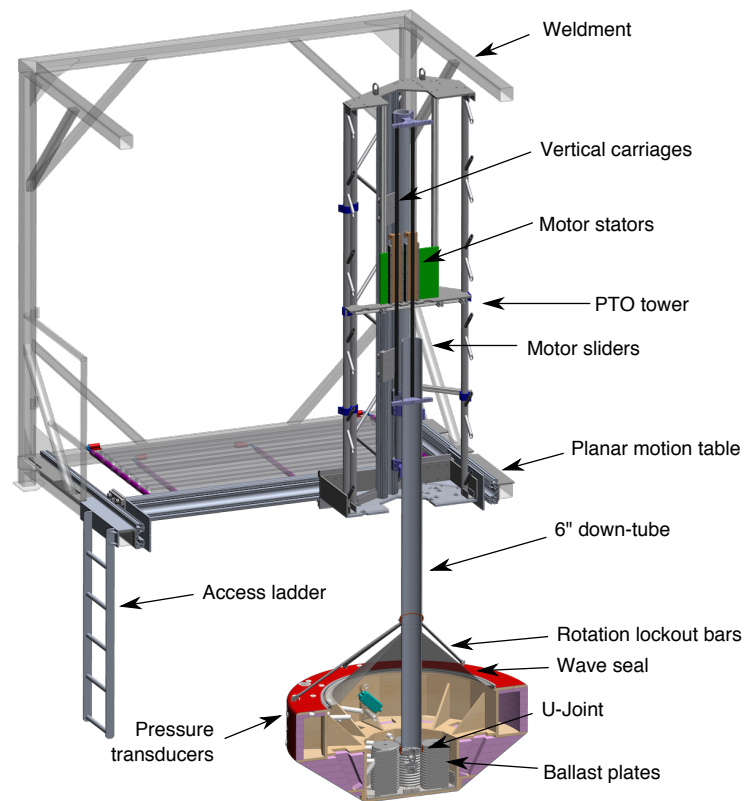


Figure 1.5: Test device structure from CAD rendering.

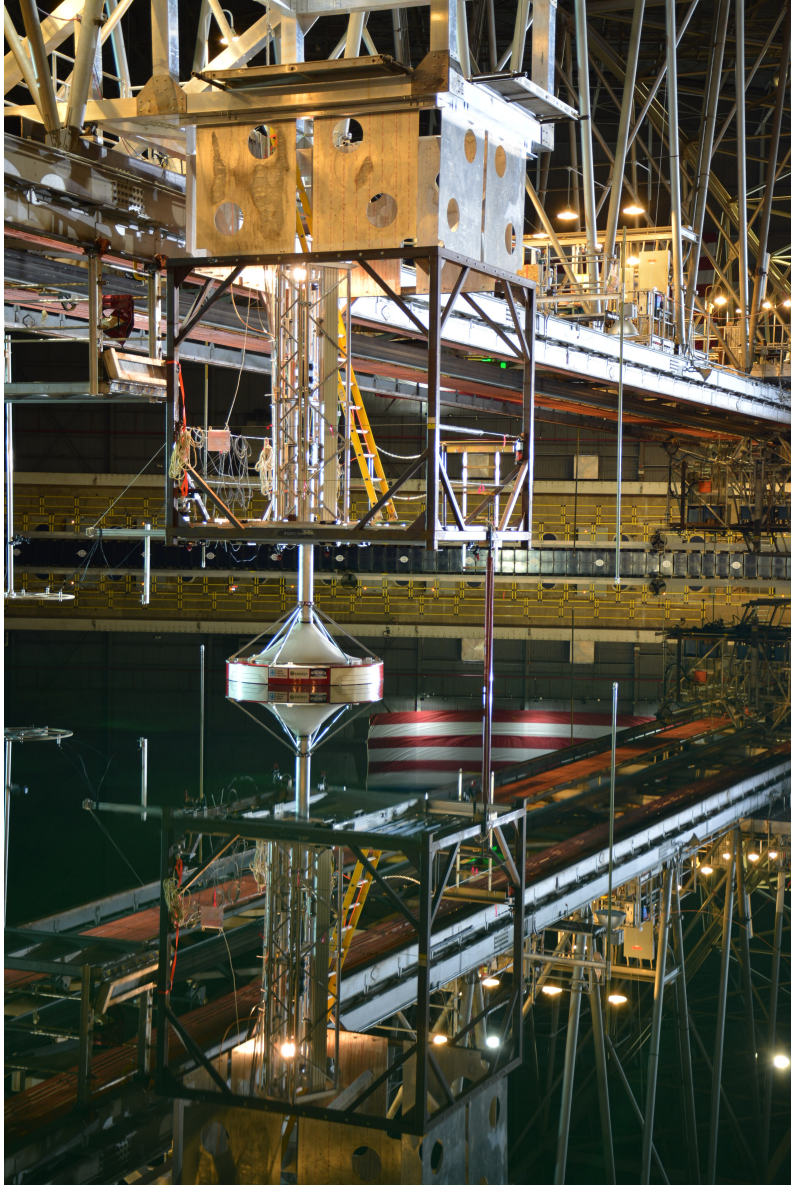


Figure 1.6: Test device and hardware installed in MASK basin.

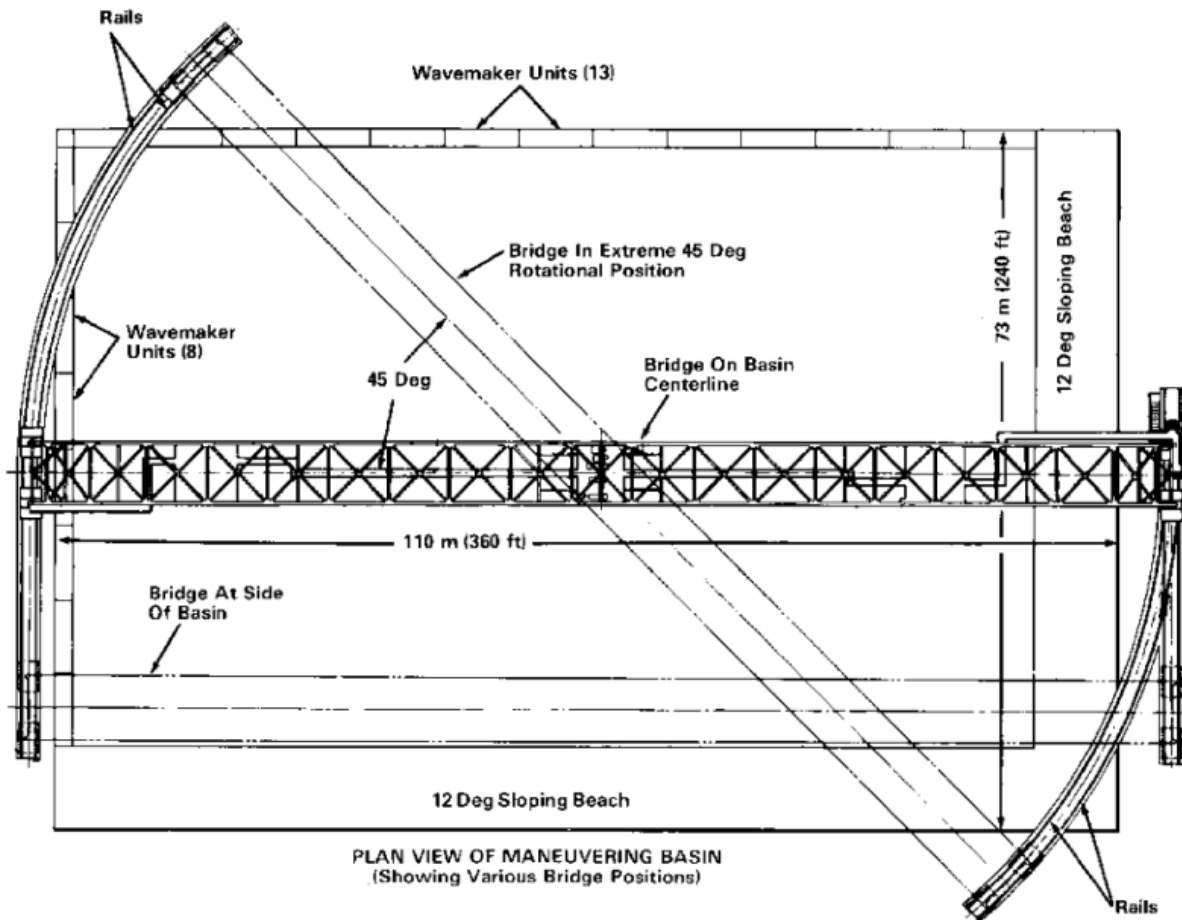


Figure 1.7: Top view schematic of bridge and MASK basin.

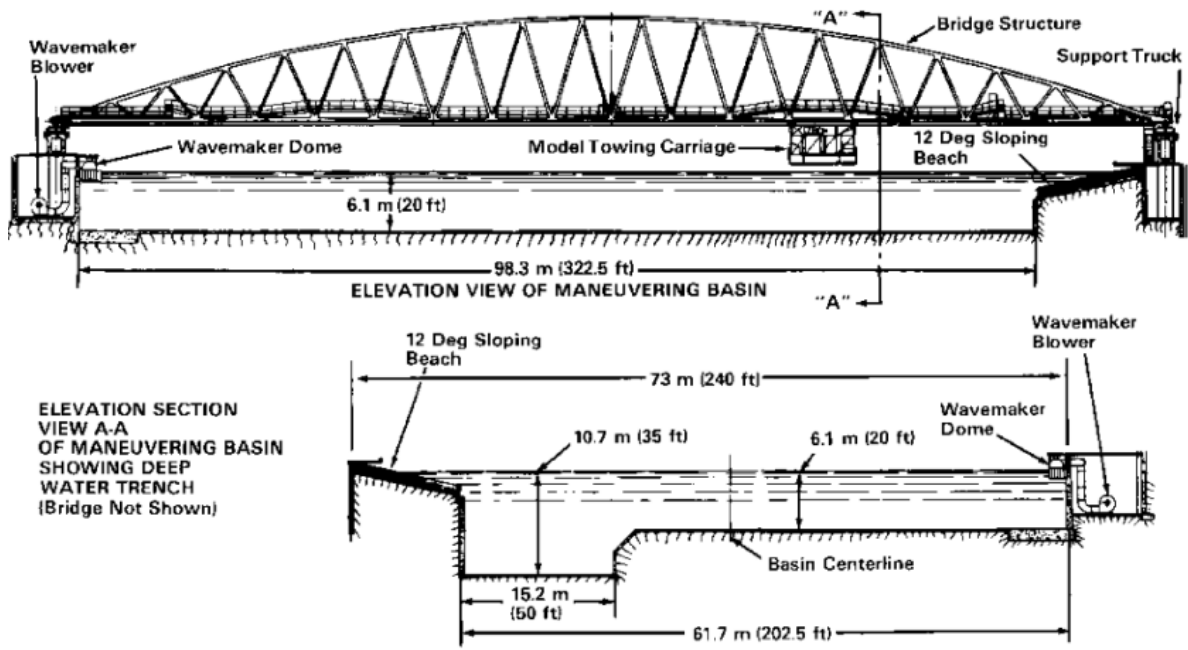


Figure 1.8: Side view schematic of bridge and MASK basin.

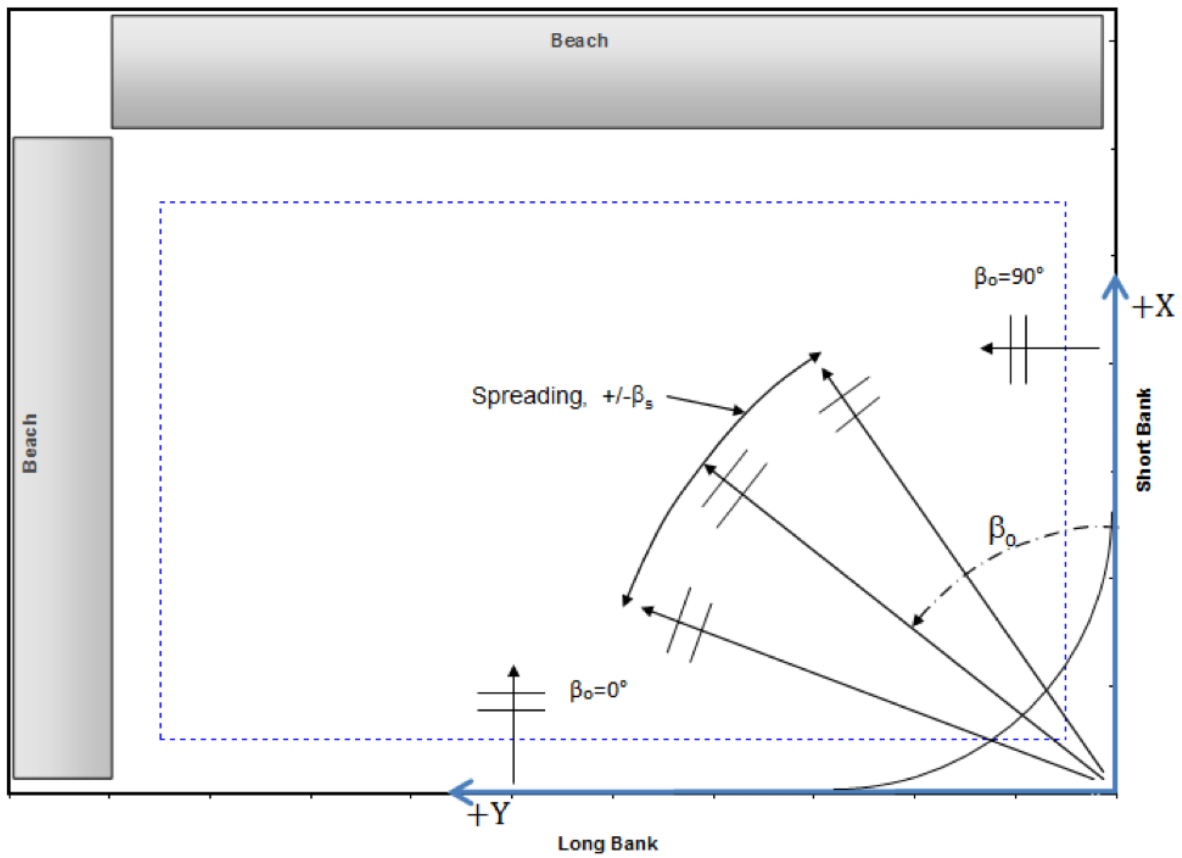


Figure 1.9: MASK reference orientation.

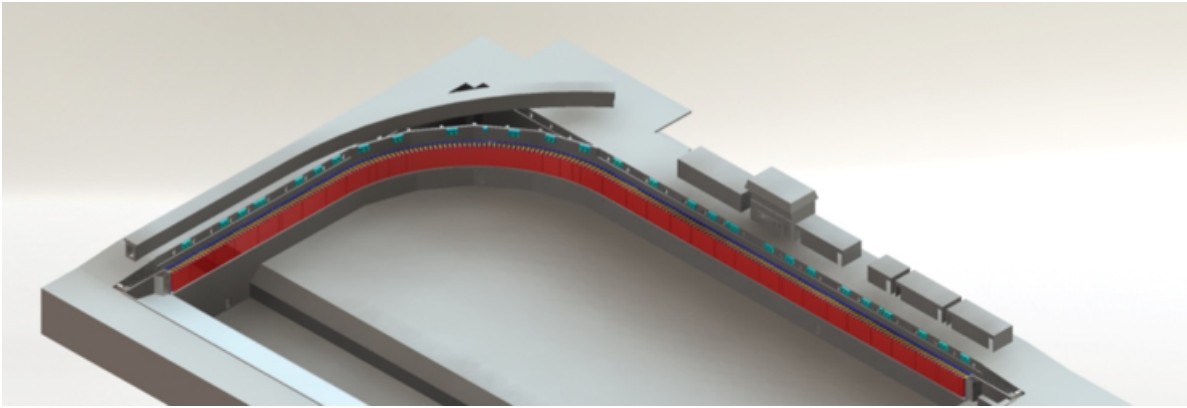


Figure 1.10: General view of new segmented wavemaker in MASK Wavemaking Facility. Paddles are highlighted in red and the control cabinets are highlighted in bright blue.

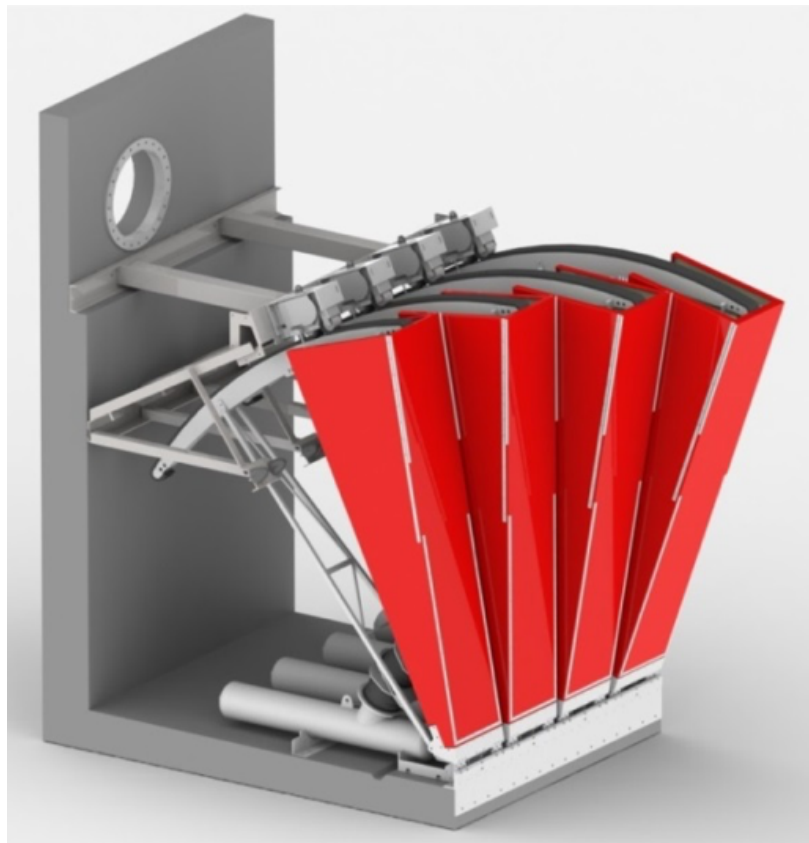


Figure 1.11: Mask wave maker diagram.

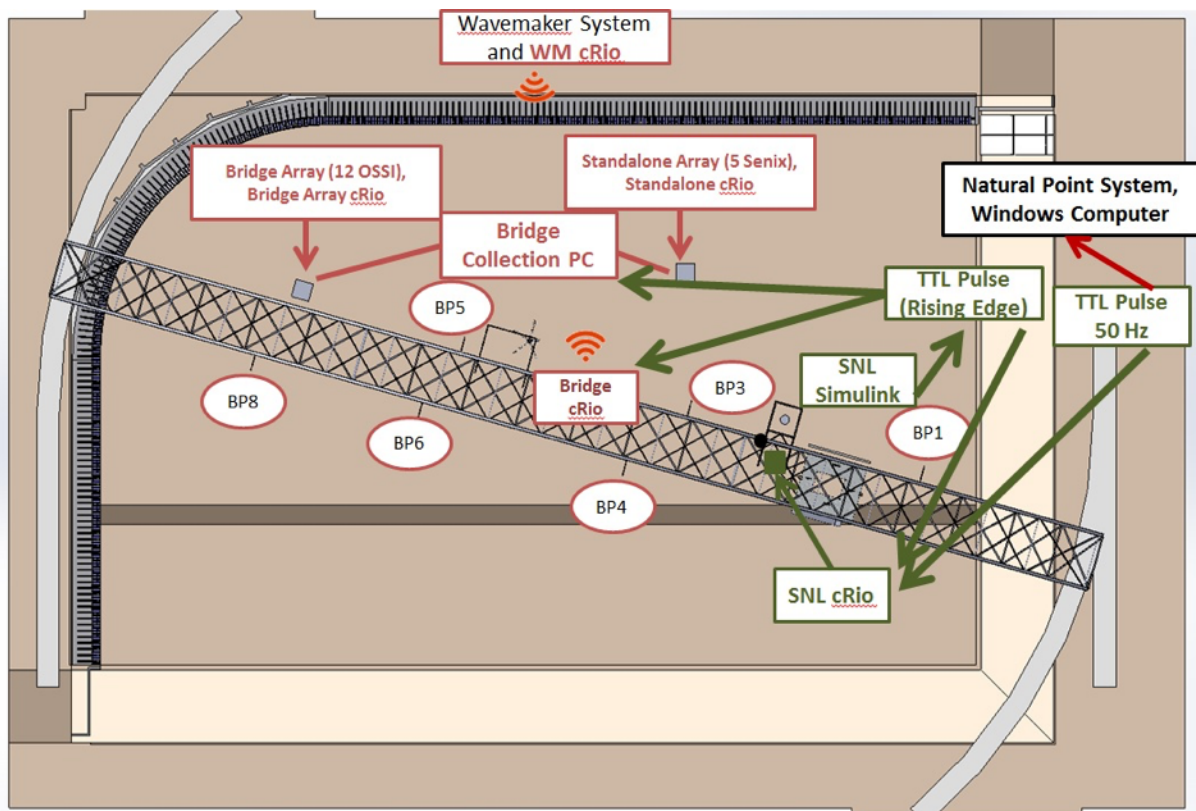


Figure 1.12: Sensor and DAQ layout (sensor and DAQ locations are not to scale). (Markers for “BP#” indicate locations of “bridge-probe” acoustic wave sensors.)

1.2.4 Sensors & data acquisition

1.2.4.1 Data acquisition & Control

To accommodate all necessary data channels, five different collection systems were used; three on the bridge, one on a Standalone Array of wave probes (see Section 1.2.4.8) and one in the wavemaker control room. Figure 1.12 and Figure 1.13 show the data acquisition systems employed. The Bridge DAQ used a National Instruments (NI) cRIO 9076 with a NI 9205 analog card and NI 9467 GPS module. The Bridge Array cRIO 9030 included 12 analog wave measurement signals and the data was time stamped with GPS time with the NI 9467 GPS module. The Standalone Array used a cRIO 9030 with a NI 9205 analog card and NI 9467 GPS module. The wavemaker data collection consisted of the EDL wavemaker system itself that can log the paddle positions at 32 Hz. Along with the paddle data, there was a cRIO 9012 with a 9403 digital card to record the 3 outputs from the wavemaker: status, start, and end. The wavemaker’s cRIO also contained a NI 9467 GPS module to timestamp the data. The SNL Simulink PC used a NI PCIe-6320 DAQ board for real-time control. A cRIO-9082 was used for signal logging of all channels other than those the wavemaker and wave sensors.

A high-level diagram of the SNL data acquisition, hardware and cabling layout along the

MASK Collection System Overview (considering only data streaming to SNL)

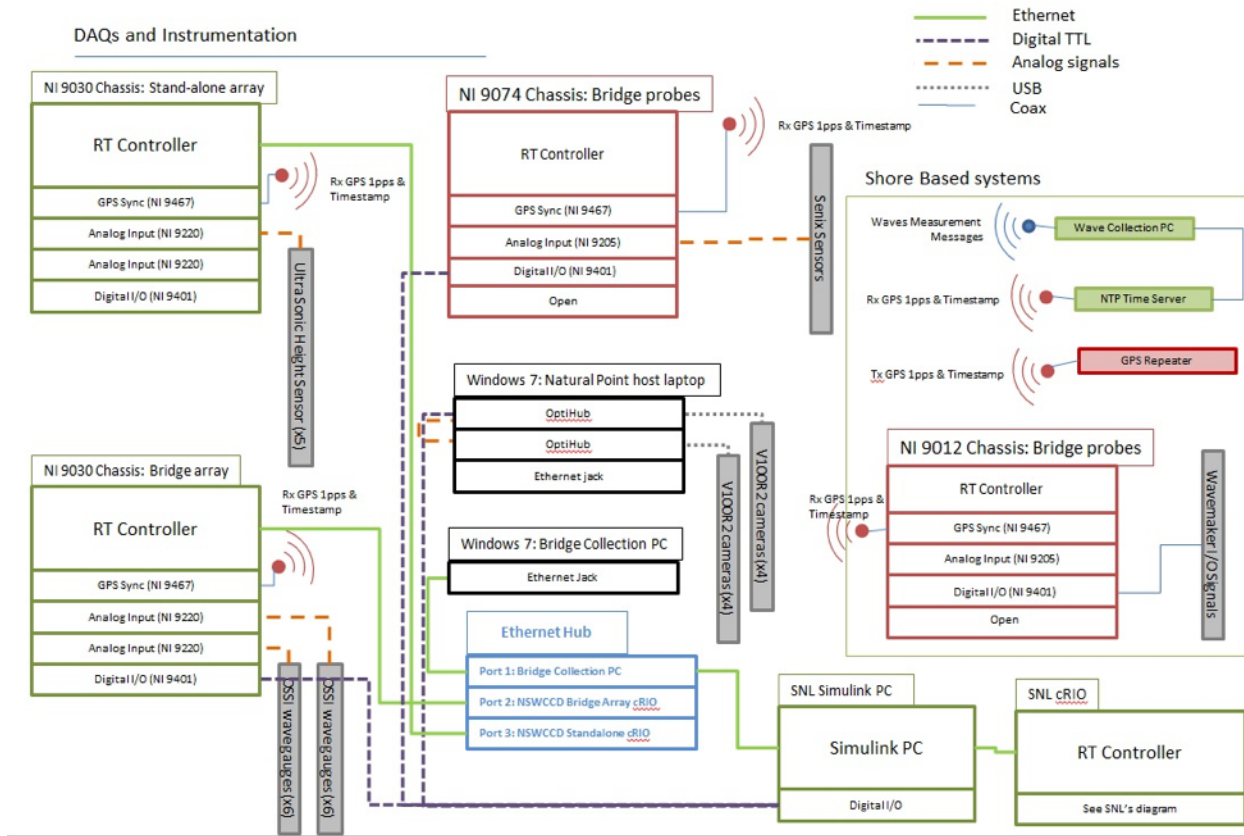


Figure 1.13: Layout of collection systems and triggering mechanisms.

MASK bridge is shown in Figure 1.14. Figure 1.14 is a top-down view of the bridge, with the gray pathway representing the catwalk that runs along the bridge. The weldment is shown by a light blue outline. Figure 1.14 also shows the layout for the actuator power and control system. Emergency stop buttons to cut power from the WEC’s actuator, are shown as red figures with a white “E.”

In order to synchronize test runs and data logging between systems, two approaches were used: TTL triggering and GPS time-stamping. GPS time is broadcast into the MASK facility through the use of a repeater attached to a GPS antenna that sits outside of the building. Figure 1.13 shows the collection systems and their interaction via these mechanisms. GPS time-stamping allows datasets collected by the different DAQs in the test setup to be aligned during post-processing (see Section 1.4).

The data being collected on the Bridge Array and Standalone Array was stored on its own computer. Data from Sandia’s cRio was stored on its own host computer while the bridge Sonics and wavemaker output was collected on a separate Navy machine. The data was backed up after every testing day onto a separate external RAID hard drive. Data sets were combined and synthesized after testing was complete (see Section 1.4 for additional info on data synthesis).

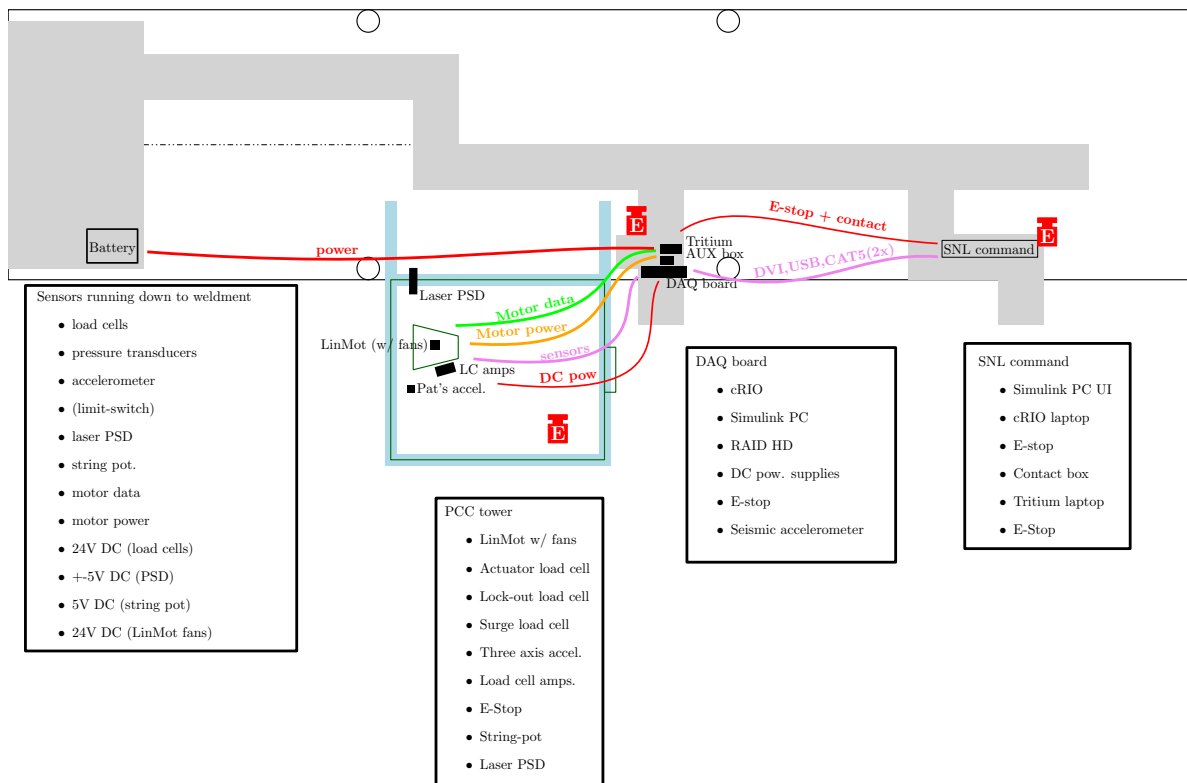


Figure 1.14: Layout of SNL data acquisition, hardware and cabling along MASK bridge.

1.2.4.2 Device actuator

A LinMot P10-70x400U linear actuator driven by Tritium WaveSculptor 200 three-phase controller served as the WEC's PTO. This motor allows for 4-quadrant control. This system was controlled via CAN-bus commands sent from Sandia's "Simulink PC" (see Section 1.2.4.1 for a discussion on data-acquisition and control). Power was supplied by a 96 V battery pack. In addition to software kill-switches, manual kill switches were located at the SNL Command Center, SNL DAQ board and on the weldment (see "E" switches in Figure 1.14). The instantaneous vertical position of the float was monitored using the actuator's sinusoidal encoder.

1.2.4.3 Load cells

A series of load cells were used to measure forces experienced by the WEC device. Three Transducer Techniques MLP-750 load cells, each rated for 750 lbf. (3340 N), were used to measure the force output of the actuator, the force input from the waves in surge, and the pitching moment of the float respectively. The actuator load cell was placed at the bottom of the motor slider (see Figure 1.15). The surge load cell was placed in between the carriage of the PMT and the perimeter of the weldment structure. Figure 1.16 shows how the pitch load cell placed in-line with a single

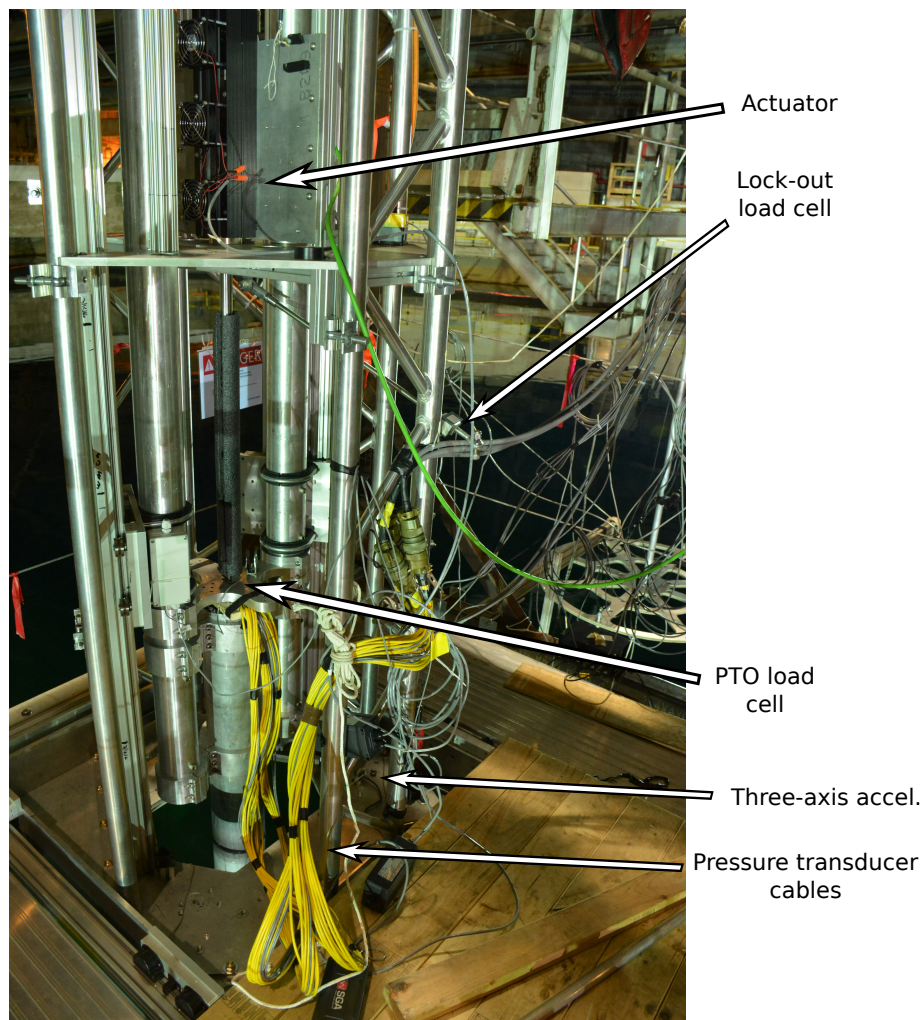


Figure 1.15: Layout of sensors on weldment.

lock-out bar on the float structure. The pitch load cell’s linear force measurement was converted to obtain the pitching moment. The pitch and surge load cells were only used in a small set of tests. One Transducer Techniques LPO-2K load cell, rated for 2000 lbf. (8900 N), was used to measure the force in heave when the vertical motion of the device was restricted (i.e. in diffraction tests; see Section 1.3.1). The lockout load cell can be seen in its storage configuration in Figure 1.15. Extra LPO-2K and MLP-750 load cells were kept on hand for use in the event of a load cell failure.

Calibration Two sets of data were used to produce the calibration parameters for the load cells used in this testing campaign: tests using a universal testing machine were used to obtain the calibration slope while static offset tests were used to obtain the calibration offset. For the slope tests, each load cell was placed in a universal testing machine and loaded with a known tension force. The amplified voltage output of the load cell being tested was measured using a multimeter. For these tests, there was an initial pre-load to make sure the shackles of the machine were secure and did not shift during the calibration test. The pre-load was zeroed out of the system before



Figure 1.16: Pitch lock-out load cell installed on float.

each set of tests. The slope calibration parameters for the load cells are shown in Figure 1.17. The offset components of the calibrations were obtained from the “tare” data at the beginning of a large set of tests. While the basin was calm and no force was being applied by the actuator, the force measurements from the load cells were taken as the offset calibration parameters. The calibration slopes and offsets are presented in Table B.6.

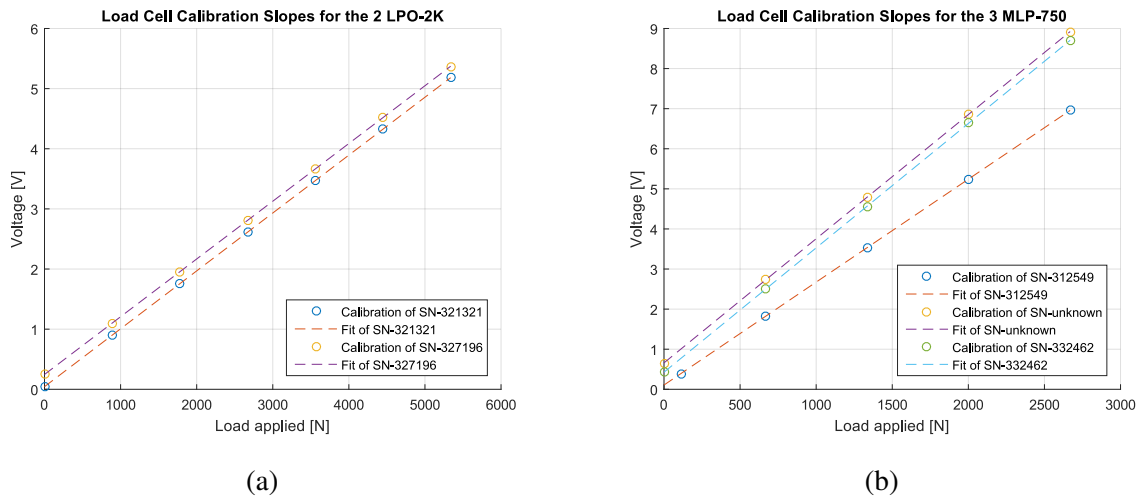


Figure 1.17: The fit for each load cell is shown as the dashed line and the points of calibration are the circular markers. The load applied was measured in newtons and the output of the devices was measured in volts.

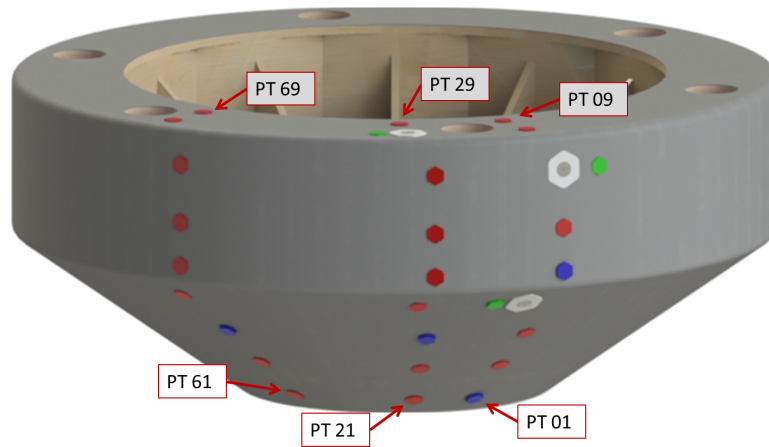


Figure 1.18: Pressure sensor locations and numbering convention. A red sensor denotes a Transducers Direct TDH-40, a blue sensor denotes an Omega PX-459, and a green sensor denotes an Amphenol NPI-19B. The larger grey sensors denote locations of the slam panels, sensors designed to measure slamming impacts on the device.

1.2.4.4 Pressure sensors

Twenty-four hull-mounted pressure sensors were used to measure the dynamic pressure on the device's hull during tests. A diagram of the pressure sensors with their numbering convention is shown in Figure 1.18. Three vertical arrays with eight sensors each were used. The pressure sensor arrays were oriented at 0° , 20° and 60° relative to the incoming wave train (with 0° being directly in line with the incoming wave fronts). A two-digit ID number, with the first digit corresponding to the array (0, 2, 6) and the second digit to the sensor within that array (0, 1, 2, ... 9), was used to distinguish each sensor. Three types of pressure sensors with varying capabilities were utilized: twenty Transducers Direct TDH40 sensors were used as a low-cost option; three Amphenol NPI-19B sensors were installed as a medium-cost option; and four Omega PX-459 sensors were used as a high-cost option. The three Amphenol pressure sensors were damaged during assembly. As these were not considered critical measurements, the slots were covered and left empty for the tests.

Figure 1.19 shows the installed pressure sensor ports on the hull of the device. In this image, the 01–09 array is on the far right, the 21–29 is centered and the 61–69 is to the left. Each pressure transducer was placed inside of a PVC housing and connected to that housing with a PVC cap (see Figure 1.3 for internal PVC piping in float). The pressure transducers were sealed in place with silicon to prevent water damage to the sensors and flooding in the float.

Calibration In order to determine the calibration factors for the pressure transducers, hydrostatic pressure tests were used. In the first test, the float was forced upward or downward in static steps while measuring its position. Using the known position of each pressure transducer on the float, the individual calibration curve for each transducer was determined. The calibration was determined by comparing the measured voltage with the calculated hydrostatic pressure based on the sensors



Figure 1.19: Pressure sensor ports on hull of device.

known position. In Figure 1.20, the actual pressures recorded for each step throughout both tests (using the sensors' factory calibrations) are shown as dots. The hydrostatic pressures, based on the sensor location for the position of the float, are shown as lines.

Some of the sensors have a shift in reading due to an offset in the sensor or a slight misplacement of the sensor on the buoy. Since hydrostatic pressure is a linear phenomena with respect to water depth, the signals can be shifted by a calibration. Table B.5 gives the calibration slopes and offsets for all the pressure transducers to get from voltage to calibrated pressure in kPa.¹

1.2.4.5 Structural vibration sensors

Some additional measurements were taken to monitor vibration of the bridge and weldment structure. These measurements are considered secondary (i.e. not mission critical for this stage of testing) and were therefore not necessarily recorded for every test. Three different measurement devices were used for this purpose:

- **Seismic accelerometer** - Low-frequency bridge oscillations we measured using a Wilcoxon Research Model 731A seismic accelerometer and Wilcoxon Model P31 power unit/amplifier. The seismic accelerometer was located next to the SNL DAQ board (see Figure 1.14). This sensor is capable of accurately capturing low-frequency accelerations down to 0.05 Hz with a sensitivity of 10 V/g.
- **Three axis accelerometer** - A PCB Model 3713B122G triaxial accelerometer and PCB Model 478B05 signal conditioner were used to measure accelerations on the weldment. The

¹The curve for PT02 is excluded from Table B.5 because the pressure sensor was determined to be faulty. The curve for PT04 is excluded because the pressure transducer to be placed here was damaged during assembly and not included.

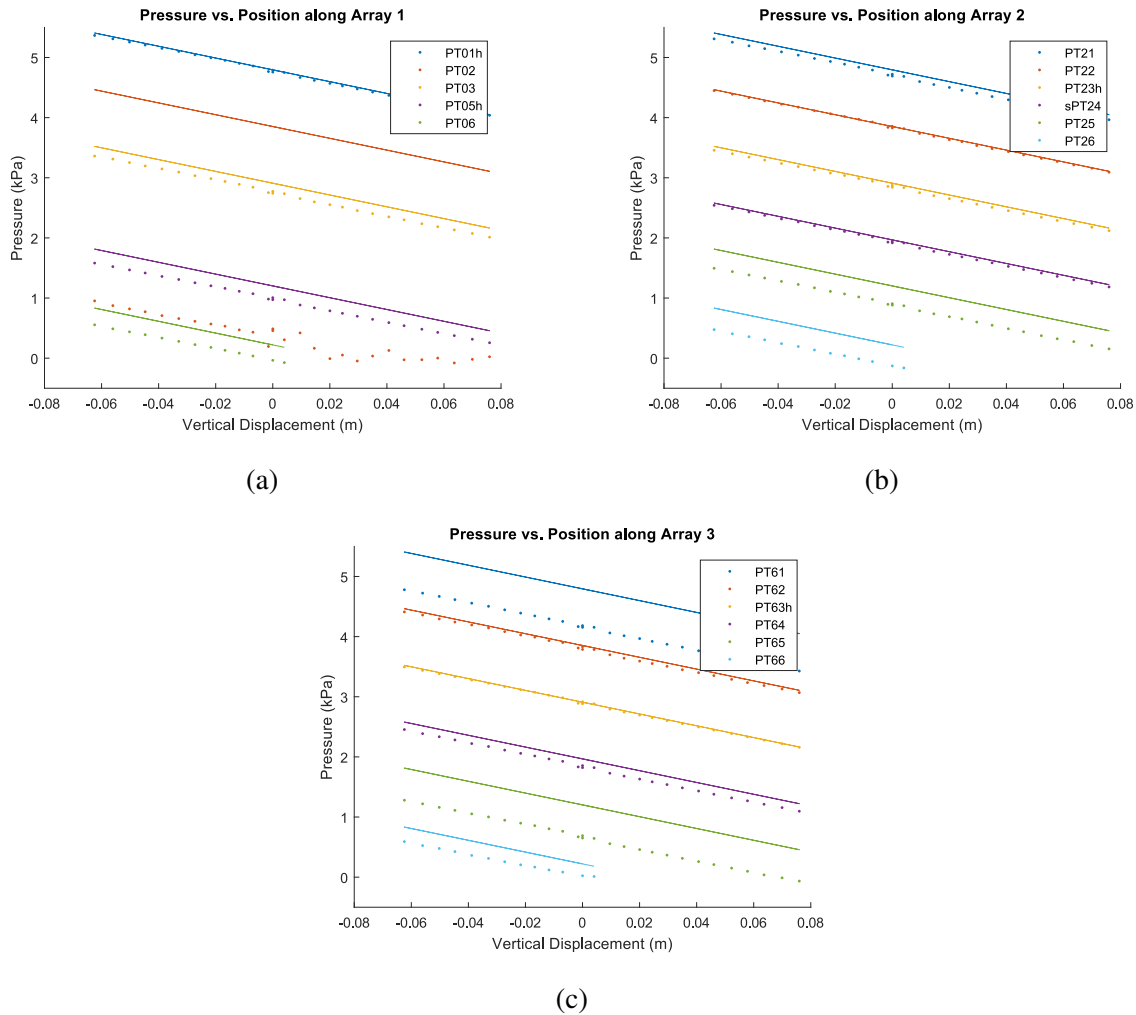


Figure 1.20: Pressure sensor calibrations: factory calibration readings are shown as dots, hydrostatic pressures (calculated) are shown as lines. In (a), PT02 is a faulty sensor which reads close to zero.

x , y and z -axes were aligned with the surge, sway and heave degrees-of-freedom of the buoy respectively. This accelerometer was placed on the bottom plate of PTO tower, as shown in Figures 1.15 and 1.21.

- Laser PSD** - To directly measure instantaneous vertical position of the weldment, a sensor setup composed of a laser and a position-sensing diode (PSD) was used. A tightly collimated class III A laser (Thorlabs Model CPS532) was mounted to a stanchion at the basin shore; a Thorlabs Model PDP90A PSD was mounted on the weldment.² The detector assembly used a forward-mounted converging lens to focus the laser beam near the PSD. As the detector assembly moves relative to the fixed laser beam, the focused laser spot moves on the face of the PSD, and the position of the spot is measured as an analog voltage. To calibrate the

²The mounting location of the laser was confirmed to be sufficiently stationary (i.e. not affected by waves in the basin) using the a number of tests with the seismic accelerometer.

Three-axis accel.



Figure 1.21: Location of triaxial accelerometer at base of PTO tower.

system, the detector assembly was mounted on a micrometer x - y - z motion stage, and the PSD response was determined for a known translation of the detector.

1.2.4.6 NaturalPoint tracking

A NaturalPoint optical tracking system was used to measure the position and orientation of the float. Figure 1.22 shows the four luminescent optical tracking probes which were located on the hull of the float. For most tests considered in this report, the NaturalPoint position/orientation measurement is redundant and the vertical position signal from the linear actuator (see Section 1.2.4.2) is used instead.

1.2.4.7 Video recordings

High-quality video recordings were taken during tests. Figure 1.23 shows a single frame from one such video. Video was recorded at 30 frames per second with a 1920×1080 pixel resolution. A GPS timestamp is placed in upper-right-hand corner of each video frame. These videos have the potential to be used for motion tracking, tracking the local waterline, and observing specific events, such as overtopping or slamming.



Figure 1.22: NaturalPoint optical tracking probes on float.



Figure 1.23: Screen shot for testing video recordings.

1.2.4.8 Wave sensors

A number of wave sensors were installed throughout the basin to measure incident, diffracted and radiated waves during testing. Sonic, capacitive and resistive sensors were used. All wave sensor locations within the basin were recorded using a TotalStation survey tool. Figure 1.24 shows the location of the WEC test device within the basin along with the various wave sensors. The locations in Figure 1.24 are tabulated in Table B.1. Figure 1.25 shows some of the installed wave sensors and wave sensor arrays. Figure 1.25a shows a top view of the “Carriage Array” sensor assembly. The Carriage Array sensors are located at $(20 \leq X \leq 30, 29 \leq y \leq 36)$ in Figure 1.24. Figure 1.25b shows the “Device Array” with the float, weldment and actuator tower in the background. The

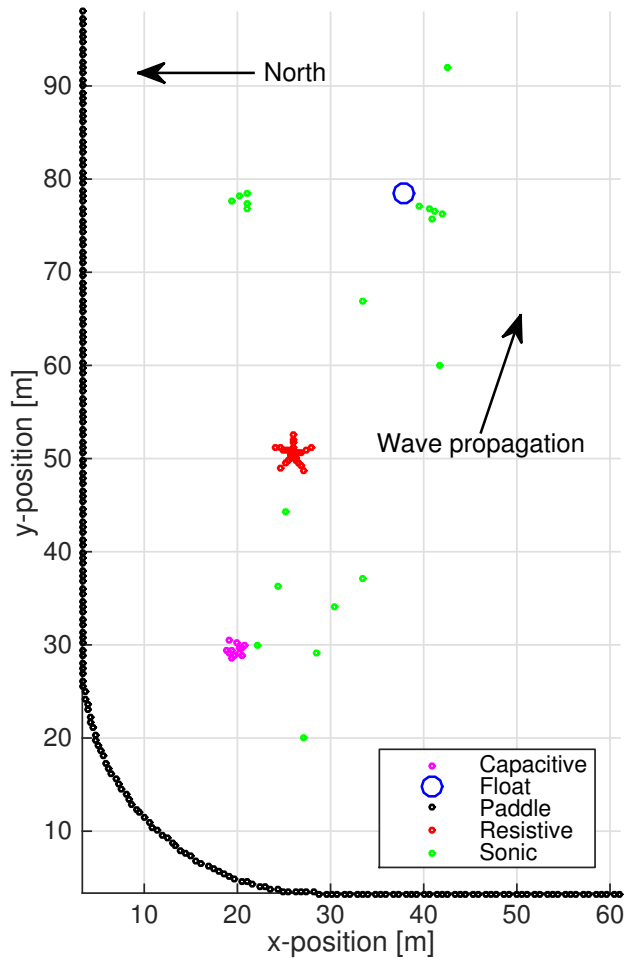


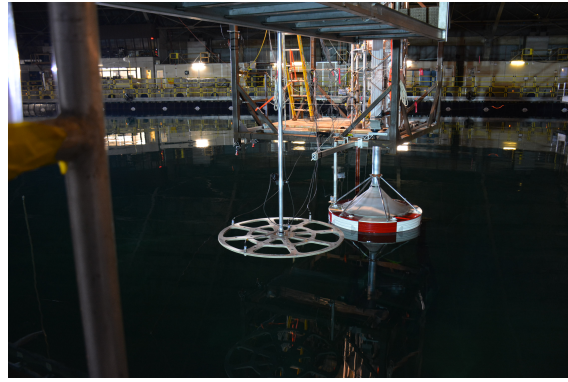
Figure 1.24: Wave sensor and device locations within MASK basin. See Table B.1 for tabulated locations.

Device Array sensors are located South-West of the float at $(x \approx 40, y \approx 75)$ in Figure 1.24. The “Standalone Array” is shown in Figure 1.25c during a radiation test. This cluster of sensors is located at $(x \approx 20, y \approx 78)$ in Figure 1.24.

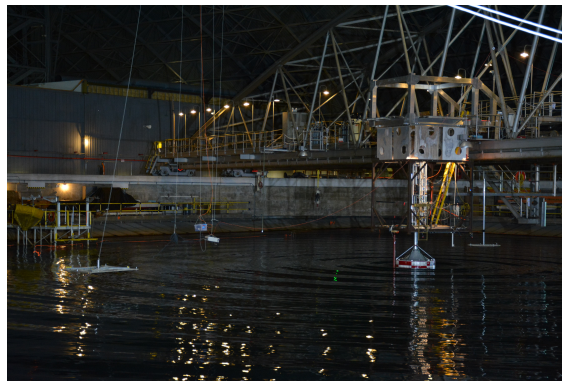
All sonic sensors were configured with sampling and collection frequencies of 20 Hz, a transmit power of 10, no hardware filtering, and set to mark drop outs as a voltage high. To correct dropouts in sonic sensors, the despiking method described by Goring and Nikora [6] was employed. Wave sensor calibration was performed before and after testing. As is standard procedure in the MASK basin, wave sensors were calibrated using a pipe with 11 pre-drilled holes that were precision machined at 4 in (0.1016 m) separation. A complete listing of calibration factors for wave sensors is shown in Tables B.2 and B.3.



(a) Top view of “Carriage Array” wave sensors.



(b) “Device Array” wave sensors shown from side.



(c) “Stand-Alone Array” wave sensors shown during a radiation test.

Figure 1.25: Wave sensor arrays used in testing.

1.3 Experimental Design

Wave energy converters (WECs) have a great deal in common with other ocean-based engineering systems. As such, many of the methodologies used to model and test both ships and offshore structures (e.g., oil and gas platforms) are employed for WECs. However, the design and analysis methods used for WECs must acknowledge and handle the large amplitude motions of these devices. Whereas ship and offshore platform designs are generally targeted to minimize motion in seaways, a WEC must be designed to maximize motion in order to, in turn, maximize energy absorption. This shift towards general operation in a large amplitude motion regime directly violates the main assumption used by many of the potential flow codes and models which form the basis for ship, offshore structure and (to this point) WEC design.

To address this challenge, novel dynamics modeling and system identification (ID) approaches may be necessary. For this study, we have considered the use of the many system ID testing procedures prevalent in a range of engineering fields (aerospace, automotive, electronics). These

practices have been applied recently by Davidson et al. [7] and Giorgi et al. [8] to a WEC using computational fluid dynamics (CFD) in the place of physical wave tank experiments. These approaches have the potential to produce more accurate, richer WEC dynamics models and can do so in a more efficient manner (potentially reducing testing time or allow for more expansive testing).

This section summarizes the types of experimental cases considered in this study. First, in Section 1.3.1, three types of experiments are introduced. These experiment types categorize the ways that the two available inputs (waves in the basin and forcing from the actuator) are used for each test. Next, in Section 1.3.2, types of input signals that can be applied to the actuator and/or waves in each of tests are considered. The definitions given in these sections are used to describe tests in Chapter 2 and in test log supplied in Appendix A.1.

1.3.1 Experiment types

Three basic experiment types can be used to categorize the tests conducted in this study. These categories are effectively divided by the way in which each test type uses the two available excitation inputs of the studied WEC system (basin waves and actuator).

- **Diffraction tests** - In a diffraction test, the device is completely locked and subjected to incoming waves. The force measured on the device can be used to produce an excitation model for the WEC.
- **Forced response tests (forced motion)** - For a forced response test (also known as a radiation test), the device is tested in calm water (no waves), and the motion is forced by means of the actuator. The critical measurements are the vertical position of the buoy and the force applied by the actuator. These tests are generally used to obtain a radiation model for a WEC.
- **Dynamic response** - In a dynamic response test, the device is tested with waves and forcing from the actuator (open loop). These tests are also often called multi-input tests. Typically, for a WEC, the actuator force is chosen to be some control input expected to be used in device operation in power generation. However, the actuator input and waves do not necessarily need to be correlated. In fact, having the two input signals be non-correlated is more advantageous for system ID (see Section 2.7 in Pintelon and Schoukens [9]).

1.3.2 Input signals

The experiment types described in Section 1.3.1 can be applied using any number of input signals for both the actuator and waves. The types of input signals considered during this study are as follows:

- **Monochromatic (regular) waves** - A linear numerical (BEM) analysis of the test device conducted before testing began predicted a resonance of roughly 0.6 Hz. Based on this,

Table 1.2: Idealized ocean spectra (Bretschneider) tested.

Peak period, T_p (s)	Sig. wave height, H_s (m)
1.77	0.138
2.00	0.155
2.39	0.115
3.08	1.21
4.00	0.192

monochromatic wave tests were conducted for $f = [0.25, 0.30, 0.40, 0.50, 0.60, 0.65, 0.70, 0.80, 0.90, 1.00]$ Hz. Wave input amplitudes of 0.025, 0.05, and 0.1 m were considered.

- **Idealized ocean spectra** - Idealized ocean sea states, as represented by Bretschneider spectra, were considered. The waves run during this study are shown in Table 1.2.³
- **Multisine signals** - A number of broad spectra polychromatic signals were also used for system ID.
 - **White (flat) multisine** - White multisine consists of randomly-phased waves which have a constant power spectral density. Note that it is not generally possible to sustain a white noise signal in water waves due to wave breaking.
 - **Pink multisine** - Pink multisine is a randomly-phased signal in which the power spectral density is inversely proportional to frequency. Unlike a white noise signal, a pink multisine can generally be sustained (without breaking) by water waves.
 - **Chirp signal** - A chirp signal is a frequency sweep, which can be defined by some starting and ending frequency as well as a time duration. For a “chirp up,” the input signal starts at the lowest frequency considered and ramps up continuously to the highest frequency considered over the test period. The opposite is done in a “chirp down.”
 - **Stepped-sinusoid** - A stepped-sign is effectively a discretized version of chirp signal, in which the frequency of the sinusoidal signal is changed by some finite amount at predetermined increments.

Traditional tank testing often relies heavily on monochromatic input signals. The multisine input signals used in this study have the potential benefit of exciting the full range of modes in a system with a single test. Even a test program with a large number of monochromatic wave cases will struggle to ever produce the amount of information provided by a single multisine test. In the presence of nonlinearities, the response of a nonlinear systems contains terms due to the interaction between input components at different frequencies. As such, multisine tests are essential in identifying and modeling these nonlinear dynamics.

Another system ID approach not well utilized in wave tank testing is the application of periodic signals. The polychromatic seas used in tank testing are often realized in pseudo-random nature

³These wave correspond with a subset of the waves used for testing in the Wave Energy Prize competition.

in which, for example, the sea state is realized with a 2 hour repeat period⁴ and then run for only 30 minutes. This approach does more closely mimic the real ocean environment. However, the ability to produce periodic multisine signals in the wave tank is a capability that should be taken advantage of, as it provides a number of attractive benefits in system ID (these are well-discussed by Pintelon and Schoukens [9]):

- **Smoother wave spectra** - Figure 1.26 shows a comparison of spectral energy density for two realizations of the same Bretschneider sea state ($H_s = 0.192$ m, $T_p = 4.00$ s). One realization uses a pseudo-random wave component spacing/phasing (2 hour repeating period, 30 minute experiment duration) while the other uses a periodic signal (5 minute repeat period, 15 minute experiment duration). The periodic wave provides a fuller/smoothed spectrum with fewer dips. Note also that this full spectrum is obtained with half the experiment time required by a pseudo-random approach.
- **Reduced spectral leakage** - When taking the discrete Fourier transform (DFT) of a signal with a non-integer number of periods, spectral leakage can occur. By using a periodic multisine input signal in testing, the DFT may be cleanly obtained for both the input (i.e. from wave probes) and for the output (i.e. device response) without the use of windowing.
- **Increased signal-to-noise ratio** - When multiple periods of the same signal are considered, random noise effects in the response can be reduced.
- **Nonlinearity detection** - In a linear time invariant (LTI) system, energy input at a given frequency can only excite a response at that same frequency. Thus, one can identify nonlinear effects in a system response by finding harmonics outside of the frequencies in the excitation signal.

1.4 Data synthesis

As discussed in Section 1.2.4.1, the nature of the experimental setup necessitated the use of multiple DAQ systems. To create a comprehensive dataset from these different sources, the following procedure was used:

1. **Find GPS timestamps from each dataset** - In each dataset, the GPS timestamp vectors were converted to MATLAB `datetime` vectors.
2. **Align files for each test** - Based on the `datetime` vectors from step 1, the full set of data channels contributing to each test were assembled.

⁴For equally-spaced frequency components, the repeat period of a pseudo-random signal is given by $T_r = \frac{1}{\Delta f}$. Alternatively, varying frequency spacing schemes (e.g. equal-energy spacing) can be used to obtain a desired repeat period with an arbitrary number of frequency components.

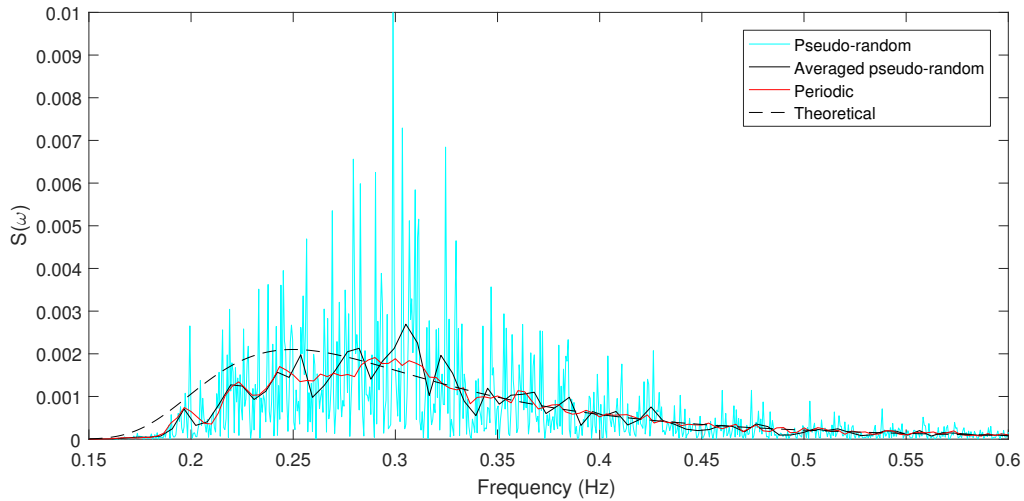


Figure 1.26: Spectral density of pseudo-random (2 hour repeat, 30 minute wave) and periodic (5 minute repeat, 15 minute wave) Bretschneider ($H_s = 0.192$ m, $T_p = 4.00$ s) wave realizations.

3. **Combine files for each test** - The set of datasets for each test (identified in step 2) were combined to form a single structure.
4. **Re-sample data** - To obtain the data points for each channel which correspond to a single universal time series, each data channel was re-sampled at 20 Hz.

For this study, data processing was conducted in MATLAB. All datasets are available for public usage at <https://mhkdr.openei.org/submissions/151> as .mat files, which can be read with MATLAB, GNU Octave and Python.

Chapter 2

System Identification

The system ID practices used widely in other fields of engineering (see, e.g., Pintelon and Schoukens [9]) have, to this point in time, seen relatively little application in wave energy. In this chapter, we use data from a number of experimental cases to construct dynamic models of the hydrodynamic-mechanical system of the model-scale WEC described in Section 1.2.1. The tests and identification processes used for the radiation model are discussed in Section 2.1. The processes and results for the excitation model study are discussed in Section 2.2. The construction of full WEC dynamics models and their resulting validation is discussed in Section 2.3. A discussion of this chapter's findings and conclusions is presented in Section 2.4.

2.1 Radiation model

As discussed in Section 1.3.1, radiation tests were conducted by using the actuator to force the WEC within the calm (no waves produced by wave makers) basin. The actuator was driven with sinusoidal signals as well as periodic broadband signals, in particular white and pink multisine (see Section 1.3.2 for more info). The spectra of the input force for the white and pink noise radiation tests are depicted in Figure 2.1 and 2.2 respectively. The spectra of the resulting velocity responses from those tests are depicted in Figure 2.3 and 2.4 for the white and pink inputs respectively.

These multisine signals have a repeat period of $T_r = 5$ minutes. Tests with a total duration of 15 minutes (including settling/tare time at the beginning/end of the test) were conducted. Thus, two periods of the multisine signals (10 minutes of logged data) were used to obtain the multisine results presented in this section.

2.1.1 Nonparametric models

The complex intrinsic impedance of the WEC Z_i is defined as

$$Z_i(\omega) = B(\omega) + B_f + i(M + A(\omega) - K/\omega), \quad (2.1)$$

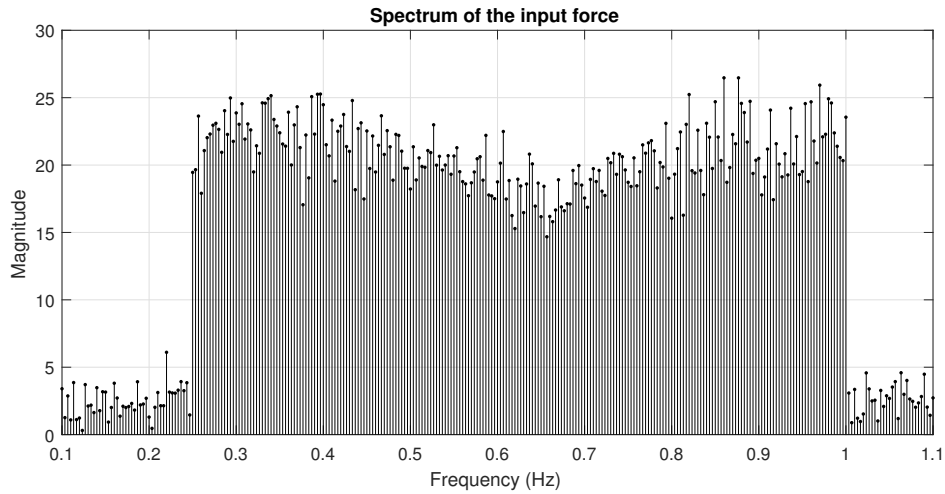


Figure 2.1: Spectra of the input force: white (flat) multisine.

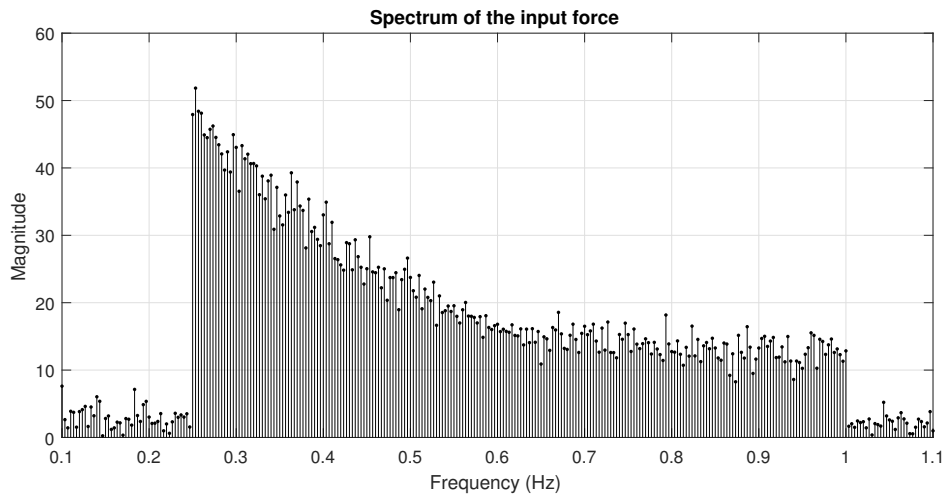


Figure 2.2: Spectra of the input force: “pink” multisine.

where $B(\omega)$ is the frequency-dependent radiation damping, B_f is viscous friction/damping, M is the rigid-body mass, $A(\omega)$ is the frequency-dependent added mass and K is the hydrostatic stiffness.

In this study, the radiation damping, $B(\omega)$, and friction, B_f , terms were distinguished by referencing the radiation damping predicted by WAMIT [10] (see, e.g., Figure 2.10). The friction term, B_f , was then scaled to provide a match with the overall intrinsic impedance. For practical purposes of control design and analysis, this is not an issue, as the quantity of interest when tuning/designing a controller is the intrinsic impedance, not the radiation impedance. For example, in the case of complex conjugate control (see, e.g., Wilson et al. [3]) the optimal PTO impedance is equal to the complex conjugate of the intrinsic impedance.

The following three sections present the resulting radiation models from three types of actuator input signals: pink multisine (Section 2.1.1.2), white multisine (Section 2.1.1.1) and sinusoidal

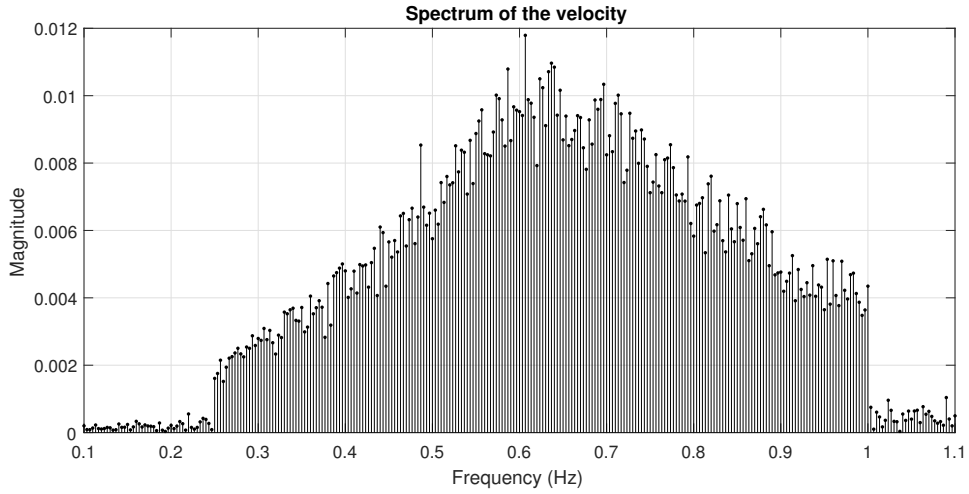


Figure 2.3: Spectra of the buoy velocity for “white” multisine input force.

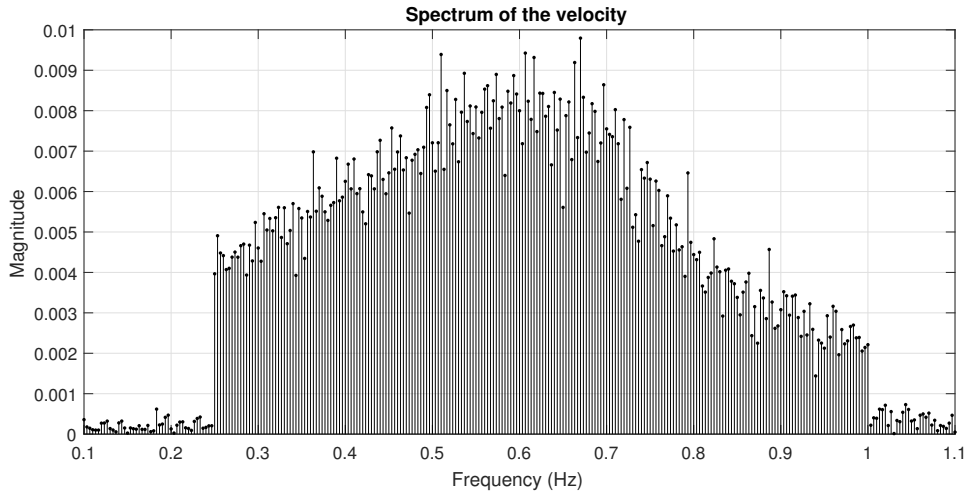


Figure 2.4: Spectra of the buoy velocity for “pink” multisine input force.

(i.e. monochromatic) waveforms (Section 2.1.1.3). In each of these sections, the models are compared using a standard set of plots. Each plot shows three curves: numerical data (where the hydrodynamic coefficients have been calculated using WAMIT), unfiltered experimental data, and averaged experimental data (where the data was averaged over 20 samples, with 10 samples of overlap for smoothing). In each of the experimental cases, the intrinsic impedance is calculated via

$$\hat{Z}_i^{\text{exp}} = \frac{\hat{F}^{\text{exp}}}{\hat{V}^{\text{exp}}}. \quad (2.2)$$

Here, \hat{F}^{exp} and \hat{V}^{exp} are the complex measured force and velocity respectively. The numerical, experimental and smoothed experimental frequency-response-functions (FRFs) are plotted for comparison in a number of ways:

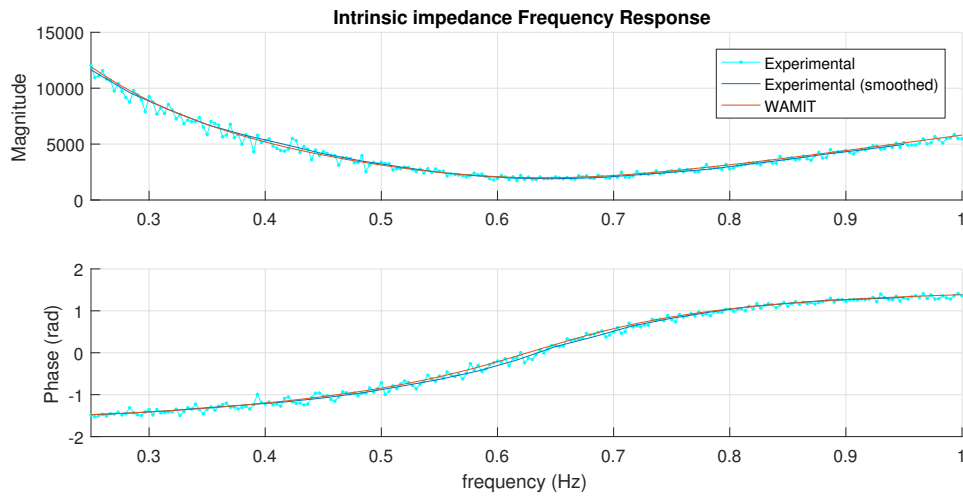


Figure 2.5: Magnitude and phase of intrinsic impedance for a white multisine input force. The estimated linear friction is $B_f = 460$ Ns/m.

1. With the intrinsic impedance broken into magnitude and phase; these plots have the useful capability to identify the resonant frequency (where the phase of the intrinsic impedance crosses the x -axis)
2. With the intrinsic impedance broken into real and imaginary parts; in these plots the resonant frequency occurs where the imaginary part of the intrinsic impedance crosses the x -axis
3. The added mass, $A(f)$, and radiation damping, $B(f)$, are broken out and shown separately

2.1.1.1 Input force: White multisine

Figures 2.5 through Figure 2.10 show the FRFs produced from experiments in which a white multisine signal was used to force the WEC through its actuator. As discussed in Section 2.1.1, three plot types are used to compare the three FRFs (WAMIT, experimental, and smoothed experimental). Two different experimental tests are considered. Figures 2.5, 2.6, and 2.7 show the results from a experiment with an actuator gain of 1. Figures 2.8, 2.9, and 2.10 show the results from a experiment with an actuator gain of 1.5.

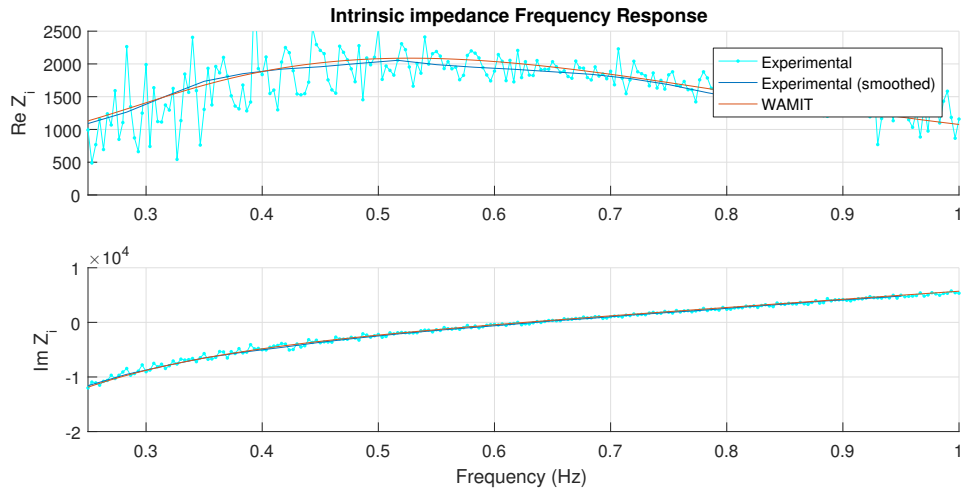


Figure 2.6: Real and Imaginary part of intrinsic impedance for a white multisine input force. The estimated linear friction is $B_f = 460$ Ns/m. It is interesting to verify from the plot of the imaginary part that the resonance frequency is approximately 0.63 Hz ($\text{Im}[Z_i(\omega)]_{\omega=\omega_{res}} = 0$).

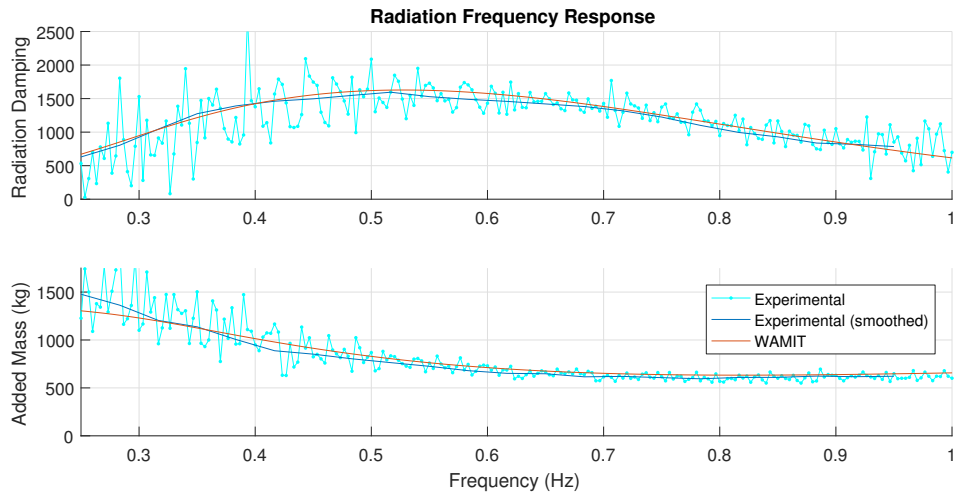


Figure 2.7: Estimated radiation damping and added mass. The input force is a white multisine (Figure 2.1) and the estimated linear friction is $B_f = 460$ Ns/m

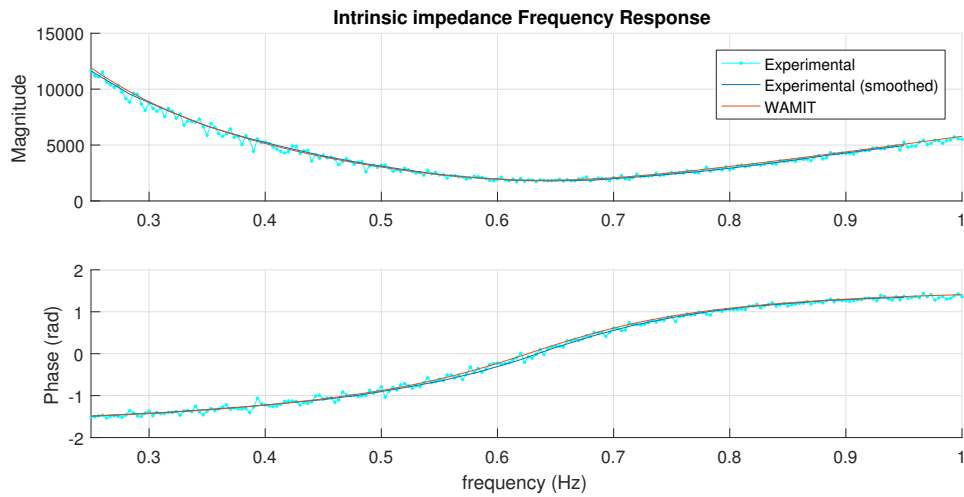


Figure 2.8: Phase and magnitude, input signal is white multisine, actuator gain 1.5 (50% greater than in Figure 2.8). Estimated linear damping is $B_f = 320$ Ns/m.

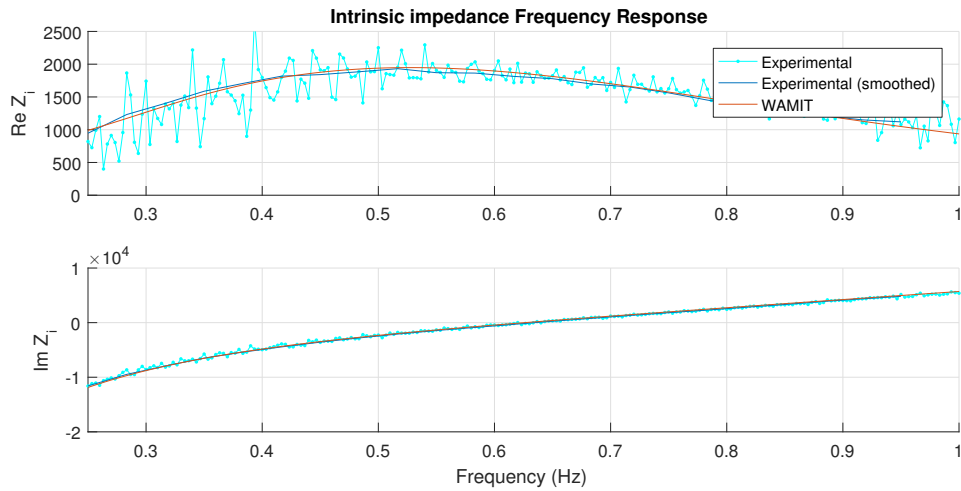


Figure 2.9: Phase and magnitude, input signal is white multisine, actuator gain 1.5 (50% greater than in Figure 2.9). Estimated linear damping is $B_f = 320$ Ns/m.

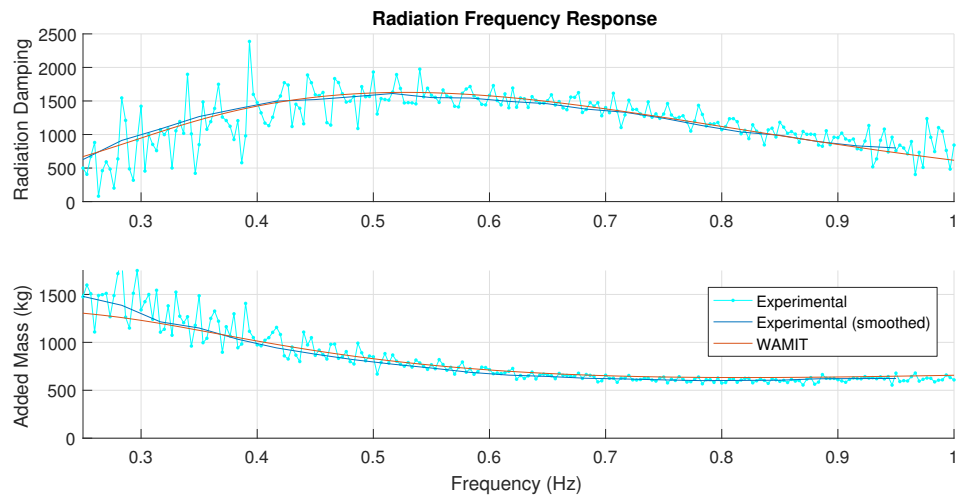


Figure 2.10: Radiation damping and added mass, input signal is white multisine, actuator gain 1.5 (50% greater than in Figure 2.10). Estimated linear friction is $B_f = 320 \text{ Ns/m}$.

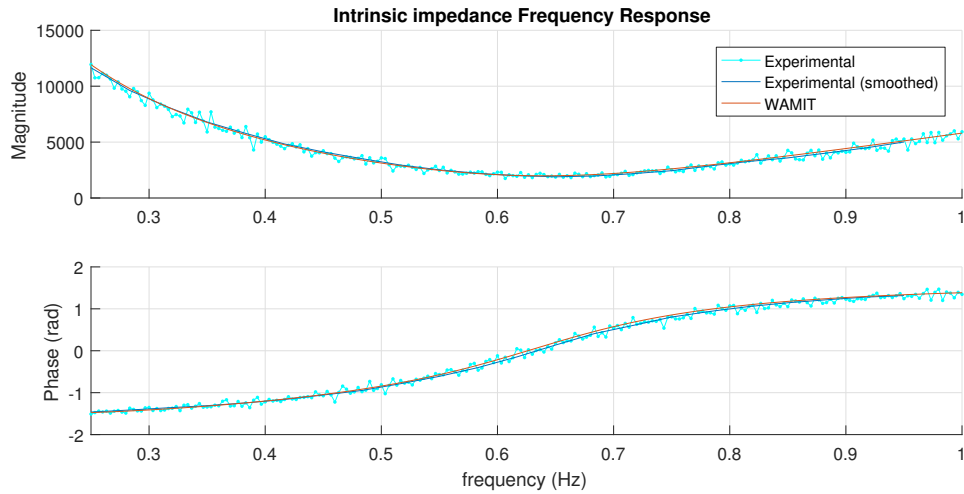


Figure 2.11: Magnitude and phase of intrinsic impedance for a pink multisine input force. The estimated linear friction is $B_f = 460$ Ns/m.

2.1.1.2 Input force: Pink multisine

As with Section 2.1.1.1, this section presents intrinsic impedance predictions from experimental radiation tests. In these tests, the input signals used to drive the actuator were of a pink multisine type. Figures 2.11, 2.12 and 2.13 show the results for an actuator gain of 1.0. Figures 2.14, 2.15 and 2.16 show the results for an actuator gain of 1.5. (The different types of plots employed here are described in Section 2.1.1.)

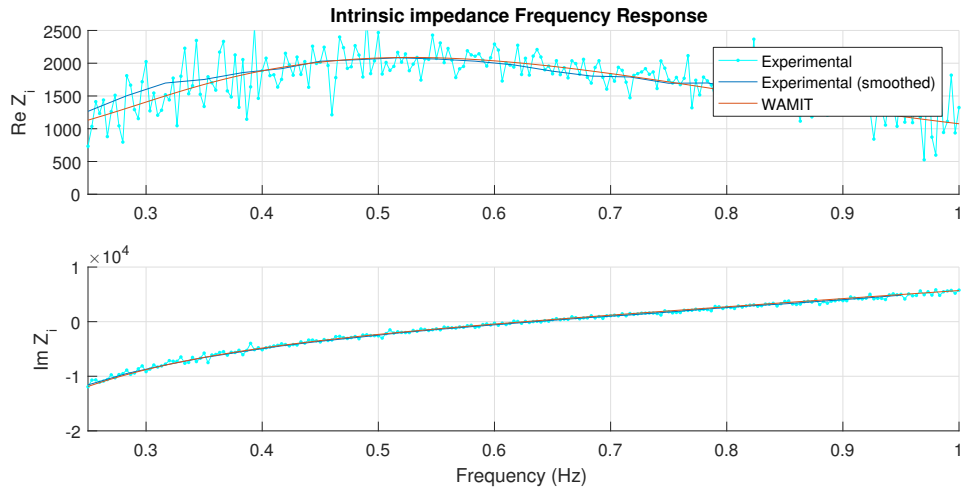


Figure 2.12: Real and Imaginary part of intrinsic impedance for a pink multisine input force. The estimated linear friction is $B_f = 460$ Ns/m. It is interesting to verify from the plot of the imaginary part that the resonance frequency is approximately 0.63 Hz ($\text{Im}[Z_i(\omega)]_{\omega=\omega_{res}} = 0$).

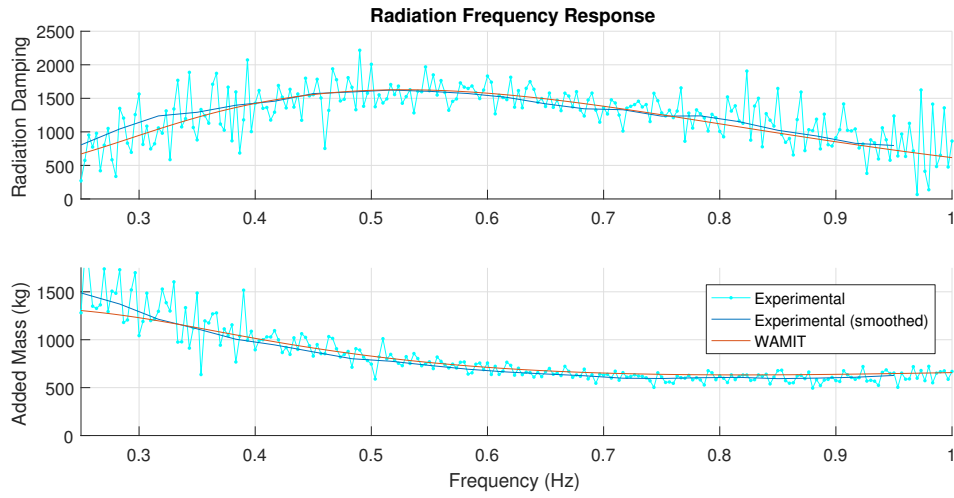


Figure 2.13: Estimated radiation damping and added mass. The input force is a pink multisine (Figure 2.1) and the estimated linear friction is $B_f = 460$ Ns/m

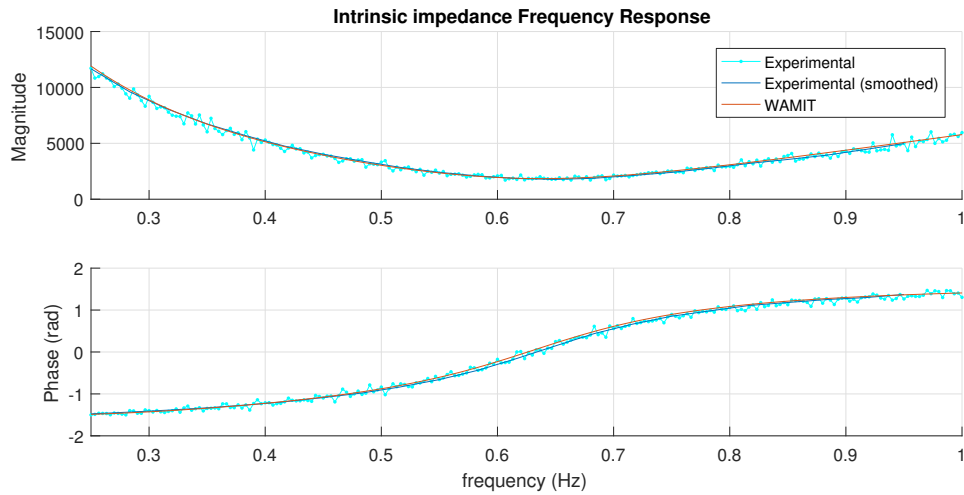


Figure 2.14: Phase and magnitude, input signal is pink multisine, actuator gain 1.5 (50% greater than in Figure 2.11). Estimated linear damping is $B_f = 320$ Ns/m.

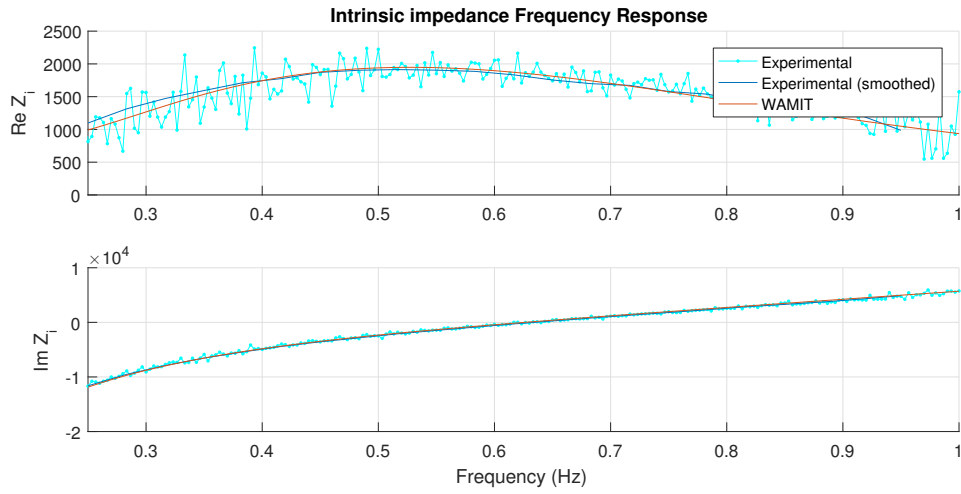


Figure 2.15: Phase and magnitude, input signal is pink multisine, actuator gain 1.5 (50% greater than in Figure 2.12). Estimated linear damping is $B_f = 320$ Ns/m.

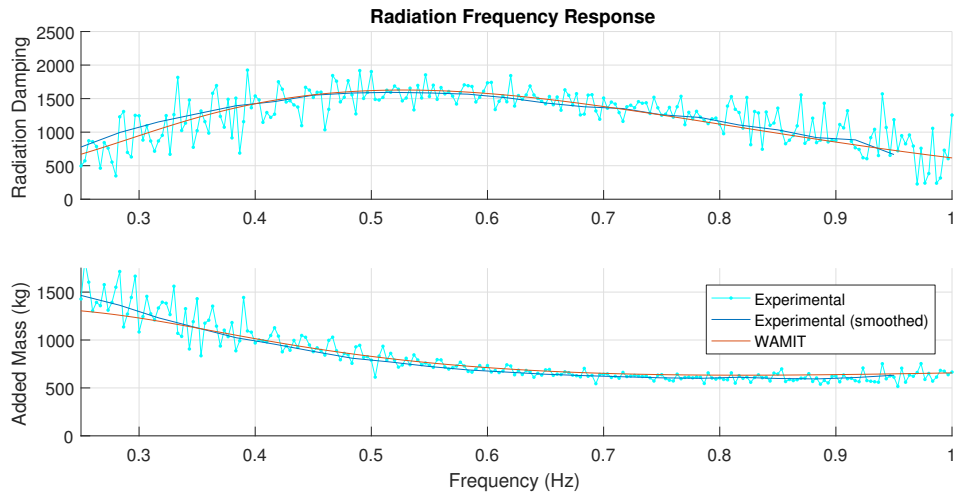


Figure 2.16: Radiation damping and added mass, input signal is pink multisine, actuator gain 1.5 (50% greater than in Figure 2.13). Estimated linear friction is $B_f = 320$ Ns/m.

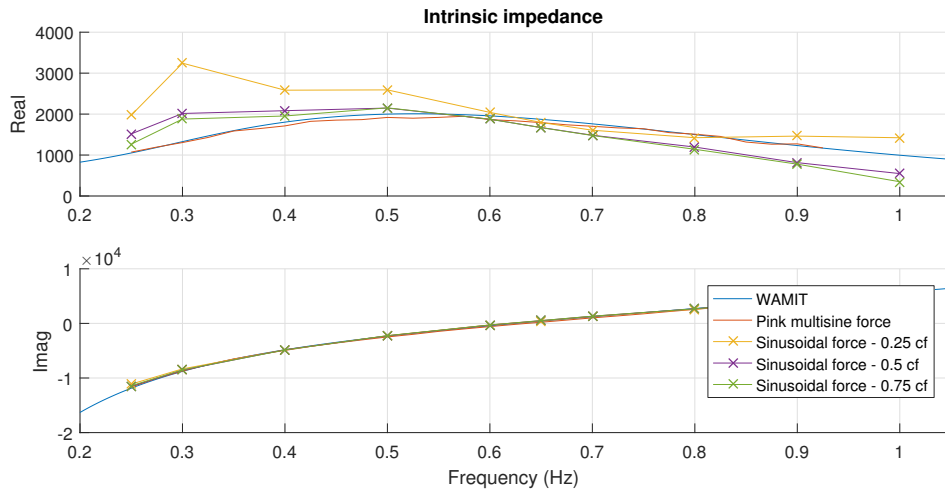


Figure 2.17: Intrinsic impedance calculated using sinusoidal input signals.

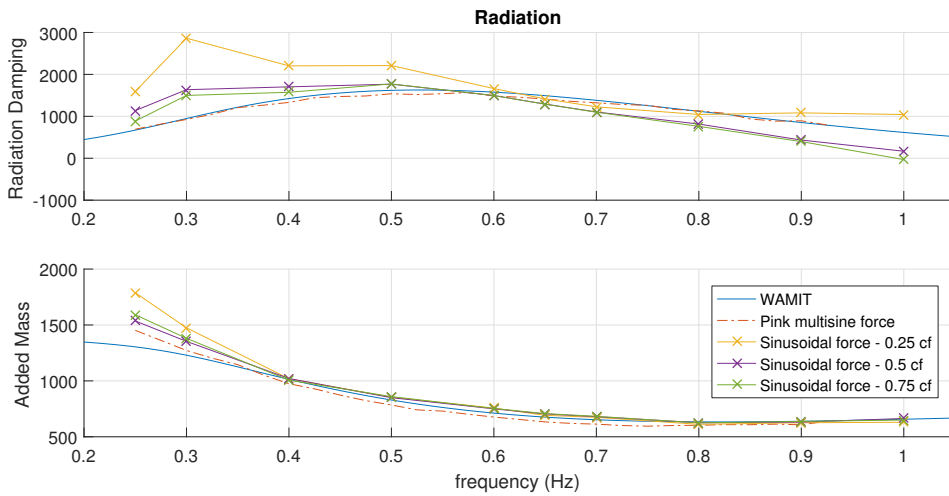


Figure 2.18: Added mass and damping calculated using sinusoidal signal of different amplitudes.

2.1.1.3 Input force: sinusoidal

Figures 2.17 and 2.18 show the radiation models produced from tests where monochromatic input signals were applied on the WEC actuator. These are plotted against the prediction from WAMIT and the results of a pink multisine radiation tests (with smoothing) for comparison. Figure 2.17 shows the real and imaginary parts of the intrinsic impedance. Figure 2.18 shows the added mass and radiation damping components separately. Monochromatic radiation tests conducted at different amplitudes (with the current fraction, “cf,” of the actuator set to 0.25, 0.5, and 0.75) are shown in each plot.

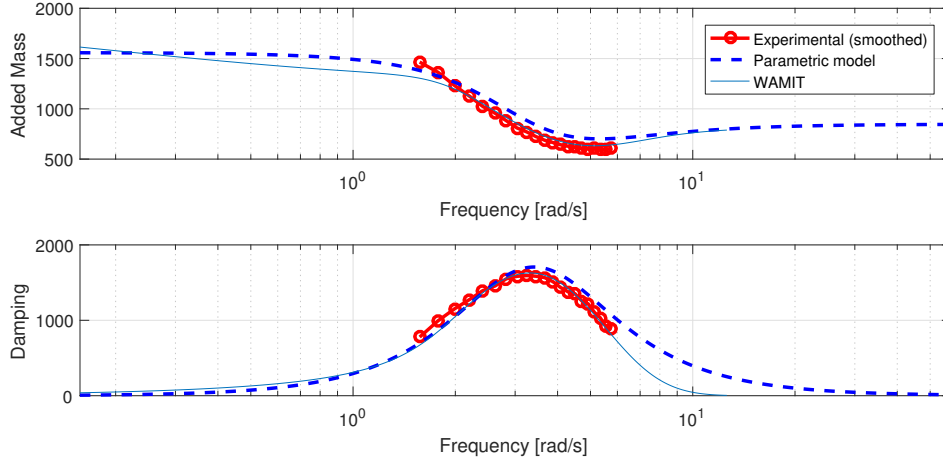


Figure 2.19: Added mass and damping. The plot shows the smoothed experimental data, the parametric model and the data obtained from WAMIT.

2.1.2 Parametric models

2.1.2.1 Identification using periodic signals

Identification Parametric models for the radiation component of a dynamic model for the studied WEC have been obtained using the FDI toolbox [11]. These models were created using data from a test where the actuator used a pink multisine force signal containing frequencies in the range $0.25 \leq f \leq 1.0$ Hz. and a control gain of 1.5. Added mass and damping are plotted in Figure 2.19. This parametric model for the radiation is a second order linear model described by the transfer function:

$$Z_r(s) - i\omega A_{inf} = \frac{8279s}{s^2 + 4.862s + 11.65}, \quad (2.3)$$

where the estimated asymptotic value of the added mass is $A_{inf} = 847.32$ kg, and the estimated linear friction $B_f = 320$ Ns/m. Using the parametric model defined by (2.3) and the definition of the intrinsic impedance in (2.1), the frequency response of the intrinsic impedance for the parametric model is depicted in Figure 2.20.

Validation Validation of this parametric radiation model has been carried out by simulating the response of the buoy when subject to an actuator force that has been applied in a different experiment. The simulated response of the buoy is then compared to the actual response measured during the experiment. Figure 2.21 shows the comparison of the simulated heave velocity with the measured velocity when the spectrum of the actuator force is a pink multisine (gain factor = 1.5). The fit of the model, measured with the normalized root mean square error (NRMSE) of the velocity time series, in this case is: $1 - \text{NRMSE} = 89.3\%$.

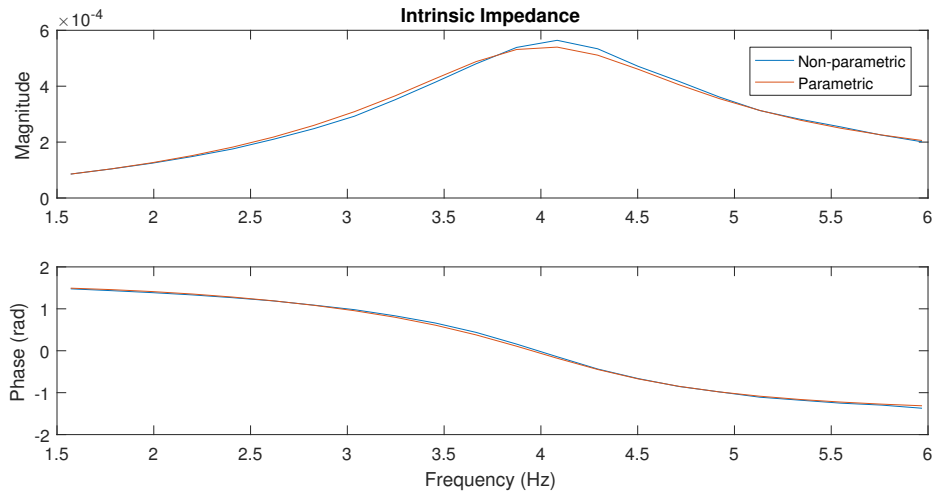


Figure 2.20: Frequency response of the intrinsic impedance, for both the parametric and non-parametric models. Both curves have been obtained from experimental data.

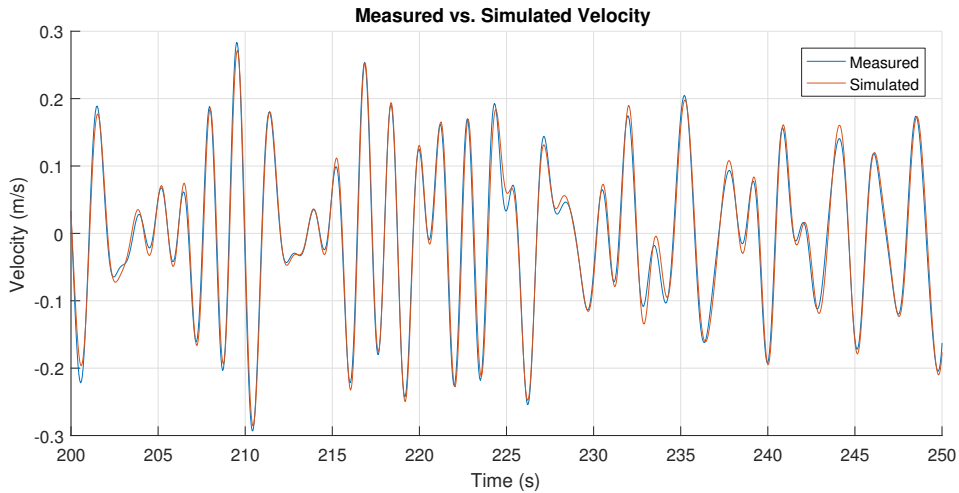


Figure 2.21: Periodic radiation model validation comparison: measured and simulated time series of the heave velocity ($1 - \text{NRMSE} = 89.3\%$).

2.1.2.2 Identification using non-periodic signals

Identification In this section, we consider the procedure to identify a parametric model for the intrinsic impedance using a random signal as the input to the actuator. In particular, the input signal used to force the system is a band-limited white noise, the spectrum of which is plotted in Figure 2.22. Figure 2.23 shows the spectrum of the resulting velocity.

The identification of the intrinsic impedance has been carried out by means of a “black box” approach, using MATLAB’s System Identification Toolbox. The approach is summarized by the block diagram in Figure 2.24. Figure 2.24 shows that, for this model, the actuator force is considered to be the input to the system, and the velocity is the output: in practice, the parametric

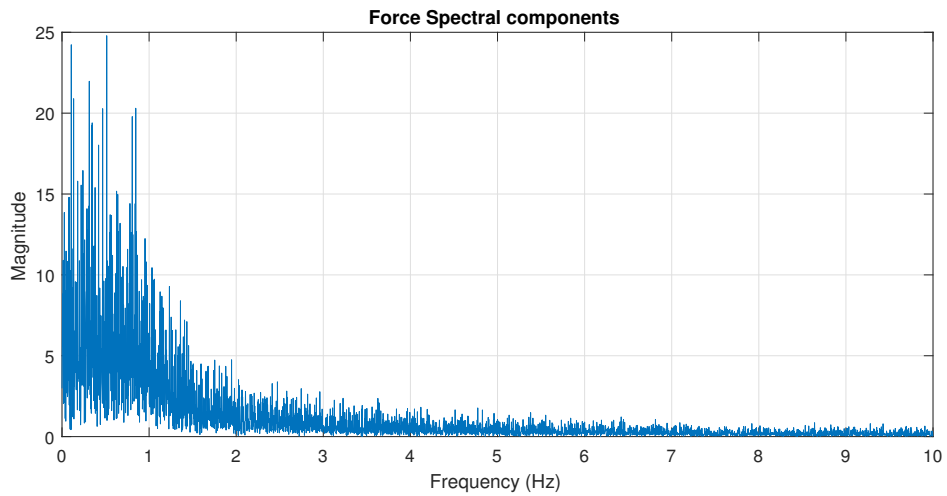


Figure 2.22: Spectral components of the actuator force.

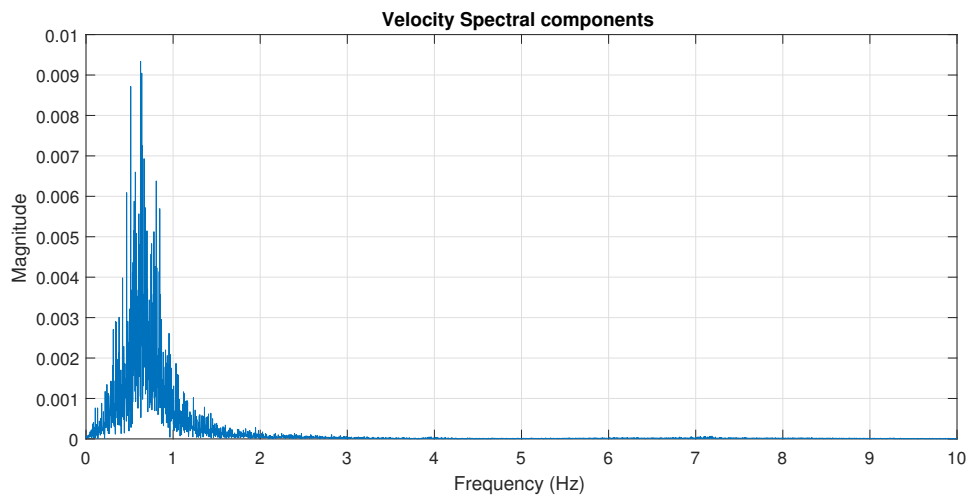


Figure 2.23: Spectral components of the heave velocity.

model describes the inverse of the intrinsic impedance. The identification was carried out using the subspace method, implemented in the function `n4sid`. The subspace method provides a parametric model in the state space form; in this case the model is of order 7. The pole-zero plot of the model is depicted in Figure 2.25. Figures 2.26 and 2.27 show the FRF of the inverse of the intrinsic impedance model. Figure 2.26 shows the real and imaginary parts of the FRF while Figure 2.27 shows the phase and magnitude of the FRF.

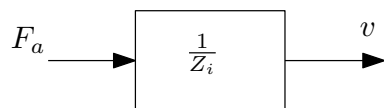


Figure 2.24: Block diagram describing “black box” approach for identification of the inverse intrinsic impedance.

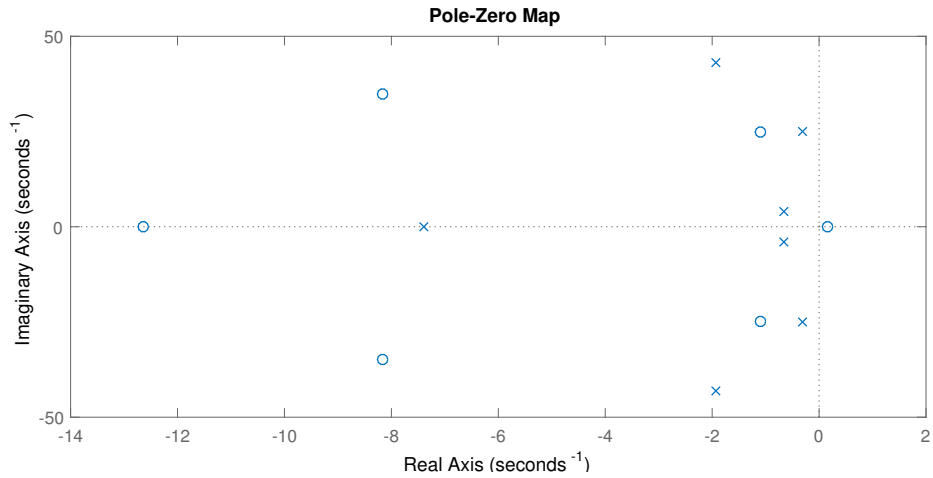


Figure 2.25: Pole-zero map of the parametric model for the inverse intrinsic impedance.

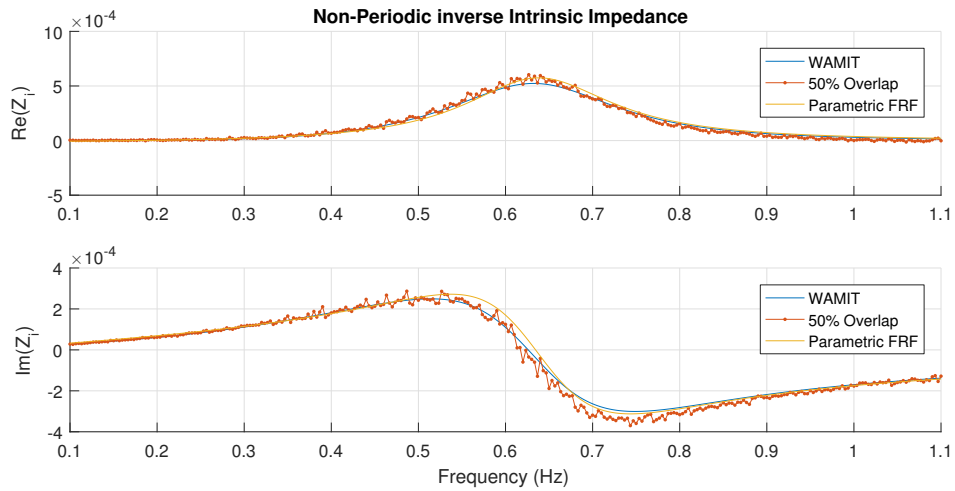


Figure 2.26: Real and imaginary part of the inverse intrinsic impedance.

Validation To perform a validation of the model, identification of the model was carried out using the first 70% of the data points in the time series, thus leaving the last 30% of the data points in the time series for independent validation. Figure 2.28 shows the comparison between measured and simulated velocities; in this case $1 - \text{NRMSE} = 91.2\%$.

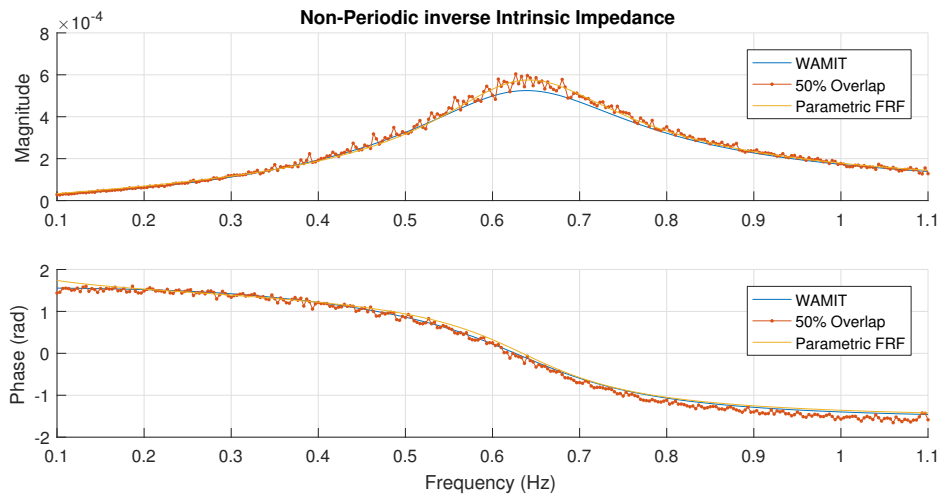


Figure 2.27: Magnitude and phase of the inverse intrinsic impedance.

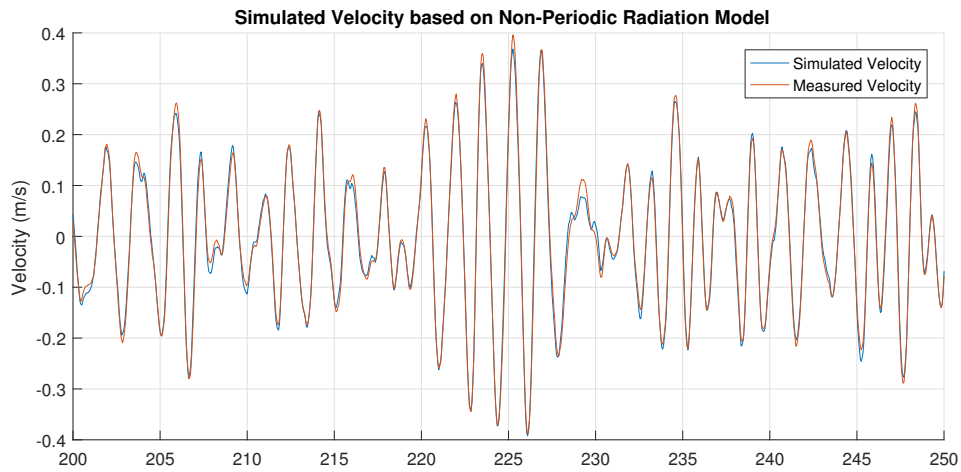


Figure 2.28: Non-periodic radiation model validation comparison: Comparison of simulated and measured velocities ($1 - \text{NRMSE} = 91.2\%$).

2.2 Excitation model

The following sections discuss the identification of excitation models from a number of experimental tests. Sections 2.2.1 and 2.2.2 consider diffraction tests, in which the device is locked and subjected to waves (see further discussion in Section 1.3.1). These two sections use multi-sine (polychromatic) and monochromatic wave signals for their diffraction tests respectively. Section 2.2.3 considers a methodology in which an excitation model can be extracted from a dynamic response test.

2.2.1 Diffraction tests with multisines

Diffraction tests were carried out by locking the heave motion of the device and by generating waves with a pink type periodic spectrum (pink multisine) in Figure 2.29; the duration of each experiment was 10 minutes. (As discussed in Section 1.3.2, white multisine input signals generally produce a large proportion of breaking waves and were therefore not considered for diffraction tests.) The FRF of the excitation is calculated as

$$H(\omega) = \frac{F_{lock}(\omega)}{\eta(\omega)}, \quad (2.4)$$

where $F_{lock}(\omega)$ is the force measured on the lockout load cell (i.e. the force required to prevent the buoy from moving) and $\eta(\omega)$ is the wave elevation measured with a wave probe. Figure 2.30 shows the magnitude and phase of FRFs for multiple wave probes (“Staff #1,” “Staff #2,” ...), overlapped to the FRF calculated with WAMIT.¹

2.2.2 Diffraction tests with monochromatic sinusoids

Diffraction tests were also conducted using monochromatic waves. Figure 2.31 shows the comparison between WAMIT, diffraction tests using sinusoidal waves and diffraction tests using pink multisine. Both the monochromatic and multisine tests show good agreement with the prediction from WAMIT. Note that the low-frequency trends seen in the multisine FRF also appear in the monochromatic results. These may be due to some low-frequency resonance in the test setup (e.g., some seiche modes in the wave basin or resonances in the structure and bridge supporting the device).

¹Note that here the phases of the excitation FRFs have been shifted to overlap.

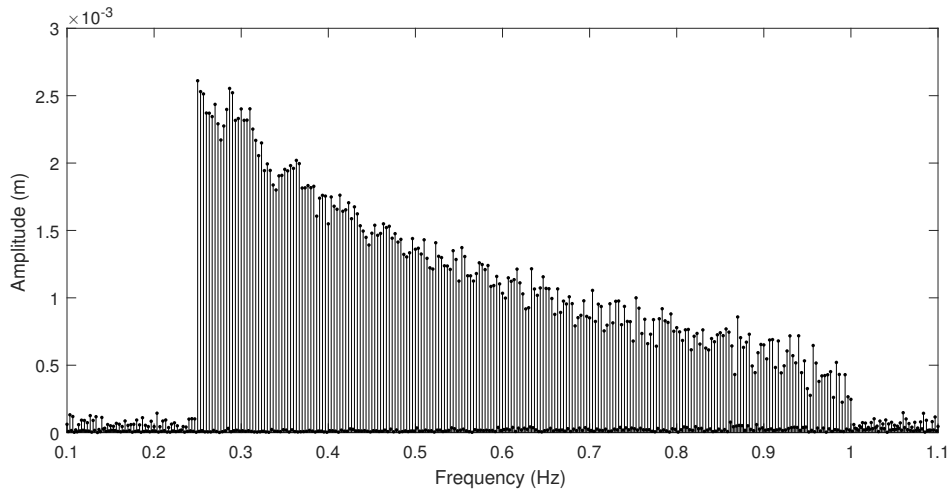


Figure 2.29: Pink spectra of wave elevation. Note: very good repeatability and no spectrum leakage.

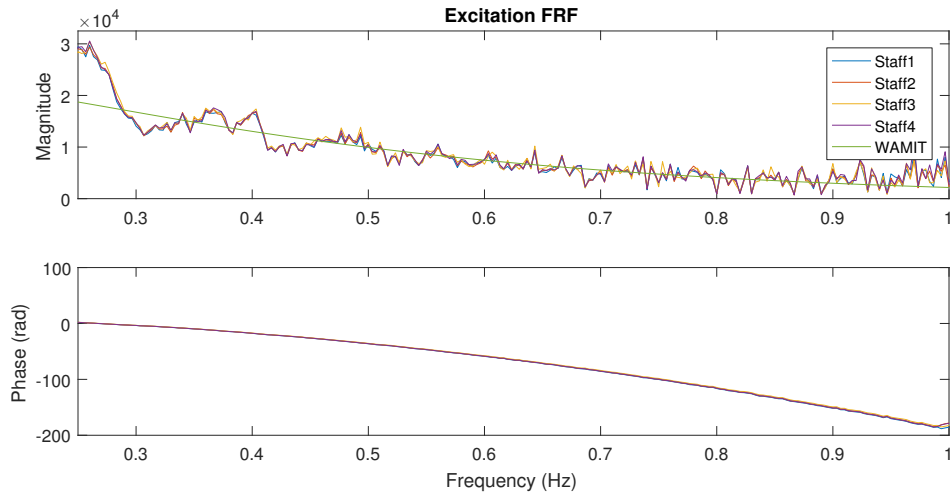


Figure 2.30: Excitation force FRFs calculated using signals from multiple waveprobes (“Staff1,” “Staff2,” ...).

2.2.3 Model separation from forced response tests

This section considers how an excitation FRF can be obtained without locking the device. For this procedure, data from two experiments has been used. The first step is to calculate the radiation FRF using forced oscillation tests (see Section 2.1). In the second experiment, the device is subject to both waves and force from the actuator (i.e. a dynamic response test as defined in Section 1.3.1). For the case studied here, the force exerted by both the actuator and the wave elevation are uncorrelated pink multisines. The process can be summarized as

1. Execute forced oscillation experiments without waves to obtain a model of the intrinsic impedance as described in Section 2.1. The procedure can be applied when using either

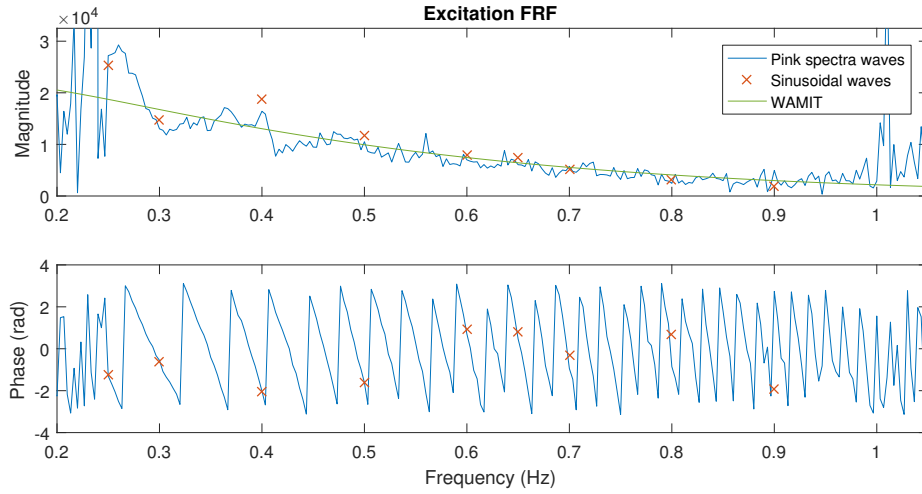


Figure 2.31: Excitation FRFs using sinusoidal waves compared to pink multisine and WAMIT.

parametric or nonparametric models for Z_i .

2. Execute the forced oscillation experiment in presence of waves. In this case, the available measurements are the actuator force (F_a), the buoy velocity (v) and the wave elevation (η).
3. By using the frequency domain equation of motion:

$$\hat{F}_e(\omega) + \hat{F}(\omega) = Z_i(\omega) \hat{V}(\omega), \quad \text{with} \quad \hat{F}_e(\omega) = H(\omega) \hat{\eta}(\omega), \quad (2.5)$$

it is possible to write the excitation FRF as function of the known quantities as:

$$H(\omega) = \frac{Z_i(\omega) \hat{V}(\omega) - \hat{F}(\omega)}{\hat{\eta}(\omega)} \quad (2.6)$$

The results of this analysis are shown in Figure 2.32. As can be seen, the results from this model separation approach compare quite well with the traditional diffraction tests and the numerical results.

2.3 WEC model

To characterize and quantify the performance of the models produced from Sections 2.1 and 2.2, a validation study has been performed. As is standard practice, a second set of data, not previously used in the system ID process, is used for the validation comparisons.

2.3.1 Radiation / diffraction model validation

The block diagram in Figure 2.33 shows the model of the WEC based on the classical radiation/diffraction scheme. The excitation FRF is denoted by H and the intrinsic impedance is de-

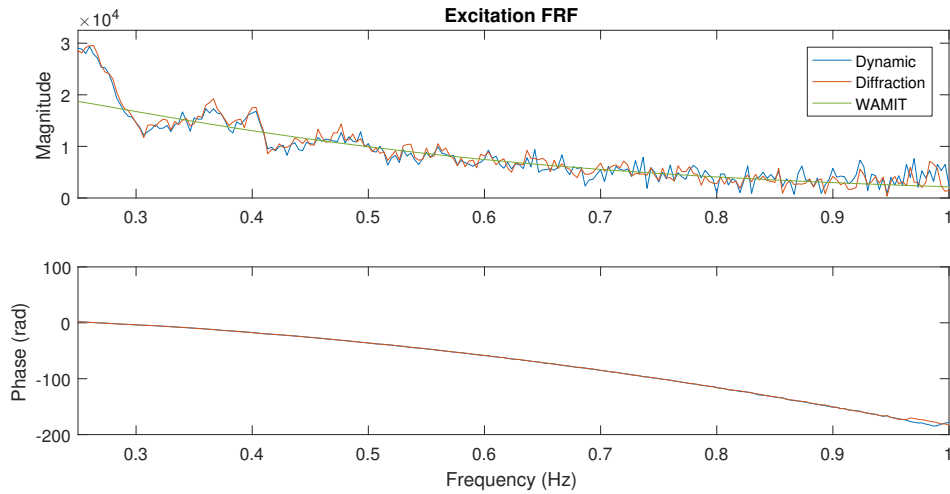


Figure 2.32: Comparison of excitation FRFs obtained using WAMIT, dedicated diffraction tests (“Diffraction”) and separation from radiation and dynamic tests (“Dynamic”).

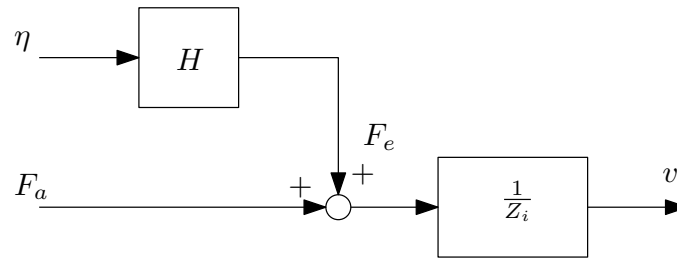


Figure 2.33: Block diagram of the WEC base on radiation/diffraction model. The wave elevation is denoted by η , the actuator force is F_a and the velocity is v .

noted by Z_i . The derivation of H is described in Section 2.2.1, while the derivation of the intrinsic impedance and radiation model are supplied in Section 2.1.2.1. In this case, the validation has been carried out using Bretschneider spectrum with $H_s = 0.155$ m and $T_p = 2.39$ s for the waves and an uncorrelated pink multisine signal for the actuator. The resulting measured and simulated velocity are shown in Figure 2.34. The model validation shows a fit of $1 - \text{NRMSE} = 71.6\%$.

2.3.2 MISO system ID (2-input/1-output)

In this section, the WEC is modeled as a MISO (multi-input, single-output) system and the identification of the parametric model is carried out using the subspace method implemented in the function `n4sid` from the MATLAB System Identification Toolbox. Two different MISO models are considered: Section 2.3.2.1 uses the wave elevation and actuator force for the system inputs while Section 2.3.2.2 uses a pressure measurement on the hull of the float and the actuator force as the inputs.

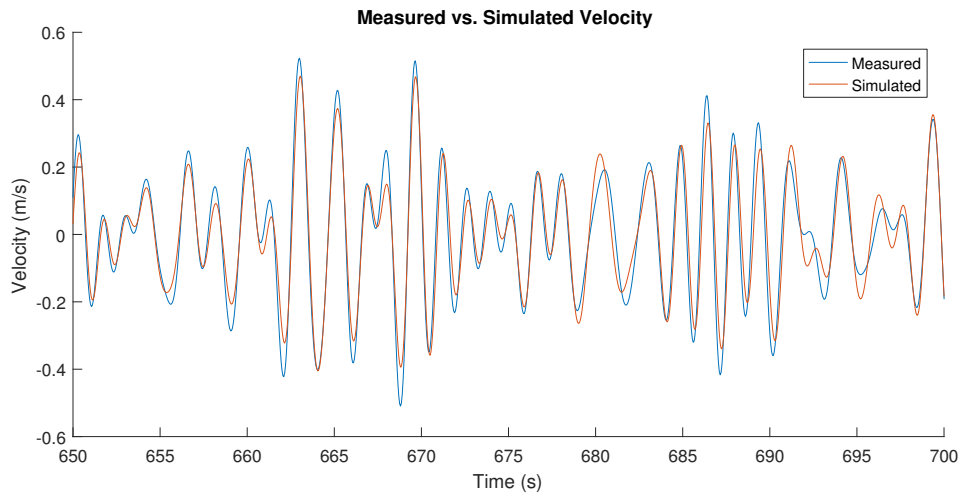


Figure 2.34: Radiation/diffraction model validation: time series detail of measured (experimental) velocity compared to simulated velocity ($1 - \text{NRMSE} = 71.6\%$).

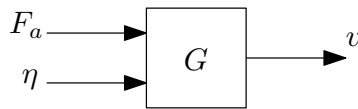


Figure 2.35: Block diagram for the 2-input, 1-output model structure: force and wave elevation are the inputs, velocity is the output.

2.3.2.1 MISO, wave elevation / actuator

A MISO model was developed using the wave elevation measurement from a wave probe (η) and the actuator force (F_a) as inputs for a model of the WEC velocity (v). Figure 2.35 provides an high level diagram of the system structure. The system ID has been carried out using an experiment where the waves have a Bretschneider spectra with $H_s = 0.121$ m and $T_p = 3.08$ s, and actuator is commanded with a band-limited white noise. The frequency response of the identified model is shown by the Bode plots in Figure 2.36. The validation of this model has been carried out using data from the experiment where both waves and actuator signal are pink multisines. The two inputs are depicted in Figures 2.29 (waves) and 2.2 (actuator). Figure 2.40 shows the comparison of simulated and measured velocity; in this case, the fit is $1 - \text{NRMSE} = 67\%$.

The wave probe used for the identification is located next to the buoy (“BuoyAssemblySenix10” - see Figure 1.25 and Table B.1). Signals from other probes in front of the buoy have also been used for system ID, but these produced poorer results. This may be due to the dispersive nature of the water waves propagation (i.e. dispersion relation), for which a nonlinear model may be required to obtain a better fitting.

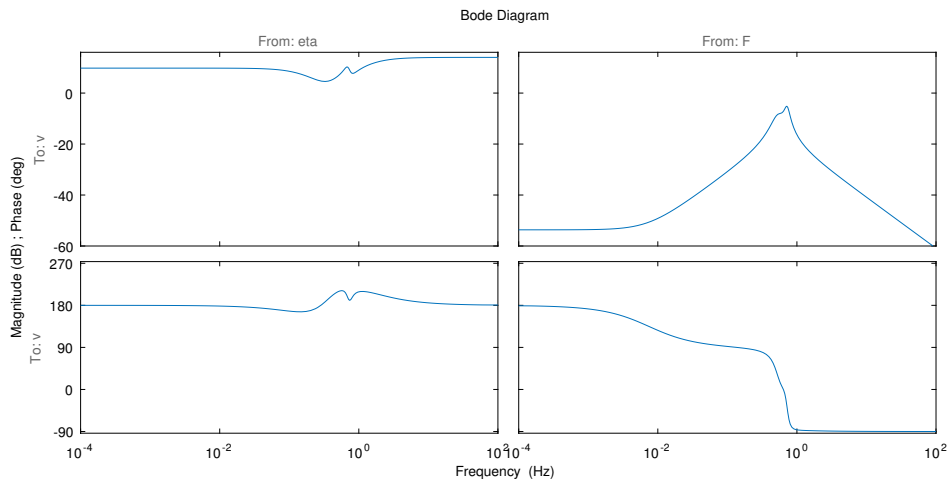


Figure 2.36: Bode plot of the 2-Input, 1-Output model for the WEC. The wave elevation is measured in inches and the force in kN.

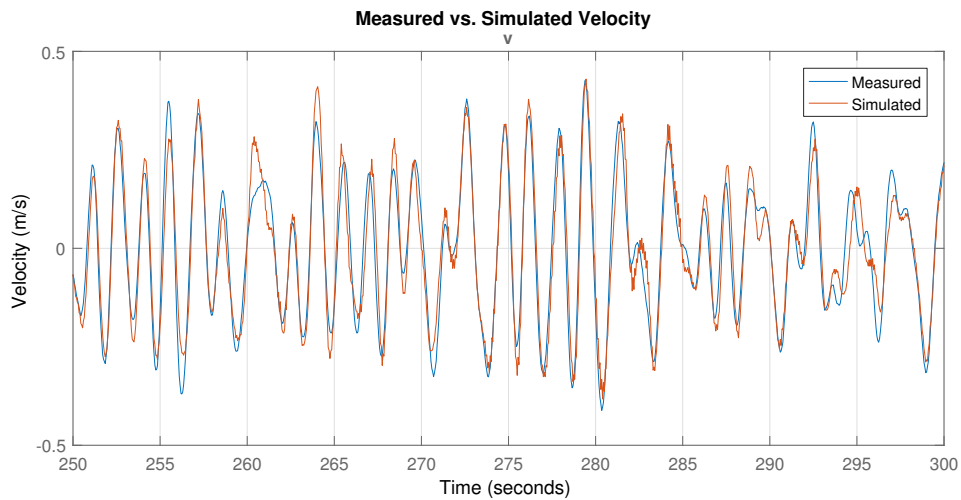


Figure 2.37: Comparison of measured and simulated velocities for the MISO, elevation / actuator model ($1 - \text{NRMSE} = 67\%$).

2.3.2.2 MISO, pressure / actuator

In this section, a second MISO model is developed and evaluated. Here, the inputs are considered to be the actuator force and the water pressure on the hull. They are measured, respectively, with the actuator load cell and a pressure transducer mounted on the hull of the device. The output of the system is again considered to be the heave velocity. This approach follows a logic similar to that used in [12], with the fundamental concept being that the excitation force of a wave is due to the pressure disturbance, not its free surface elevation. Figure 2.38 provides an high level diagram of the system structure. The system identification has been carried out using an experiment where the waves have a Bretschneider spectra with $H_s = 0.121$ m and $T_p = 3.08$ s, and actuator is commanded with a band-limited white noise signal. The frequency response of the identified model is shown by

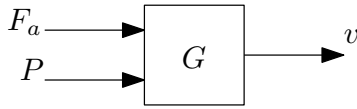


Figure 2.38: Block diagram for the 2-input, 1-output model structure: force and pressure are the inputs, velocity is the output.

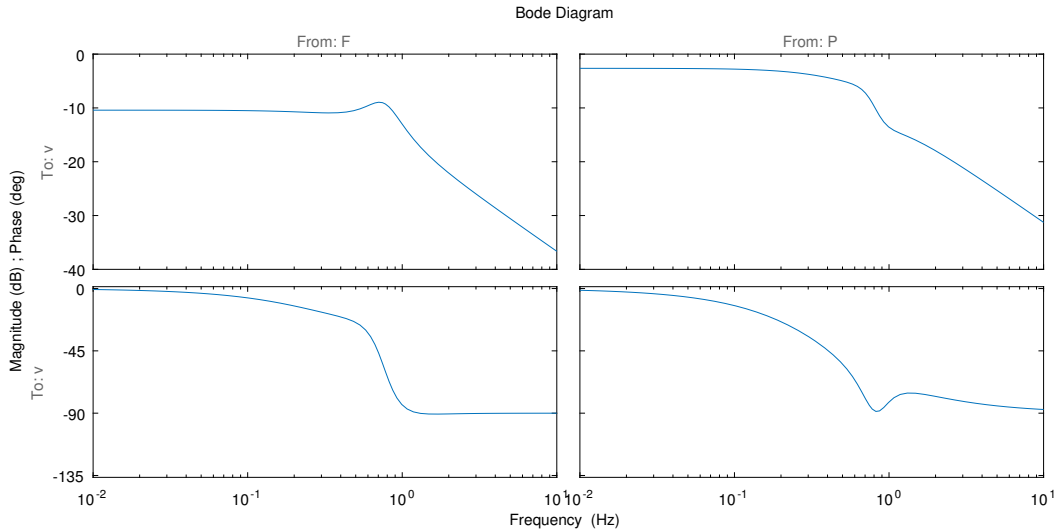


Figure 2.39: Bode plot of the 2-input, 1-output model for the WEC. The unit of the force is kN and of the pressure is kPa.

the Bode plots in Figure 2.39. The validation of the model depicted in Figure 2.39 has been carried out using data from an experiment where both waves and actuator signals are pink multisines (the wave and actuator signals are depicted in Figures 2.29 and 2.2 respectively). Figure 2.40 shows the comparison of simulated and measured velocity; in this case, the fit is $1 - \text{NRMSE} = 87\%$.

2.4 Conclusions

A number of system ID approaches have been applied for this study. Table 2.1 shows a summary of these models' validation performance. The MISO pressure/actuator model delivered the best performance. While this model does not retain the typical structure often used in WEC modeling (radiation/diffraction), it appears to provide the most accurate dynamics model of the system. In the end, this is the most critical factor for control design.

At a higher level, regardless of the model formulation used, the system ID approaches applied in this study have a number of a very attractive qualities over the monochromatic wave based approach which is often employed in model-scale testing. As discussed in Section 1.3.2, the use of periodic multisine input signals has a number of advantages. Compared against monochromatic

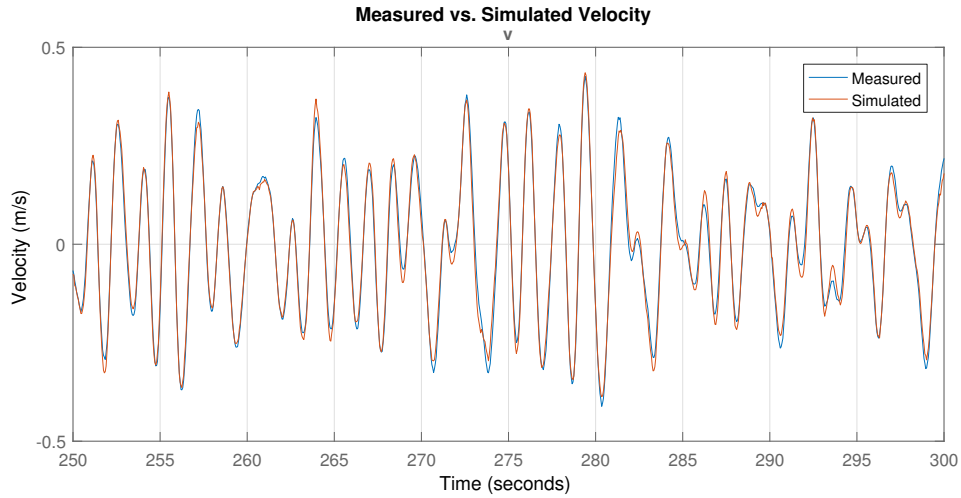


Figure 2.40: Comparison of measured and simulated velocities for the MISO, pressure / actuator model ($1 - \text{NRMSE} = 87\%$).

Table 2.1: Model validation performance comparison.

Model	Fit ($1 - \text{NRMSE}$)
Radiation/diffraction	71.6%
MISO, pressure / actuator	87.0%
MISO, wave elevation / actuator	67.2%

waves, multisine input signals allow for higher levels of frequency resolution to be obtained in less time. Periodic input signals allow for smoother wave spectra (see Figure 1.26), reduced spectral leakage, increased signal to noise ratios and a straightforward approach to nonlinearity detection (see Section 1.3.2 for further discussion).

Additionally, the process summarized in Section 2.2.3 lays the groundwork for a means to obtain dynamic models of full-scale WEC devices in an open ocean environment. This will likely prove to be an important step in realizing the benefits of advanced WEC control in commercial devices. While model-scale testing and the system ID processes considered in this study are essential to the design of a control algorithm for a WEC, this work alone cannot be relied upon for the success of a full-scale system. The leap from a foam and wood model, moored with springs, and actuated with a linear motor, to a full-scale WEC, built of steel, moored in 100 m of water, and actuated with a hydraulic system is substantial. The ability to perform at-sea system ID to tune a controller will be essential to maximizing the performance of a WEC device.

Chapter 3

Control performance comparison

In a previous study [13], a numerical WEC dynamics model was developed using a BEM tool. A set of control strategies were developed and the numerical model was used to compare their performance [3, 14]. This comparison, which considered a wide range of performance metrics, including power absorption, reactive power requirements, PTO force requirements and motion extents, showed the importance of incorporating the selection of a WEC control strategy into the larger design process. Decoupling control design from the rest of the WEC design process has the potential to substantially limit design options and therefore performance. For example, a WEC with a PTO unable to provide reactive control will be unable to implement a large set of control strategies. As a control strategy selection can both drive and be driven by other design considerations, it should ideally be incorporated early within the design process.

Here, we update the control strategy performance comparison first presented in [3]. The BEM-based model is replaced with the radiation / diffraction model developed and validated in Chapter 2. Seven control strategies were considered: resistive damping, complex conjugate control (CCC), latching, linear quadratic Gaussian (LQG), a proportional-derivative version of complex conjugate control (PDC3), linear model predictive control (MPC), and shape-based control (SB). Control tuning factors remained the same as in previous studies. For details on the design/implementation of these control strategies, please see Wilson et al. [3].

As with previous analyses [3, 14], controller performance was assessed for a wave climate based on NDBC 46050, which is located off the coast of Newport, OR [1]. The sea states selected to represent this location (see Wilson et al. [3] for methodology) are shown in Table 3.1. Table 3.2 summarizes the irregular wave control strategy performance results. All values are given as the average annual value for the quantity defined. Further, all units are metric and all results are shown in model scale (1/17). The quantities presented in Table 3.2 are defined as follows:

- Power production characteristics - Quantities relevant to power production.
 - Average power-in - Average annual power used to motor the device (i.e. “reactive power”).
 - Average power-net - Average annual net power from the device.
 - Average energy-stored - Average annual stored power (only necessary for reactive strategies). Storage is calculated as the amount of energy necessary to provide the

Table 3.1: List of the 17 irregular sea-states simulated to characterize controller performance for Newport, OR (NDBC 46050) deployment [1].

Sea-State index	Peak period, T_p [s]	Significant wave height, H_s [m]	Steepness, (H_m, T_m) [-]	Occurrence, Ξ [%]
1	1.00	0.0247	60	0
2	1.00	0.0148	100	0
3	1.00	0.0370	40	0
4	1.53	0.0871	40	18.5
5	2.00	0.0594	100	0
6	2.05	0.1039	60	17.2
7	2.25	0.1875	40	11.3
8	2.50	0.1545	60	0
9	2.50	0.0927	100	0
10	2.58	0.1194	82	21.1
11	2.89	0.2523	49	7.6
12	3.00	0.3337	40	0
13	3.03	0.1363	100	12.8
14	3.46	0.1283	138	9.2
15	3.60	0.3195	60	4.9
16	4.02	0.1320	180	5.8
17	4.86	0.1617	206	1.6

reactive power required by the control strategy without absorbing power from other sources (e.g. power from the electrical network).

- Power-in, peak[†]/RMS - Peak power-in divided by RMS power-in.
- Power-net, peak[†]/RMS - Peak power-net divided by RMS power-net.
- Total absolute power flow - Indication of stress on PTO. Is is calculated as the annual weighted average of the absolute value of the power flowing through the PTO.
- PTO requirement - Quantities relevant to PTO capability requirements.
 - PTO force, peak[†] - Peak force applied by PTO.
 - Slew rate requirements - Average annual rate change in force applied by PTO (i.e. $\frac{\partial F}{\partial t}$)
 - PTO force, RMS - RMS of force applied by PTO.
 - PTO Force, peak[†]/RMS - Peak PTO force divided by RMS PTO force.
- Mechanical loading - Measures of requirements for device device drive train structure (e.g., bearing surfaces, motor extension limits)
 - Oscillation amplitude, peak[†] - Peak of float vertical motion amplitude.

- Oscillation amplitude, $\text{peak}^\dagger/\text{RMS}$ - Peak of float vertical motion amplitude divided by RMS of float vertical motion amplitude.
- Oscillation velocity, peak^\dagger - Peak of float vertical velocity.
- Oscillation velocity, $\text{peak}^\dagger/\text{RMS}$ - Peak of float vertical velocity divided by RMS of float vertical velocity.
- Oscillation acceleration, peak^\dagger - Peak of float vertical velocity
- Oscillation acceleration, $\text{peak}^\dagger/\text{RMS}$ - Peak of float vertical acceleration divided by RMS of vertical acceleration.

[†]Here, the term “peak” refers to the 98th percentile of the identified response’s peaks.

The performance results seen in Table 3.2 show close agreement with those seen in [3]. This is expected, as the two numerical models show good agreement. Many of the differences seen in Table 3.2 result from the additional damping of the experimental system. Some control strategies do show a significant change in performance when compared with the previous assessment in [3] (e.g. shape-based control). This result shows the sensitivity of certain strategies to model uncertainties and highlights the need for retuning a control strategy based on experimental testing. On the other hand, certain controllers (linear controllers such as MPC and LQG) do not require human supervision for retuning. Consequently, their performance with this new experimentally-based model is not dramatically changed. Furthermore, this indicates that these controllers might be well-suited for a gain-scheduling approach (i.e. using a series of local linear models for different sea states).

Table 3.2: Performance comparison of control strategies in irregular waves.

	Resistive	CCC	Latching	LQG	PDC3	Linear MPC	SB
<i>Power production characteristics</i>							
Average power-in	0	237.5	0	48.9	67.3	95.6	21.0
Average power-net	15.1	49.0	29.8	39.0	25.7	44.2	16.9
Average energy-stored	0	212.1	0	29.2	57.9	72.5	10.2
Power-in, peak/RMS	0	5.8	0	5.6	5.3	5.6	5.3
Power-net, peak/RMS	7.3	36.2	6.2	14.8	22.0	20.3	13.6
Total absolute power flow	15.1	269.6	29.8	77.0	85.1	127.0	33.9
<i>PTO requirements</i>							
PTO force, peak	776	4039	968	1998	2331	2698	1218
Slew rate requirements	2.85E3	9.88E3	4.26E5	6.01E3	5.73E3	7.11E3	3.90E4
PTO force, RMS	313	2184	346	992	1219	1372	503
PTO Force, peak/RMS	2.44	1.85	2.80	2.17	1.91	1.97	2.42
<i>Mechanical loading</i>							
Oscillation amplitude, peak	0.05	0.23	0.12	0.13	0.13	0.17	0.08
Oscillation amplitude, peak/RMS	2.47	1.99	2.04	2.28	1.99	2.13	1.99
Oscillation velocity, peak	0.13	0.44	0.33	0.3	0.25	0.34	0.22
Oscillation velocity, peak/RMS	2.75	2.21	2.75	2.33	2.23	2.34	2.00
Oscillation acceleration, peak	0.36	0.96	0.45	0.77	0.49	0.80	0.69
Oscillation acceleration, peak/RMS	2.62	2.41	1.09	2.61	2.11	2.50	1.99

References

- [1] National Data Buoy Center (NDBC). Station 46050 (LLNR 641) - STONEWALL BANK - 20NM West of Newport, OR. National Oceanic and Atmospheric Administration (NOAA). [Online]. Available: http://www.ndbc.noaa.gov/station_history.php?station=46050
- [2] J. Hals, “Modelling and phase control of wave-energy converters,” PhD, Norwegian University of Science and Technology, Trondheim, Norway, 2010. [Online]. Available: <http://ntnu.diva-portal.org/smash/record.jsf?pid=diva2:403616>
- [3] D. Wilson, G. Bacelli, R. G. Coe, D. L. Bull, O. Abdelkhalik, U. A. Korde, and R. D. Robi-
nett III, “A comparison of WEC control strategies,” Sandia National Labs, Albuquerque, New
Mexico, Tech. Rep. SAND2016-4293, April 2016 2016.
- [4] D. L. Bull, R. G. Coe, M. Monda, K. Dullea, G. Bacelli, and D. Patterson, “Design of a
physical point-absorbing WEC model on which multiple control strategies will be tested at
large scale in the MASK basin,” in *International Offshore and Polar Engineering Conference
(ISOPE2015)*, Kona, HI, 2015.
- [5] W. Brownell, “Two new hydromechanics research facilities at the David Taylor Model Basin,”
Department Of The Navy: David Taylor Model Basin, Tech. Rep. 1690, 1962.
- [6] D. G. Goring and V. I. Nikora, “Despiking acoustic doppler velocimeter data,” *Journal of
Hydraulic Engineering*, vol. 128, no. 1, pp. 117–126, 2002.
- [7] J. Davidson, S. Giorgi, and J. V. Ringwood, “Linear parametric hydrodynamic
models for ocean wave energy converters identified from numerical wave tank
experiments,” *Ocean Engineering*, vol. 103, pp. 31 – 39, 2015. [Online]. Available:
<http://www.sciencedirect.com/science/article/pii/S0029801815001432>
- [8] S. Giorgi, J. Davidson, and J. V. Ringwood, “Identification of wave energy device models
from numerical wave tank data part 2: Data-based model determination,” *IEEE Transactions
on Sustainable Energy*, vol. 7, no. 3, pp. 1020–1027, July 2016.
- [9] R. Pintelon and J. Schoukens, *System identification: A frequency domain approach*. John
Wiley & Sons, 2012.
- [10] WAMIT, *WAMIT User Manual*, 7th ed., Chestnut Hill, MA, 2012. [Online]. Available:
<http://www.wamit.com/manual.htm>
- [11] T. Perez and T. I. Fossen, “A matlab toolbox for parametric identification of radiation-force
models of ships and offshore structures,” *Modeling, Identification and Control: A
Norwegian Research Bulletin*, vol. 30, no. 1, pp. 1–15, 2009. [Online]. Available:
<http://www.mic-journal.no/ABS/MIC-2009-1-1.asp>

- [12] O. Abdelkhalik, S. Zou, G. Bacelli, R. D. Robinett III, D. G. Wilson, and R. G. Coe, "Estimation of excitation force on wave energy converters using pressure measurements for feedback control," in *OCEANS2016*. Monterey, CA: IEEE, 2016.
- [13] R. G. Coe and D. L. Bull, "Nonlinear time-domain performance model for a wave energy converter in three dimensions," in *OCEANS2014*. St. John's, Canada: IEEE, 2014.
- [14] G. Bacelli, R. G. Coe, D. Wilson, O. Abdelkhalik, U. A. Korde, R. D. Robinett III, and D. L. Bull, "A comparison of WEC control strategies for a linear WEC model," in *METS2016*, Washington, D.C., April 2016.
- [15] D. Wilson, G. Bacelli, R. G. Coe, R. D. Robinett III, G. Thomas, D. Linehan, D. Newborn, and M. Quintero, "WEC and support bridge control structural dynamic interaction analysis," in *METS2016*, Washington, D.C., April 2016.

Appendix A

Testing Log & Procedures

A.1 Test Log

Table A.1 shows a log of the tests conducted with relevant parameters to describe the test. The Test ID listed in Table A.1 can be used to access the data publicly at <https://mhkdr.openei.org/submissions/151>.

Table A.1: Wave tank testing log.

Datetime	Test ID	DOF config	Actuator input type	Actuator freq [Hz]	Actuator amp	Wave input type	Wave freq [Hz]	Wave amp [m]	Test time [min]	Video file
2016/2/26 11:25 AM	001	1-DOF (heave)	None			Monochromatic	0.4	0.05	8	25
2016/2/26 11:38 AM	002	1-DOF (heave)	None			Monochromatic	0.5	0.05	8	26
2016/2/26 11:49 AM	003	1-DOF (heave)	None			Monochromatic	0.6	0.05	8	27
2016/2/26 12:06 PM	004	1-DOF (heave)	None			Monochromatic	0.65	0.05	8	28
2016/2/26 12:19 PM	005	1-DOF (heave)	None			Monochromatic	0.7	0.05	8	29
2016/2/26 12:33 PM	006	1-DOF (heave)	None			Monochromatic	0.8	0.05	8	30
2016/2/26 12:46 PM	007	1-DOF (heave)	None			Monochromatic	0.3	0.05	8	31
2016/2/26 1:00 PM	008	1-DOF (heave)	None			Monochromatic	0.25	0.05	8	32
2016/2/26 1:14 PM	009	1-DOF (heave)	None			Monochromatic	0.9	0.05	8	33
2016/2/26 2:25 PM	010	1-DOF (heave)	None			Pink multisine	$0.25 \leq f \leq 1.0$	gain = 1.00	28	36
2016/2/26 3:13 PM	011	1-DOF (heave)	None			Monochromatic	0.6	0.025	8	37
2016/2/26 3:36 PM	012	1-DOF (heave)	Pink multisine	$0.25 \leq f \leq 1.0$	gain = 1.00	Pink multisine	$0.25 \leq f \leq 1.0$	gain = 1.00	18	38
2016/2/29 11:14 AM	013	1-DOF (heave)	Stepped damping			Monochromatic	0.4	0.05	22	41
2016/2/29 11:42 AM	014	1-DOF (heave)	Stepped damping			Monochromatic	0.5	0.05	22	42
2016/2/29 12:19 PM	015	1-DOF (heave)	Stepped damping			Monochromatic	0.6	0.05	22	NA
2016/2/29 12:47 PM	016	1-DOF (heave)	Stepped damping			Monochromatic	0.6	0.05	22	44
2016/2/29 2:12 PM	017	1-DOF (heave)	Stepped damping			Monochromatic	0.25	0.05	22	47
2016/2/29 2:39 PM	018	1-DOF (heave)	Stepped damping			Monochromatic	0.3	0.05	22	48
2016/3/1 5:24 AM	019	1-DOF (heave)	Stepped damping			Bretschneider	0.564971751	0.069	53	50
2016/3/1 6:39 AM	020	1-DOF (heave)	Stepped damping			Bretschneider	0.418410042	0.0885	53	52
2016/3/1 8:50 AM	021	1-DOF (heave)	Constant damping			Bretschneider	0.25	0.096	38	55
2016/3/1 10:57 AM	022	1-DOF (heave)	Constant damping			Bretschneider	0.324675325	0.0605	38	NA
2016/3/1 11:44 AM	023	1-DOF (heave)	Constant damping			Bretschneider	0.418410042	0.0775	38	56
2016/3/1 12:33 PM	024	1-DOF (heave)	Constant damping			Bretschneider	0.564971751	0.069	38	57
2016/3/1 1:22 PM	025	1-DOF (heave)	Constant damping			Bretschneider	0.25	0.096	38	NA
2016/3/1 3:33 PM	026	1-DOF (heave)	Pink multisine	$0.25 \leq f \leq 1.0$	gain = 1.00	Pink multisine	$0.25 \leq f \leq 1.0$	gain = 1.00	33	60
2016/3/2 1:23 PM	027	1-DOF (heave)	White multisine	$0.25 \leq f \leq 1.0$	$P = 0.01$	None			15	none
2016/3/2 3:05 PM	028	1-DOF (heave)	White multisine	$0.25 \leq f \leq 1.0$	$P = 0.02$	None			15	72
2016/3/2 3:26 PM	029	1-DOF (heave)	White multisine	$0.25 \leq f \leq 1.0$	$P = 0.04$	None			15	73
2016/3/3 5:20 AM	030	1-DOF (heave)	Stepped damping			Bretschneider	0.564971751	0.069	53	76
2016/3/3 5:51 AM	031	1-DOF (heave)	Stepped damping			Bretschneider	0.564971751	0.069	53	78
2016/3/3 8:18 AM	032	1-DOF (heave)	Stepped damping			Bretschneider	0.324675325	0.1575	53	80
2016/3/3 12:10 PM	033	1-DOF (heave)	None			Chirp up	$4 \rightarrow 1$	0.05	63	83

Table A.1: Wave tank testing log (continued).

Datetime	Test ID	DOF config	Actuator input type	Actuator freq [Hz]	Actuator amp	Wave input type	Wave freq [Hz]	Wave amp [m]	Test time [min]	Video file
2016/3/3 1:25 PM	034	1-DOF (heave)	None			Chirp up	$4 \Rightarrow 1.43$	0.1	39	84
2016/3/3 2:41 PM	035	1-DOF (heave)	White multisine	$0.25 \leq f \leq 1.0$	$P = 0.01$	Bretschneider	0.25	0.192	33	86
2016/3/3 3:19 PM	036	1-DOF (heave)	White multisine	$0.25 \leq f \leq 1.0$	$P = 0.02$	Bretschneider	0.25	0.192	33	87
2016/3/3 3:55 PM	037	1-DOF (heave)	White multisine	$0.25 \leq f \leq 1.0$	$P = 0.04$	Bretschneider	0.25	0.192	18	88
2016/3/4 6:20 AM	038	1-DOF (heave)	Chirp up	$0.25 \Rightarrow 0.8$	$cf = 0.40$	None			33	90
2016/3/4 6:59 AM	039	1-DOF (heave)	Chirp down	$0.8 \Rightarrow 0.25$	$cf = 0.40$	None			33	91
2016/3/4 7:39 AM	040	1-DOF (heave)	Chirp up	$0.25 \Rightarrow 1.0$	$cf = 0.60$	None			33	92
2016/3/4 8:21 AM	041	1-DOF (heave)	Chirp down	$1.0 \Rightarrow 0.25$	$cf = 0.60$	None			33	93
2016/3/4 9:12 AM	042	1-DOF (heave)	Chirp up	$0.25 \Rightarrow 1.0$	$cf = 0.80$	None			33	94
2016/3/4 10:03 AM	043	1-DOF (heave)	Chirp up	$0.8 \Rightarrow 0.4$	$cf = 0.80$	None			18	95
2016/3/4 1:02 PM	044	1-DOF (heave)	Pink multisine	$0.25 \leq f \leq 0.8$	$gain = 1.20$	None			18	96
2016/3/4 1:25 PM	045	1-DOF (heave)	Pink multisine	$0.25 \leq f \leq 0.8$	$gain = 1.75$	None			18	97
2016/3/4 1:58 PM	046	1-DOF (heave)	Pink multisine	$0.25 \leq f \leq 1.0$	$gain = 0.75$	None			33	98
2016/3/4 2:39 PM	047	1-DOF (heave)	Pink multisine	$0.25 \leq f \leq 1.0$	$gain = 1.00$	None			33	100
2016/3/4 3:17 PM	048	1-DOF (heave)	Pink multisine	$0.25 \leq f \leq 1.0$	$gain = 1.50$	None			33	101
2016/3/7 5:43 AM	049	1-DOF (heave)	Monochromatic	0.25	$cf = 0.25$	None			5	104
2016/3/7 5:50 AM	050	1-DOF (heave)	Monochromatic	0.3	$cf = 0.25$	None			5	105
2016/3/7 5:57 AM	051	1-DOF (heave)	Monochromatic	0.4	$cf = 0.25$	None			5	106
2016/3/7 6:04 AM	052	1-DOF (heave)	Monochromatic	0.5	$cf = 0.25$	None			5	107
2016/3/7 6:13 AM	053	1-DOF (heave)	Monochromatic	0.5	$cf = 0.25$	None			5	108
2016/3/7 6:20 AM	054	1-DOF (heave)	Monochromatic	0.6	$cf = 0.25$	None			5	109
2016/3/7 6:26 AM	055	1-DOF (heave)	Monochromatic	0.65	$cf = 0.25$	None			5	110
2016/3/7 6:32 AM	056	1-DOF (heave)	Monochromatic	0.7	$cf = 0.25$	None			5	111
2016/3/7 6:39 AM	057	1-DOF (heave)	Monochromatic	0.8	$cf = 0.25$	None			5	112
2016/3/7 6:45 AM	058	1-DOF (heave)	Monochromatic	0.9	$cf = 0.25$	None			5	113
2016/3/7 6:53 AM	059	1-DOF (heave)	Monochromatic	1	$cf = 0.25$	None			5	114
2016/3/7 7:00 AM	060	1-DOF (heave)	Monochromatic	0.25	$cf = 0.50$	None			5	115
2016/3/7 7:06 AM	061	1-DOF (heave)	Monochromatic	0.3	$cf = 0.50$	None			5	116
2016/3/7 7:12 AM	062	1-DOF (heave)	Monochromatic	0.4	$cf = 0.50$	None			5	117
2016/3/7 7:18 AM	063	1-DOF (heave)	Monochromatic	0.5	$cf = 0.50$	None			5	118
2016/3/7 7:25 AM	064	1-DOF (heave)	Monochromatic	0.6	$cf = 0.50$	None			5	119
2016/3/7 7:32 AM	065	1-DOF (heave)	Monochromatic	0.65	$cf = 0.50$	None			5	120

Table A.1: Wave tank testing log (continued).

Datetime	Test ID	DOF config	Actuator input type	Actuator freq [Hz]	Actuator amp	Wave input type	Wave freq [Hz]	Wave amp [m]	Test time [min]	Video file
2016/3/7 7:40 AM	066	1-DOF (heave)	Monochromatic	0.7	cf = 0.50	None			5	121
2016/3/7 7:46 AM	067	1-DOF (heave)	Monochromatic	0.8	cf = 0.50	None			5	122
2016/3/7 7:52 AM	068	1-DOF (heave)	Monochromatic	0.9	cf = 0.50	None			5	123
2016/3/7 8:02 AM	069	1-DOF (heave)	Monochromatic	1	cf = 0.50	None			5	124
2016/3/7 8:08 AM	070	1-DOF (heave)	Monochromatic	0.25	cf = 0.75	None			5	125
2016/3/7 8:16 AM	071	1-DOF (heave)	Monochromatic	0.3	cf = 0.75	None			5	126
2016/3/7 8:23 AM	072	1-DOF (heave)	Monochromatic	0.4	cf = 0.75	None			5	127
2016/3/7 8:30 AM	073	1-DOF (heave)	Monochromatic	0.5	cf = 0.75	None			5	128
2016/3/7 8:43 AM	074	1-DOF (heave)	Monochromatic	0.6	cf = 0.75	None			5	129
2016/3/7 8:50 AM	075	1-DOF (heave)	Monochromatic	0.65	cf = 0.75	None			5	130
2016/3/7 8:57 AM	076	1-DOF (heave)	Monochromatic	0.65	cf = 0.75	None			5	131
2016/3/7 9:05 AM	077	1-DOF (heave)	Monochromatic	0.7	cf = 0.75	None			5	132
2016/3/7 9:12 AM	078	1-DOF (heave)	Monochromatic	0.8	cf = 0.75	None			5	133
2016/3/7 9:19 AM	079	1-DOF (heave)	Monochromatic	0.9	cf = 0.75	None			5	134
2016/3/7 9:27 AM	080	1-DOF (heave)	Monochromatic	1	cf = 0.75	None			5	135
2016/3/7 12:09 PM	081	1-DOF (heave)	White multisine	$0.25 \leq f \leq 1.0$	gain = 1.00	None			15	138
2016/3/7 12:31 PM	082	1-DOF (heave)	White multisine	$0.25 \leq f \leq 1.0$	gain = 1.50	None			15	139
2016/3/7 12:55 PM	083	1-DOF (heave)	White multisine	$0.25 \leq f \leq 1.0$	gain = 0.50	None			15	140
2016/3/7 1:37 PM	084	1-DOF (heave)	White multisine	$0.25 \leq f \leq 1.0$	gain = 1.25	None			15	143
2016/3/7 1:56 PM	085	1-DOF (heave)	White multisine	$0.25 \leq f \leq 1.0$	gain = 0.75	None			15	144
2016/3/7 2:16 PM	086	1-DOF (heave)	Pink multisine	$0.25 \leq f \leq 1.0$	gain = 1.00	None			15	145
2016/3/7 2:35 PM	087	1-DOF (heave)	Pink multisine	$0.25 \leq f \leq 1.0$	gain = 1.50	None			15	146
2016/3/7 2:52 PM	088	1-DOF (heave)	Pink multisine	$0.25 \leq f \leq 1.0$	gain = 0.50	None			15	147
2016/3/7 3:12 PM	089	1-DOF (heave)	Pink multisine	$0.25 \leq f \leq 1.0$	gain = 2.00	None			15	149
2016/3/7 3:31 PM	090	1-DOF (heave)	Pink multisine	$0.25 \leq f \leq 1.0$	gain = 0.75	None			15	150
2016/3/7 3:48 PM	091	1-DOF (heave)	Pink multisine	$0.25 \leq f \leq 1.0$	gain = 1.25	None			15	151
2016/3/8 5:10 AM	092	1-DOF (heave)	Pink multisine	$0.25 \leq f \leq 1.0$	gain = 1.00	Bretschneider	0.324675325	0.121	18	152
2016/3/8 6:30 AM	093	1-DOF (heave)	Pink multisine	$0.25 \leq f \leq 1.0$	gain = 2.00	Bretschneider	0.324675325	0.121	18	155
2016/3/8 6:56 AM	094	1-DOF (heave)	Pink multisine	$0.25 \leq f \leq 1.0$	gain = 1.00	Bretschneider	0.418410042	0.115	18	156
2016/3/8 7:21 AM	095	1-DOF (heave)	Pink multisine		gain = 0.50	Bretschneider	0.418410042	0.0575	18	157
2016/3/8 7:45 AM	096	1-DOF (heave)	Pink multisine	$0.25 \leq f \leq 1.0$	gain = 2.00	Bretschneider	0.418410042	0.115	18	158
2016/3/8 8:09 AM	097	1-DOF (heave)	Pink multisine	$0.25 \leq f \leq 1.0$	gain = 1.00	Bretschneider	0.25	0.192	18	159

Table A.1: Wave tank testing log (continued).

Datetime	Test ID	DOF config	Actuator input type	Actuator freq [Hz]	Actuator amp	Wave input type	Wave freq [Hz]	Wave amp [m]	Test time [min]	Video file
2016/3/8 8:40 AM	098	1-DOF (heave)	Pink multisine		gain = 0.50	Bretschneider	0.25	0.096	18	160
2016/3/8 9:06 AM	099	1-DOF (heave)	Pink multisine		gain = 0.50	Bretschneider	0.25	0.096	18	161
2016/3/8 10:35 AM	100	1-DOF (heave)	Constant damping			Bretschneider	0.418410042	0.0775	33	162
2016/3/8 11:27 AM	101	1-DOF (heave)	Constant damping			Bretschneider	0.324675325	0.0605	33	163
2016/3/8 12:09 PM	102	1-DOF (heave)	White multisine	$0.25 \leq f \leq 1.0$	$P = 0.005$	Bretschneider	0.324675325	0.121	33	164
2016/3/8 12:49 PM	103	1-DOF (heave)	White multisine	$0.25 \leq f \leq 1.0$	$P = 0.010$	Bretschneider	0.324675325	0.121	33	165
2016/3/8 1:30 PM	104	1-DOF (heave)	White multisine	$0.25 \leq f \leq 1.0$	$P = 0.100$	Bretschneider	0.324675325	0.121	33	166
2016/3/8 2:08 PM	105	1-DOF (heave)	White multisine	$0.25 \leq f \leq 1.0$	$P = 0.200$	Bretschneider	0.324675325	0.121	33	167
2016/3/8 2:49 PM	106	1-DOF (heave)	White multisine	$0.25 \leq f \leq 1.0$	$P = 0.200$	Bretschneider	0.25	0.192	33	168
2016/3/8 3:30 PM	107	1-DOF (heave)	White multisine	$0.25 \leq f \leq 1.0$	$P = 0.040$	Bretschneider	0.418410042	0.155	33	169
2016/3/9 5:22 AM	108	1-DOF (heave)	White multisine	$0.25 \leq f \leq 1.0$	$P = 0.100$	Bretschneider	0.418410042	0.155	33	170
2016/3/9 6:37 AM	109	1-DOF (heave)	Pink multisine	$0.25 \leq f \leq 1.0$	gain = 1.00	Pink multisine	$0.25 \leq f \leq 1.0$	gain = 1.00	18	173
2016/3/9 6:58 AM	110	1-DOF (heave)	Pink multisine	$0.25 \leq f \leq 1.0$	gain = 0.50	Pink multisine	$0.25 \leq f \leq 1.0$	gain = 1.00	18	174
2016/3/9 7:20 AM	111	1-DOF (heave)	Pink multisine	$0.25 \leq f \leq 1.0$	gain = 2.00	Pink multisine	$0.25 \leq f \leq 1.0$	gain = 1.00	18	175
2016/3/9 7:41 AM	112	1-DOF (heave)	Pink multisine	$0.25 \leq f \leq 1.0$	gain = 1.00	Pink multisine	$0.25 \leq f \leq 1.0$	gain = 2.00	18	176
2016/3/9 8:04 AM	113	1-DOF (heave)	Pink multisine	$0.25 \leq f \leq 1.0$	gain = 0.50	Pink multisine	$0.25 \leq f \leq 1.0$	gain = 2.00	18	177
2016/3/9 8:26 AM	114	1-DOF (heave)	Pink multisine	$0.25 \leq f \leq 1.0$	gain = 2.00	Pink multisine	$0.25 \leq f \leq 1.0$	gain = 2.00	18	178
2016/3/9 8:55 AM	115	1-DOF (heave)	Pink multisine, reseeded	$0.25 \leq f \leq 1.0$	gain = 2.00	Pink multisine	$0.25 \leq f \leq 1.0$	gain = 1.00	18	179
2016/3/9 9:17 AM	116	1-DOF (heave)	Pink multisine, reseeded	$0.25 \leq f \leq 1.0$	gain = 0.50	Pink multisine	$0.25 \leq f \leq 1.0$	gain = 1.00	18	180
2016/3/9 10:54 AM	117	1-DOF (heave)	Pink multisine, reseeded	$0.25 \leq f \leq 1.0$	gain = 1.00	Pink multisine	$0.25 \leq f \leq 1.0$	gain = 1.00	18	181

A.2 Procedures

A.2.1 Test procedures

1. Confirm wave setting
2. Confirm actuator setting
3. Start actuator control and data-logging via SNL Simulink PC
4. Start waves (via radio)
5. Waves end (at pre-determined time)
6. End actuator control and data-logging via SNL Simulink PC

A.2.2 Entrance criteria

1. The following entrance criteria must be met in order to begin testing:
2. The wave sensors must all be mounted and display the correct polarity, vertical positive.
3. The wave conditions must be agreed upon and the fronts-files created.
4. Confirm actuator control setting
5. The wave experiment files must be generated and saved on to the wavemaker computer.
6. Sample data collects of all the systems will be conducted; verify that GPS time is being recorded on each system.
7. Confirm the water integrity of the buoy and electronics near the water line.

A.2.3 Exit criteria

1. The following criteria will be used to judge successful completion of the test:
2. All the critical data channels must be operational throughout the testing matrix.
3. All the collected data and testing logs must be backed up.
4. All the primary top-level objectives must be completed.

A.2.4 General daily procedures

1. The following is a general procedure for the beginning of each test day:
2. Stand up the wavemaker and allow the tank to settle for 30 minutes.
3. Ensure the RNLC system is operational and communicating with all DAQs.
4. Check device waterline
5. Power-up actuator
6. Check that contact switch is Off
7. Set Aux. Box switch to Charge
8. Turn battery switch to On position
9. Check voltage level on CAN display
10. Check for zero value of actuator/actuator lock-out load cell
11. Align/Ensure the bridge and carriage to prepare for the first measurement of the day.
12. Ensure all the data channels are operational.
13. Make sure all test engineers have operational radios for communication.
14. Confirm all the data channels from the wavemaker system are being collected and saved to the correct folder prior to each wave run.
15. Daily logs will be kept marking the start and stop time of each run along with notes identifying any discrepancies identified during testing.

A.3 Safety analysis

Extensive safety engineering was conducted to insure the safety of the project team during both bench-testing and test at the MASK basin. The failure modes effects analysis from the Advanced WEC Dynamics and Controls safety procedures is shown in Table A.2.

Table A.2: Failure modes effects analysis from the Advanced WEC Dynamics and Controls safety procedures.

Work Element Phase	System or Component	Failure Mode	Single Point Failure (Y or N)	Hazard Effect	Consequence	Engineered Controls	Administrative controls	Personal Protective Equipment (PPE)	Actions
PMT Assembly	Hand and power tools	Human error / tool failure	N	Pinching, blow to extremities	Personal injury		TWD	Safety glasses, safety shoes	Replace tool
	Heavy lifting	Human error	N	Pinching; muscle strain	Personal injury		TWD	Work gloves, safety shoes	Utilize proper lifting techniques and utilize other personnel or appropriate equipment for lifting.
Float Assembly	Hand and power tools	Human error / tool failure	N	Pinching, blow to extremities	Personal injury		TWD	Safety glasses	Replace tool
	Heavy lifting	Human error	N	Pinching; muscle strain	Personal injury		TWD	Work gloves, safety shoes	Utilize proper lifting techniques and utilize other personnel or appropriate equipment for lifting.
Weldment/ground plate mate	See Actions Notes								Carderock will perform this task.
PTO install	Hand and power tools	Human error / tool failure	N	Pinching	Personal injury		TWD	Safety glasses, safety shoes, Hard hat	Replace tool
	Heavy Lifting	Human error	N	Pinching; muscle strain	Personal injury		TWD	Work gloves, safety boots	Utilize proper lifting techniques and utilize other personnel or appropriate equipment for lifting.
	Magnetic Slider	Human Error	N	Pinching	Personal injury		TWD	Work gloves, protective foam tubes	Magnetic sliders stored and handled with protective foam tubes surrounding sliders. Use of work gloves while handling sliders. Keep metallic objects away from magnet slider.
	Magnetic Slider	Assumption	N	magnetic field effects to medical devices	Personal injury		Signage, TWD	Distance	IH analysis and assessed a distance of 2 feet.
Weldment to bridge	See Actions Notes								Carderock will perform this task.
Float install	Barge & punt (boat)	Human error or barge & punt failure	N	Fall into water	Personal injury		Carderock Safety Procedures	Certified PFD	Follow Carderock procedures; Carderock personnel run the Barge & punt
	Hand and power tools	Human error / tool failure	N	Pinching, blow to extremities	Personal injury		TWD	Safety glasses, safety shoes, Work gloves, Hard hat	Replace tool
	Elevated work	Human error	N	Fall	Personal injury	Weldment platform / Railings	TWD	Safety glasses, safety shoes, Hard hat, PFD	Personnel stay within Weldment platform and railings.
Ballast & Deballast of float	Heavy lifting	Human error	N	Pinching; muscle strain	Personal injury		TWD	Work gloves, safety shoes	Utilize proper lifting techniques and utilize other personnel or appropriate equipment for lifting.
	Bending over	Human error	N	fall into float	Personal injury	Harness			Harness used to prevent fall into float due to bending over to add or remove 10lb ballast weights. Float will be secured to the barge/punt to avoid separation.
DAQ installation and operations	Hand and power tools	Human error / tool failure	N	Pinching, blow to extremities	Personal injury		TWD	Safety glasses	Replace tool
	Electronic tools	Human error / tool failure	N	Inability to trouble shoot equipment	Equipment Failure		TWD	Safety glasses	Replace tool
	Elevated work	Human error	N	Fall	Personal injury	Bridge Cat-Walk and Railings	TWD	Safety glasses	Personnel stay within Bridge Cat-Walk and any area on bridge that has railings.
General operation	Carderock general industrial facility	General hazards in industrial facility	N	Slips, trips & falls	Personal injury		TWD & Carderock Safety Procedures	Safety glasses	Safety Instructions Carderock, General awareness of hazards around working area, follow all signage and safety procedures
Lock-out	Barge & punt (boat)	Human error or barge & punt failure	N	Fall into water	Personal injury	Harness	Carderock Safety Procedures	Certified PFD	Follow Carderock procedures; Carderock personnel run the Barge & punt
	Hand and power tools	Human error / tool failure	N	Pinching, blow to extremities	Personal injury		TWD	Safety glasses	Replace tool
	Elevated work	Human error	N	Fall	Personal injury	Weldment platform / Railings	TWD	Safety glasses, safety shoes, Hard hat, PFD	Personnel stay within Weldment platform and railings.
Measurements of Bridge Movement	Class 3a Laser	Human error	N	Injury due to prolonged exposure.	Personal injury	Hardware installation	TWD		Safety Instructional signage and safety procedures, General awareness of hazards around working area.

Appendix B

Sensors Locations and Calibrations

Table B.1 lists the locations of wave sensors within the MASK basin. The orientation of the x and y axes used in this description can be referenced from Figures 1.24 and 1.9. Within the basin, the x -axis runs South away from the long bank of wavemakers and the y -axis runs East away from the short bank of wavemakers. Table B.2 lists the calibration factors ($y = mx + b$; m : slope, b : offset) for all non-WaveWire sensors. WaveWire calibration factors are shown in Table B.3. Table B.4 shows the locations of pressure sensors of the float. The calibration parameters for the pressure sensors are shown in Table B.5. Table B.6 shows the calibration factors for the load cells used in testing.

Table B.1: Wave sensor locations within MASK basin.

Name	Type	x location (m)	y location (m)
Float	Float	37.9	78.5
Staff1	Capacitive	19.7	28.9
Staff2	Capacitive	20.2	29.1
Staff3	Capacitive	20.1	29.6
Staff4	Capacitive	19.4	29.3
Staff5	Capacitive	20.4	28.8
Staff6	Capacitive	20.6	29.6
Staff7	Capacitive	20.0	30.1
Staff8	Capacitive	19.1	29.1
Staff9	Capacitive	20.9	29.9
Staff10	Capacitive	19.2	30.4
Staff11	Capacitive	19.0	29.5
Staff12	Capacitive	19.3	28.6
CarriageSonicSW	Sonic	28.5	29.1
CarriageSonicNW	Sonic	22.2	29.8
CarriageSonicSE	Sonic	30.3	34.1
CarriageSonicNE	Sonic	24.4	36.3
BridgeProbe1	Sonic	42.6	92.0
BridgeProbe3	Sonic	33.5	66.9
BridgeProbe4	Sonic	41.7	59.9
BridgeProbe5	Sonic	25.3	44.3

Table B.1: Wave sensor locations within MASK basin (continued).

Name	Type	<i>x</i> location (m)	<i>y</i> location (m)
BridgeProbe6	Sonic	33.4	37.1
BridgeProbe8	Sonic	27.2	20.1
BuoyAssemblySenix8	Sonic	39.5	77.0
BuoyAssemblySenix9	Sonic	40.6	76.7
BuoyAssemblySenix10	Sonic	41.1	76.5
BuoyAssemblySenix14	Sonic	41.9	76.2
BuoyAssemblySenix15	Sonic	40.9	75.8
SAASenix22	Sonic	20.3	78.1
SAASenix24	Sonic	19.4	77.7
SAASenix13	Sonic	21.1	78.6
SAASenix19	Sonic	21.0	76.9
SAASenix23	Sonic	21.0	77.4
WaveWire1	Resistive	26.0	50.5
WaveWire2	Resistive	25.9	50.6
WaveWire3	Resistive	26.0	50.7
WaveWire4	Resistive	26.1	50.4
WaveWire5	Resistive	25.7	50.7
WaveWire6	Resistive	25.5	50.8
WaveWire7	Resistive	25.2	50.9
WaveWire8	Resistive	24.9	51.0
WaveWire9	Resistive	24.5	51.1
WaveWire10	Resistive	24.1	51.3
WaveWire11	Resistive	26.1	50.9
WaveWire12	Resistive	26.1	51.2
WaveWire13	Resistive	26.1	51.6
WaveWire14	Resistive	26.1	52.1
WaveWire15	Resistive	26.1	52.6
WaveWire16	Resistive	26.3	50.6
WaveWire17	Resistive	26.4	50.6
WaveWire18	Resistive	26.6	50.7
WaveWire19	Resistive	26.9	50.7
WaveWire20	Resistive	27.3	50.9
WaveWire21	Resistive	28.0	51.1
WaveWire22	Resistive	26.2	50.2
WaveWire23	Resistive	26.4	49.9
WaveWire24	Resistive	26.6	49.6
WaveWire25	Resistive	26.8	49.3
WaveWire26	Resistive	27.2	48.8
WaveWire27	Resistive	25.8	50.4
WaveWire28	Resistive	25.7	50.2
WaveWire29	Resistive	25.6	50.1

Table B.1: Wave sensor locations within MASK basin (continued).

Name	Type	<i>x</i> location (m)	<i>y</i> location (m)
WaveWire30	Resistive	25.5	49.9
WaveWire31	Resistive	25.1	49.5
WaveWire32	Resistive	24.7	48.9

Table B.2: General wave sensor calibration factors.

Sensor	Slope	Offset
SAA Senix #22	-4.437	18.2433
SAA Senix #24	-4.4485	17.7522
SAA Senix #13	-4.4273	18.4708
SAA Senix #19	-4.4377	18.2362
SAA Senix #23	-4.4369	18.4253
Bridge Probe 1	-4.4291	22.6128
Bridge Probe 3	-4.4325	23.7689
Bridge Probe 4	-4.314	23.2929
Bridge Probe 5	-4.423	22.6315
Bridge Probe 6	-4.433	22.4565
Bridge Probe 8	-4.4352	23.3338
Buoy Assembly Senix #8	-4.4435	24.5153
Buoy Assembly Senix #9	-4.4417	24.3976
Buoy Assembly Senix #10	-4.4807	24.8301
Buoy Assembly Senix #14	-4.429	24.198
Buoy Assembly Senix #15	-4.4267	24.3873
Staff #1	15.7085812	-40.2406
Staff #2	15.7120204	-40.2712
Staff #3	15.7424631	-40.0737
Staff #4	15.6624417	-39.9403
Staff #5	15.773867	-41.0644
Staff #6	15.7251873	-40.5765
Staff #7	15.6688842	-39.9257
Staff #8	15.7067437	-40.3036
Staff #9	15.7966151	-40.4066
Staff #10	15.6113495	-39.9481
Staff #11	15.7090018	-40.2746
Staff #12	15.7255004	-40.5354
Carriage Sonic SW	-4.0339	19.3528
Carriage Sonic NW	-4.1393	27.1757
Carriage Sonic SE	-4.0353	18.9297
Carriage Sonic NE	-4.0272	19.056

Table B.3: WaveWire sensor calibration factors.

Sensor	CableRes	CalSet	ZeroSet	CalError
1	0.955948	1.76514	0.635288	0.00678396
2	0.955948	1.67189	0.659994	0.00950901
3	0.955948	1.74105	0.639889	0.00993676
4	0.955948	1.63175	0.644182	0.014288
5	0.955948	1.64801	0.641573	0.008205
6	0.955948	1.6657	0.637642	0.0121867
7	0.955948	1.66651	0.651231	0.00687442
8	0.955948	1.65789	0.651636	0.0116865
9	0.955948	1.67976	0.65075	0.01364
10	0.955948	1.71228	0.644313	0.0119244
11	0.955948	1.68286	0.6366	0.0100827
12	0.955948	1.63595	0.639887	0.0147378
13	0.955948	1.67842	0.645583	0.00819785
14	0.955948	1.65985	0.653153	0.00926284
15	0.955948	1.68315	0.639827	0.0119436
16	0.955948	1.59522	0.661756	0.0113031
17	0.955948	1.68548	0.638253	0.00742515
18	0.955948	1.61068	0.649676	0.00781937
19	0.955948	1.63444	0.646849	0.00964963
20	0.955948	1.67959	0.639891	0.0122841
21	0.955948	1.61328	0.649964	0.00937961
22	0.955948	1.62644	0.653829	0.00987444
23	0.955948	1.65763	0.644157	0.00644939
24	0.955948	1.63204	0.646429	0.00943805
25	0.955948	1.63411	0.651057	0.00306208
26	0.955948	1.58049	0.654232	0.00984414
27	0.955948	1.65539	0.647371	0.0135908
28	0.955948	1.70447	0.635573	0.00783403
29	0.955948	1.69478	0.636678	0.00459993
30	0.955948	1.6362	0.647923	0.012946
31	0.955948	1.66243	0.64943	0.00644979
32	0.955948	1.65024	0.652972	0.00973834

Table B.4: Locations of the Pressure Sensors with respect to the center of the base.

Sensor	Model	Radial Orientation	Radial location (mm)	Vertical location (mm)
PT01	PX-459	0°	412	41
PT02	TDH-40	0°	549	137
PT03	TDH-40	0°	686	233
PT04	Slam Panel	0°	823	330
PT05	PX-459	0°	882	408
PT06	TDH-40	0°	882	508
PT07	Slam Panel	0°	882	643
PT08	TDH-40	0°	820	729
PT09	TDH-40	0°	695	729
PT44	Amphenol NPI	4°	823	330
PT47	Amphenol NPI	4°	882	643
PT21	TDH-40	20°	412	41
PT22	TDH-40	20°	549	137
PT23	PX-459	20°	686	233
PT24	TDH-40	20°	823	330
PT25	TDH-40	20°	882	407
PT26	TDH-40	20°	882	507
PT27	TDH-40	20°	882	643
PT28	Slam Panel	20°	820	729
PT29	TDH-40	20°	695	729
PT248	Amphenol NPI	24°	820	729
PT61	TDH-40	60°	412	41
PT62	TDH-40	60°	549	137
PT63	PX-459	60°	686	233
PT64	TDH-40	60°	823	330
PT65	TDH-40	60°	882	407
PT66	TDH-40	60°	882	507
PT67	TDH-40	60°	882	643
PT68	TDH-40	60°	820	729
PT69	TDH-40	60°	695	729

Table B.5: Pressure transducer calibration curves.

Sensor	Model	Calibration Slope	Calibration Offset
PT01	PX-459	9.10	-8.85
PT02	TDH-40		-NA-
PT03	TDH-40	8.93	-8.57
PT04	(Empty)		-NA-
PT05	PX-459	9.19	-8.48
PT06	TDH-40	9.10	-8.38
PT21	TDH-40	8.93	-8.70
PT22	TDH-40	8.93	-8.73
PT23	PX-459	9.02	-8.70
PT24	TDH-40	8.84	-8.64
PT25	TDH-40	8.93	-8.36
PT26	TDH-40	8.93	-8.29
PT61	TDH-40	8.93	-8.13
PT62	TDH-40	9.02	-8.75
PT63	PX-459	9.10	-8.76
PT64	TDH-40	8.93	-8.56
PT65	TDH-40	9.02	-8.13
PT66	TDH-40	9.54	-8.44

Table B.6: Calibration curves for test load cells.

Location/usage	Model	Serial number	Calibration slope	Calibration offset
Heave lock-out	LPO-2K	SN-321321	1039.0	-22.47
(spare)	LPO-2K	SN-327196	1041.0	-256.9
Actuator	MLP-750	NA	322.9	90.33
Surge	MLP-750	SN-312549	389.6	-12.30
Pitch	MLP-750	SN-332462	322.4	-34.08

Appendix C

Structural Dynamics Report

As part of the preparations for this test, a structural dynamics analysis was completed by ATA Engineering. This analysis included both numerical modeling and empirical analyses. A copy of the final report summarizing this work is included here. A subsequent analysis on methods to limit control-structure interaction was performed by Wilson et al. [15].



ATA Project No. 65402
Customer PO No. 1642952
January 28, 2016

Final Report for
Test and Analysis Evaluation of MASK Basin
Bridge Structural Dynamics for Advanced
WEC Controls Hardware

Prepared for

Sandia National Laboratories
Water Power Technologies (Org. 6122)
PO Box 5800
Albuquerque, New Mexico 87185

Prepared by

ATA Engineering, Inc.
13290 Evening Creek Drive South, Suite 250
San Diego, California 92128

Prepared by:

Daniel Linehan
Senior Project Engineer

Gareth R. Thomas, Ph.D.
Consultant

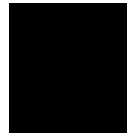
Reviewed by:

Ralph D. Brillhart
Vice President, Test

CONTACTS

SANDIA:
Ryan Coe
Albert Schneider

ATA:
Daniel Linehan
Ralph Brillhart
Tom Deiters
Dan Kuriger
Gareth Thomas



ABSTRACT

This report summarizes ATA Engineering, Inc.'s evaluation of the structural dynamic behavior of the maneuvering and sea-keeping (MASK) basin bridge at Naval Sea Systems Command (NSWCCD) Carderock in Potomac, Maryland. A modal test was performed on the bridge which identified two important modes of vibration: vertical bending and torsion at frequencies of 1.56 Hz and 1.68 Hz, respectively. These modes are important for understanding how the bridge structure will interact with a planned wave energy converter support structure. A finite element model of the bridge was constructed and correlated to modal test results, and this correlated model was reduced to provide a simplified version that Sandia National Laboratories can use for simulating the dynamic performance of a wave energy conversion (WEC) device. The bridge finite element model was also used to confirm that the bridge will not be at risk structurally during upcoming WEC performance tests.

TABLE OF CONTENTS

1. INTRODUCTION 1
2. PROJECT OBJECTIVES 2
3. TEST SETUP AND EXECUTION 3
4. ANALYSIS MODEL AND RESULTS 8
5. CONCLUSIONS 19
Appendix A Two-Degree-of-Freedom (2DOF) Bridge Model A-1

LIST OF TABLES

Table 3-1. MASK basin WEC modal test run log.	4
Table 3-2. MASK basin WEC modal test channel table.....	5
Table 3-3. Modal parameters extracted using ATA's AFPoly™ IMAT toolkit for each of the two bridge configurations.	5

LIST OF FIGURES

Figure 1-1. WEC system converts wave motion to electrical energy through a linear generator system.	1
Figure 3-1. The MASK bridge FEM. Arrows indicate modal response accelerometers.	3
Figure 3-2. The six impact locations corresponding to the WEC frame load path to the MASK basin bridge. Location 6 is not seen, but it is analogous to location 5.	4
Figure 3-3. MASK bridge first vertical bending mode, carriage at west end.	6
Figure 3-4. MASK bridge first torsion mode, carriage at west end.	6
Figure 3-5. MASK bridge first vertical bending mode, carriage at mid-span.	7
Figure 3-6. MASK bridge first torsion mode, carriage at mid-span.	7
Figure 4-1. Finite element model of bridge to represent configuration at the time of the modal test.	8
Figure 4-2. First lateral bending mode of bridge at 1.04 Hz. This is a mode of little relevance, since it will not be excited by the WEC.	10
Figure 4-3. First vertical bending mode of bridge at a frequency of 1.57 Hz.	10
Figure 4-4. First torsional mode of bridge at 1.68 Hz.	11
Figure 4-5. Second lateral bending mode of bridge at 3.01 Hz.	11
Figure 4-6. Second vertical bending mode of bridge at 3.13 Hz.	12
Figure 4-7. Second torsional mode of bridge at 3.72 Hz.	12
Figure 4-8. Aluminum WEC interface frame added to bridge model only as rigid elements connecting the load point to the four mounting points.	13
Figure 4-9. Driving point FRF for the WEC frame (based on a mode acceleration analysis).	14
Figure 4-10. Driving point FRF for the WEC frame (based on a mode displacement analysis).	15
Figure 4-11. SDOF model as described by SNL.	15
Figure 4-12. SDOF model as described by SNL but adjusted to account for local flexibility effects.	16
Figure 4-13. Nominal stresses in the bridge structure due to 1 g gravity load in conjunction with a 2.7 kN WEC vertical (down) load.	17

1. INTRODUCTION

The Sandia National Laboratories (SNL) Water Power Technologies group is in the process of developing and demonstrating a wave energy converter (WEC), which can use wave motion to develop electrical energy, using a generator system as shown in Figure 1-1. To evaluate the system's behavior, SNL plans to install the WEC system at the NSWCCD Carderock wave pond MASK basin facility. The WEC will be attached to the bridge that spans the basin, shown in Figure 1-1 at the planned test location. Since the WEC will generate loads from wave movement, there are some concerns about how much the WEC will excite the bridge during the WEC evaluation program. To assess some of the safety and test validity concerns, SNL would like to develop an understanding of the bridge's dynamics so that the interaction between the WEC and the bridge can be more thoroughly evaluated. This report describes the results of ATA's modal test of the bridge, the subsequent analysis approach, and the development of a simplified bridge model.



Figure 1-1. WEC system converts wave motion to electrical energy through a linear generator system.

2. PROJECT OBJECTIVES

ATA set out to perform structural dynamic analysis and testing on the MASK basin's bridge to support the execution of a WEC modal test. The objective of the ATA effort was to conduct numerical and empirical studies to understand the bridge's structural dynamics and deliver a simplified model (i.e., lumped parameter model) of the bridge in all relevant modes for use in subsequent analyses at SNL. SNL also wanted to assess the bridge's strength and its ability to support the WEC hardware and structural supports.

3. TEST SETUP AND EXECUTION

ATA arrived at NSWCCD on the morning of January 13, 2016, to begin test setup. ATA installed accelerometers at the locations denoted in Figure 3-1, using the finite element model (FEM) node labels as location identifiers. The Cartesian coordinate system is identified in Figure 3-1. Not seen in Figure 3-1, two additional accelerometers were installed on the east end of the bridge: one on the longitudinal (X-axis) ground rail, and one on the roller directly above this rail. The purpose of these two additional accelerometers was to determine whether any relative longitudinal motion could be observed, which would affect the FEM characterization of the bridge boundary conditions. All accelerometers were PCB 393B04 seismic accelerometers with a nominal sensitivity of 1000 mV/g.

Test Measurements

ATA used a PCB 086D50 instrumented modal impact sledgehammer to excite the bridge at the various WEC interface locations. These locations are identified in Figure 3-2. A single location was impacted typically six times for each data run, each frame of data was 60 seconds long, and the frames were averaged as part of the postprocessing to frequency-domain data such as frequency response functions (FRFs). All data were acquired with a 24-channel Brüel & Kjær LAN XI data acquisition system. A laptop computer running Brüel & Kjær I-deas® Test software and ATA's IMAT™ software was used to store and process the data.

In total, twelve runs for record (runs 6–17) were obtained: six runs were completed with the MASK bridge carriage located approximately 92 feet from the west end of the bridge, and six runs were completed with the MASK bridge carriage located approximately 7 feet east of bridge mid-span. A test run log, shown in Table 3-1, provides a chronology and description of the test performance. A complete channel table is provided in Table 3-2, outlining the channel configuration used for the data collection system during measurement of all acquired accelerometer and load cell (hammer) data.

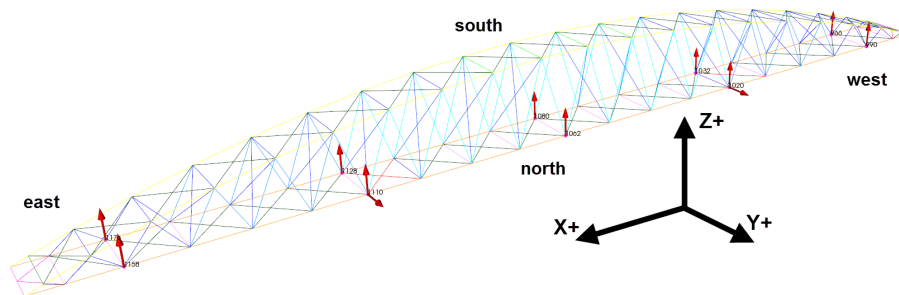


Figure 3-1. The MASK bridge FEM. Arrows indicate modal response accelerometers.

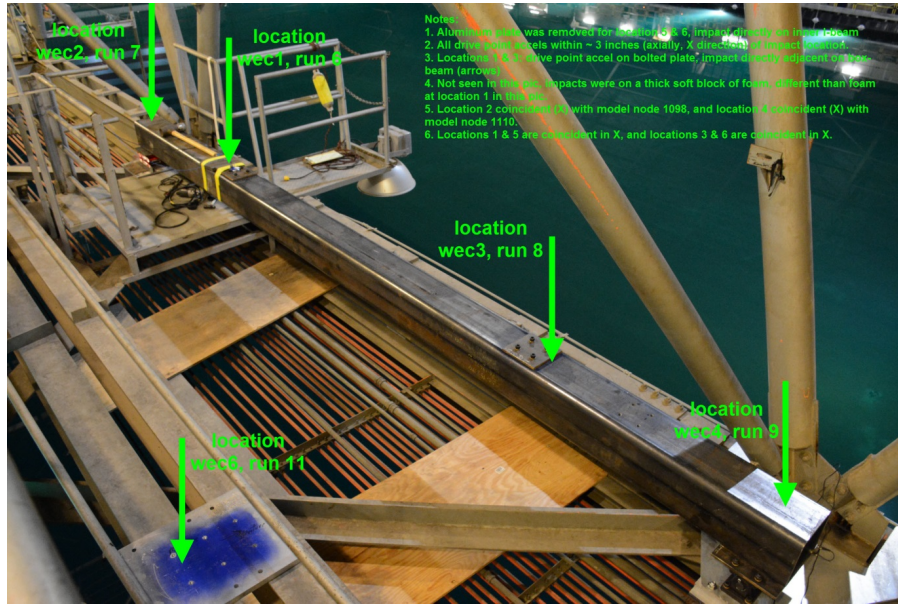


Figure 3-2. The six impact locations corresponding to the WEC frame load path to the MASK basin bridge. Location 6 is not seen, but it is analogous to location 5.

Table 3-1. MASK basin WEC modal test run log.

LAN XI HPF 0.1Hz										
Run #	Date	Start Time	Config	Exc. Type	Filename	Ref Chans	Freq (Hz)	Frame Size (s)	Description	Notes
c1	1/13/2016	13:13	WEC1	i	checkout1.all	2001Z	200	20	Impact sledge, WEC1	
c2	1/13/2016	14:05	WEC1	i	checkout2.all	2001Z	200	20	Detuning ground loops	ratios found to cause DC offset
c3	1/13/2016	14:58	WEC1	i	checkout3.all	2001Z	200	20	Impact sledge w/ DC load cell, WEC1	
c4	1/13/2016	15:48	WEC1	i	checkout4.all	2001Z	200	60	Impact sledge, WEC 1	softer foam
Damage at West end MEC interface beam installed, but not MEC										
1	1/13/2016	16:24	WEC1	i	65402_SNL_WEC_001_wec1.all	2001Z	200	60	Impact sledge, WEC 1	
2	1/13/2016	16:45	WEC2	i	65402_SNL_WEC_002_wec2.all	2001Z	200	60	Impact sledge, WEC 2	
3	1/13/2016	17:03	WEC3	i	65402_SNL_WEC_003_wec3.all	2001Z	200	60	Impact sledge, WEC 3	
4	1/13/2016	17:48	WEC4	i	65402_SNL_WEC_004_wec4.all	2001Z	200	60	Impact sledge, WEC 4	added 3001x to center of carriage prior to run, 1080Z noisy
6	1/13/2016	18:02	WEC1	i	65402_SNL_WEC_005_wec1.all	2001Z	200	60	Impact sledge, WEC 1	repeat to see if same "antiresonance" at 0.4Hz - NEED TO WAIT LONGER FOR DECAY
6	1/14/2016	8:59	WEC1	i	65402_SNL_WEC_006_wec1.all	2001Z	100	60	Impact sledge, WEC 1	added 3002x to rail, moved 3001x to top of wheel
7	1/14/2016	7:06	WEC2	i	65402_SNL_WEC_007_wec2.all	2001Z	100	60	Impact sledge, WEC 2	
8	1/14/2016	7:18	WEC3	i	65402_SNL_WEC_008_wec3.all	2001Z	100	60	Impact sledge, WEC 3	
9	1/14/2016	7:29	WEC4	i	65402_SNL_WEC_009_wec4.all	2001Z	100	60	Impact sledge, WEC 4	
10	1/14/2016	7:50	WEC5	i	65402_SNL_WEC_010_wec5.all	2001Z	100	60	Impact sledge, WEC 5	
11	1/14/2016	8:08	WEC6	i	65402_SNL_WEC_011_wec6.all	2001Z	100	60	Impact sledge, WEC 6	
Damage 7 feet East of midspan, MEC interface beam installed, but not MEC										
12	1/14/2016	8:47	WEC6	i	65402_SNL_WEC_012_wec6.all	2001Z	100	60	Impact sledge, WEC 6	
13	1/14/2016	9:00	WEC5	i	65402_SNL_WEC_013_wec5.all	2001Z	100	60	Impact sledge, WEC 5	
14	1/14/2016	9:13	WEC4	i	65402_SNL_WEC_014_wec4.all	2001Z	100	60	Impact sledge, WEC 4	
15	1/14/2016	9:36	WEC3	i	65402_SNL_WEC_015_wec3.all	2001Z	100	60	Impact sledge, WEC 3	moved 3001 to 3003 prior to run
16	1/14/2016	9:51	WEC1	i	65402_SNL_WEC_016_wec1.all	2001Z	100	60	Impact sledge, WEC 1	
17	1/14/2016	10:06	WEC2	i	65402_SNL_WEC_017_wec2.all	2001Z	100	60	Impact sledge, WEC 2	
EXCITATION TYPE CONFIGURATION										
WEC1 X-Y+ WEC to box beam attachment										
WEC2 X-Y+ box beam to bridge attachment										
WEC3 X-Y+ WEC to box beam attachment										
WEC4 X-Y+ box beam to bridge attachment										
WEC5 X-Y- WEC to I-Beam attachment										
WEC6 X-Y- WEC to I-Beam attachment										
Acel Ground Locations										
3001 10' above wheel base										
3002 10' inboard of wheel base										
3003 1' above wheel base										

Table 3-2. MASK basin WEC modal test channel table.

CH	Gatherbox# - Channe #	Chassis# - Module# - Channe #	SN	Node	DIR	Data Type	EU	Cal mV/EU	Channel Description	CAL DUE DATE
1	1-1	1-1-1	42244	966	Z+	Acceleration	G	995.17	station 1, Y-	05-Aug-16
2	1-2	1-1-2	23361	990	Z+	Acceleration	G	990.69	station 1, Y+	05-Aug-16
3	1-3	1-1-3	42247	1020	Y+	Acceleration	G	992.56	station 2, Y+	02-Aug-16
4	1-4	1-1-4	42249	1020	Z+	Acceleration	G	995.26	station 2, Y+	02-Aug-16
5	1-5	1-1-5	29646	1032	Z+	Acceleration	G	1046.01	station 2, Y-	05-Aug-16
13	1-13	1-2-1	28679	1062	Z+	Acceleration	G	988.31	station 3, Y+	05-Aug-16
14	1-14	1-2-2	42248	1080	Z+	Acceleration	G	997.09	station 3, Y-	05-Aug-16
15	1-15	1-2-3	42245	1110	Y+	Acceleration	G	985.84	station 4, Y+	02-Aug-16
16	1-16	1-2-4	42243	1110	Z+	Acceleration	G	989.25	station 4, Y+	05-Aug-16
17	2-1	1-2-5	29648	1128	Z+	Acceleration	G	1028.56	station 4, Y-	05-Aug-16
18	2-2	1-2-6	28139	1158	Z+	Acceleration	G	999.44	station 5, Y+	05-Aug-16
19	2-3	1-2-7	28137	1176	Z+	Acceleration	G	991.77	station 5, Y-	05-Aug-16
20	2-4	1-2-8	H21234SS	2001	Z-	Excitation Force	IN	0.94	DP LC, WEC interface 1 (X+Y+)	26-Oct-16
21	2-5	1-2-9	42250	2001	Z+	Acceleration	G	992.16	DP Accel, WEC interface 1 (X+Y+)	05-Aug-16
23	2-7	1-2-11	42251	3001	X-	Acceleration	G	995.91	Ground Roller, Axial (X+Y+)	02-Aug-16
24	2-8	1-2-12	42252	3002	X-	Acceleration	G	987.75	Ground Rail, Axial (X+Y+)	02-Aug-16

Test Results

The bridge first vertical bending mode and the bridge first torsion mode were identified for each of the two carriage positions. The frequency and damping results are presented in Table 3-3. The mode shapes are presented in Figure 3-3 through Figure 3-6.

Table 3-3. Modal parameters extracted using ATA’s AFPoly™ IMAT toolkit for each of the two bridge configurations.

configuration	frequency (Hz)	damping estimate (% critical)	mode description
MASK bridge carriage position 1, ~92 feet from west end of bridge	1.56	0.27%	1st vertical bending
	1.69	0.37%	1st torsion
MASK bridge carriage position 2, ~7 feet east of bridge mid-span	1.54	0.31%	1st vertical bending
	1.62	0.60%	1st torsion

Displacement:
Mode 1
Frequency: 1.504 Hz
Damping: 0.200 %Cr
IDLine1: \\cv-fs1\ui\projects\65XXX\65402_Sandia_WEC\Test\atu_hpf\65402_SNL_WEC_009Lwec4_
IDLine4: 65402_SNL_WEC_009Lwec4.atl - Impact\ledge_WEC 4
Contour:
Mode 1
Component: Magnitude
Layer: 1

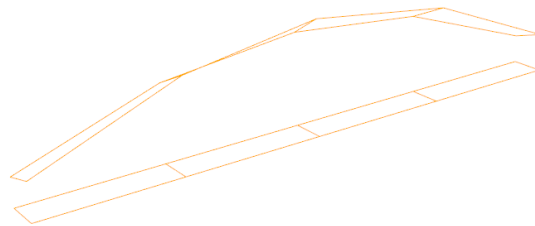


Figure 3-3. MASK bridge first vertical bending mode, carriage at west end.

Displacement:
Mode 2
Frequency: 1.090 Hz
Damping: 0.305 %Cr
IDLine1: \\cv-fs1\ui\projects\65XXX\65402_Sandia_WEC\Test\atu_hpf\65402_SNL_WEC_009Lwec4_
IDLine4: 65402_SNL_WEC_009Lwec4.atl - Impact\ledge_WEC 4
Contour:
Mode 2
Component: Magnitude
Layer: 1

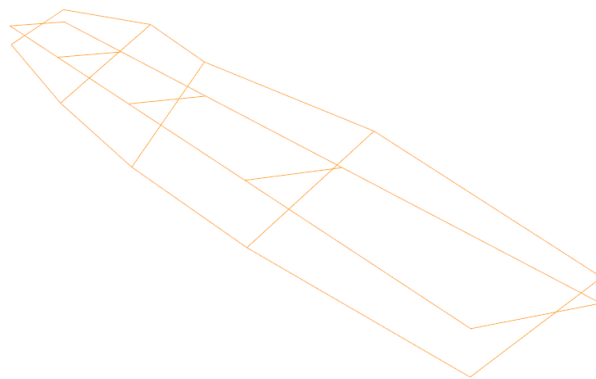


Figure 3-4. MASK bridge first torsion mode, carriage at west end.

Displacement:
Mode 2
Frequency: 1.537 Hz
Damping: 0.313 %Cr
IDLine1: \\cv-811\ui\projects\65000\65402_Sandia_WEC\Test\aru_hpr\65402_SNL_WEC_014L_wec4_
IDLine4: 65402_SNL_WEC_014L_wec4.att-impactledge, WEC 4

Contour:
Mode 2
Component: Magnitude
Layer: 1

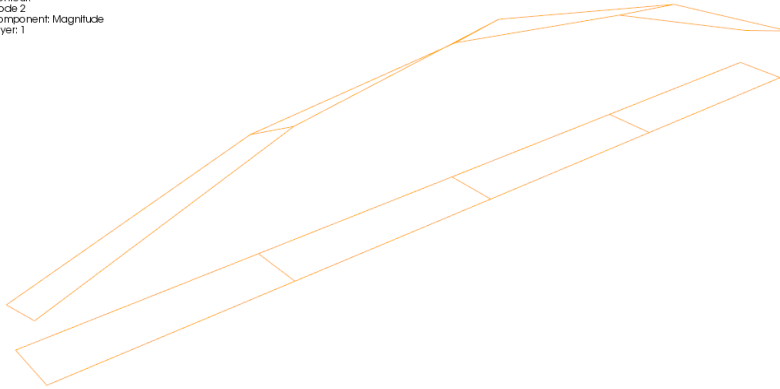


Figure 3-5. MASK bridge first vertical bending mode, carriage at mid-span.

Displacement:
Mode 3
Frequency: 1.623 Hz
Damping: 0.599 %Cr
IDLine1: \\cv-811\ui\projects\65000\65402_Sandia_WEC\Test\aru_hpr\65402_SNL_WEC_014L_wec4_
IDLine4: 65402_SNL_WEC_014L_wec4.att-impactledge, WEC 4

Contour:
Mode 3
Component: Magnitude
Layer: 1

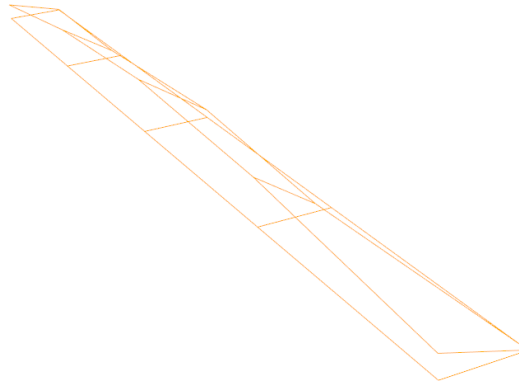


Figure 3-6. MASK bridge first torsion mode, carriage at mid-span.

4. ANALYSIS MODEL AND RESULTS

A bridge FEM was required to meet the objectives of this project because modal testing alone would not be able to reflect the final bridge configuration following the final WEC hardware installation. This was a schedule-driven consideration, in that the modal characteristics of the bridge were needed as early as possible in the program. The bridge model was constructed from hard copy drawings prepared in the 1950s. The preparation of the model was aided by the availability of a SolidsWorks solid model that was prepared in recent times. This model was not used for specific section properties or dimensions but as a comparison tool to make sure that the overall bridge member topology was correct. A beam finite element model was assembled to represent the primary load-carrying members in the bridge, as shown in Figure 4-1.

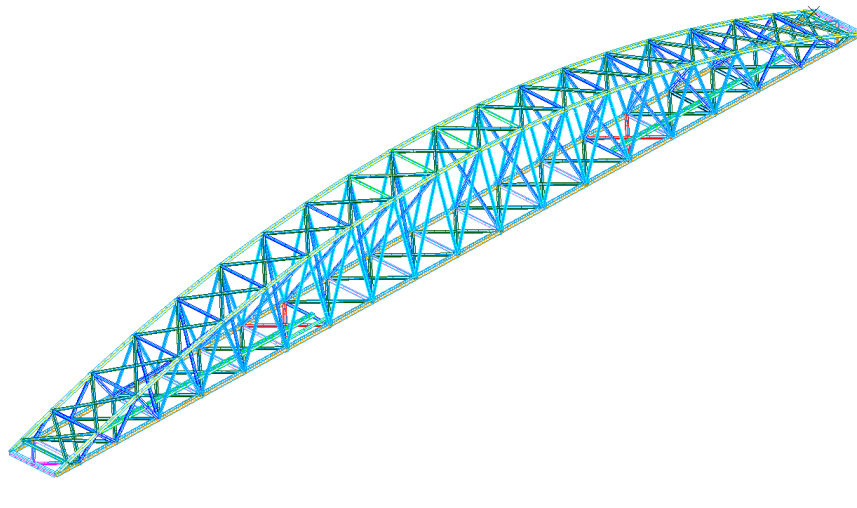


Figure 4-1. Finite element model of bridge to represent configuration at the time of the modal test.

One area of ambiguity that arises in the use of simple 1-D beam elements for a structure such as the MASK bridge is in the member-end connectivity. The use of gusseted, bolted joints to connect the bracing to the top and bottom chords would imply that moments may not be transmitted across the joints. This effect was tested by initially pinning these joints and evaluating the change in the natural frequency of the system. In early debugging versions of the model, it was found that the change in frequency associated with this change in structural behavior was less than 2%. As a result, the pinned-end condition was used for all subsequent analyses.

An all-up bridge weight estimate of 235 T was provided by the project team. Since the weight of the structural model was significantly less than this, it was necessary to modify the steel density of some members to achieve the weight target. It was decided that the weight of only the deck members would be

adjusted since it appeared (from inspection) that the secondary structure making up for the weight shortfall was concentrated on the deck.

A simple stiffness check was undertaken on the model in which two static load cases were considered:

1. A 1 g gravity load case on the whole bridge.
2. The effect of a 33,500 lb carriage located at midspan.

Design analysis results from the 1950s were available for these two load cases and provided the following comparison:

FEA gravity case displacement: 6.50 in. vs. 6.73 in. documented

FEA carriage load case: 0.77 in. vs. 0.80 in. documented

This level of agreement provided confidence that the model did not have significant stiffness errors in it. It should be noted, however, that the stiffness of the model at this stage was based only on the primary structure, and the good agreement with design-stage calculations only confirmed the theoretical accuracy of the model. When these stiffness values were used in a modal analysis, it was found that the first vertical bending mode of the bridge was predicted at 1.2 Hz, whereas the modal test results on the bridge showed this to be at 1.56 Hz. This difference in stiffness compared to the baseline model was attributed to the fact that the secondary structure that contributed to the deck weight shortfall does indeed provide stiffness to overall bridge bending. This assessment provided one of the parameters (deck stiffness) to be used for tuning the model in the correlation effort.

Two other analysis parameters were identified as suitable candidates for use in the correlation effort to match the frequencies of the first two modes of interest, and the shapes of these two modes also provided justification for the additional parameter selection. The flexibility provided by the end trucks was thought to be important, as indicated by the significant motion at the most extreme points in the mode shapes. The other parameter that provides separation in the bending and torsional frequencies is the stiffness of the deck cross-bracing.

The following combination of stiffness values provided the level of correlation believed acceptable for this program:

Modulus of bottom chord members: 60E6 psi (2x steel)

Truck vertical stiffness: 0.4E6 lb/in

Deck cross-bracing modulus: 40E6 psi (1.33x steel)

With these values for correlation parameters, the mode shapes and frequencies shown in Figure 4-2 through Figure 4-7 were predicted.

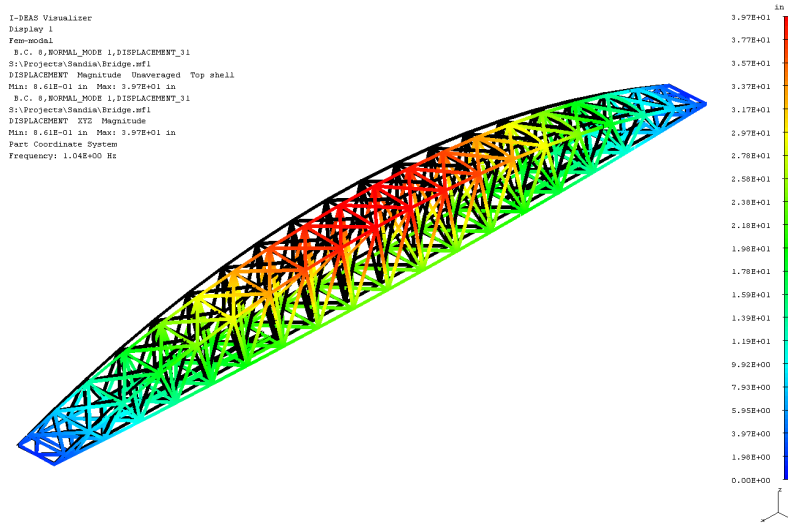


Figure 4-2. First lateral bending mode of bridge at 1.04 Hz. This is a mode of little relevance, since it will not be excited by the WEC.

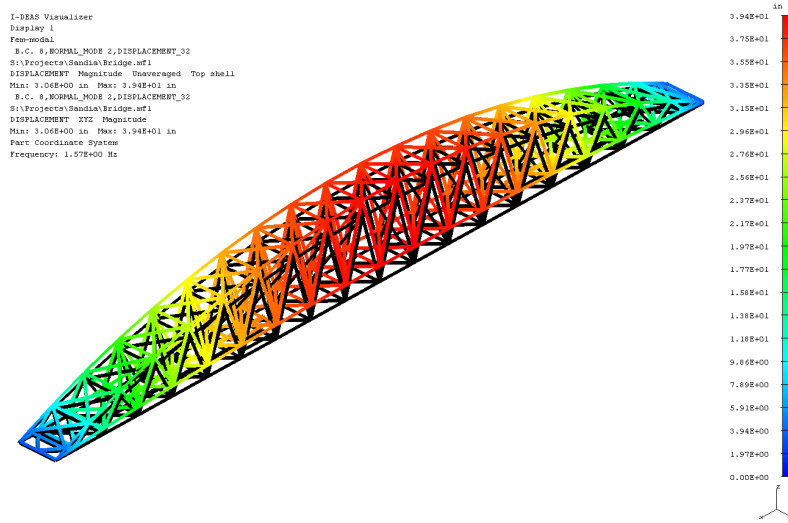


Figure 4-3. First vertical bending mode of bridge at a frequency of 1.57 Hz.

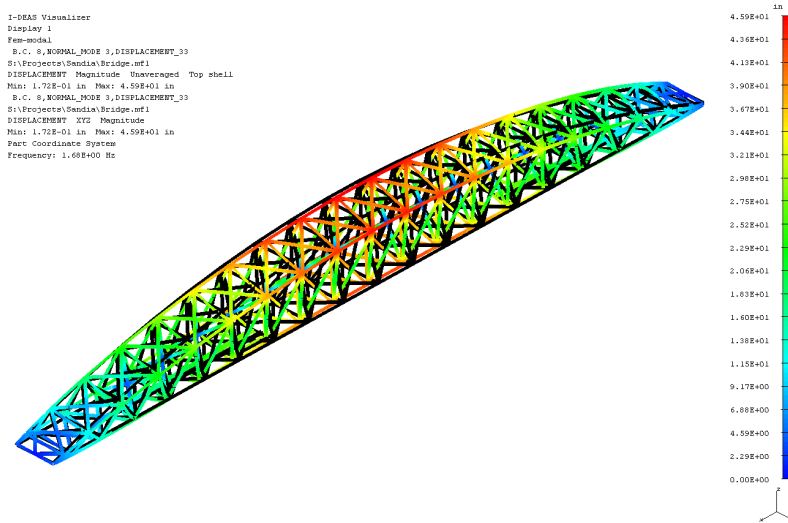


Figure 4-4. First torsional mode of bridge at 1.68 Hz.

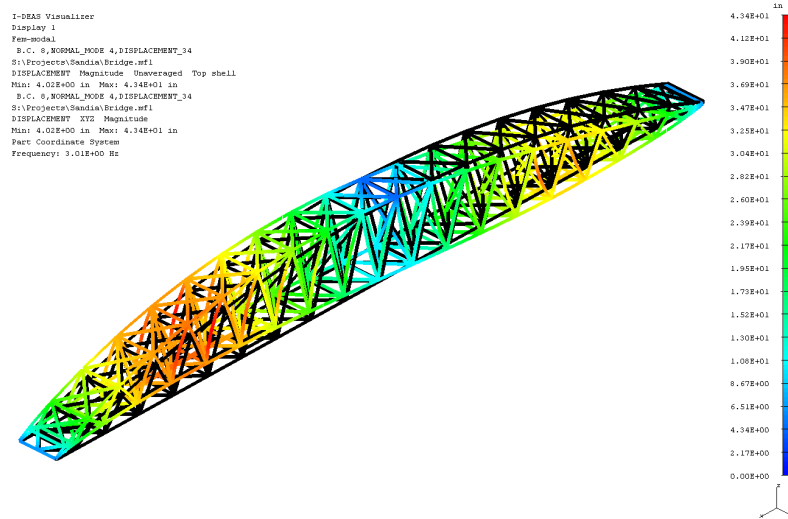


Figure 4-5. Second lateral bending mode of bridge at 3.01 Hz.

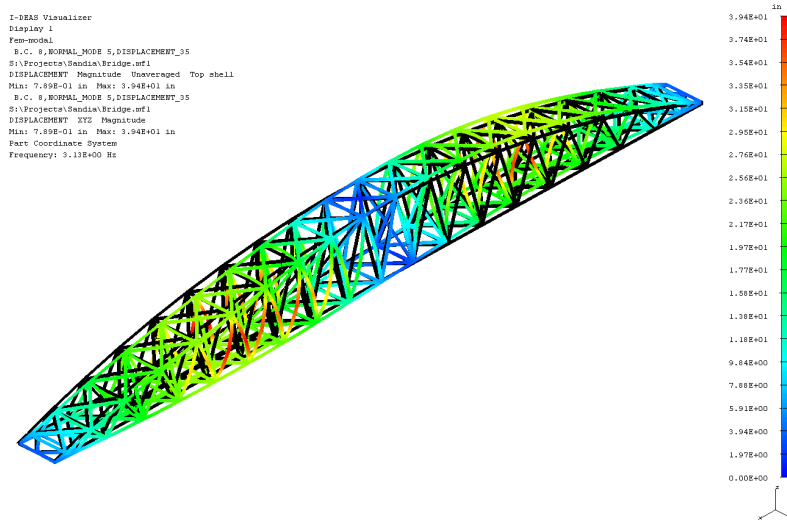


Figure 4-6. Second vertical bending mode of bridge at 3.13 Hz.

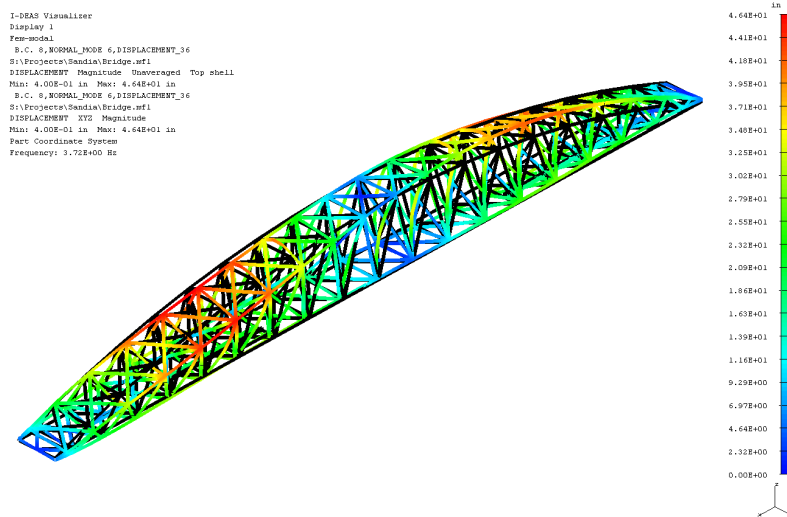


Figure 4-7. Second torsional mode of bridge at 3.72 Hz.

The correlated model used to generate these mode shapes was updated to reflect the presence of the WEC interface frame, as shown in Figure 4-8.

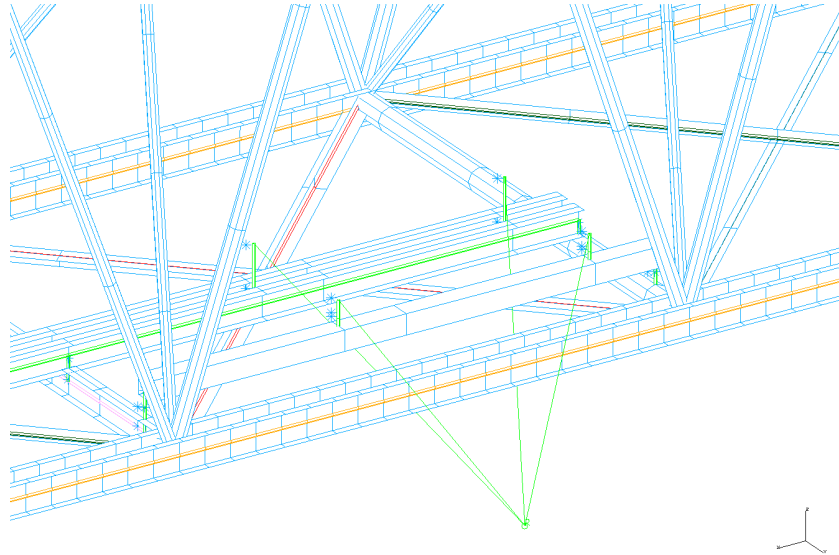


Figure 4-8. Aluminum WEC interface frame added to bridge model only as rigid elements connecting the load point to the four mounting points.

This complete model was then subjected to a forced response analysis in which a unit sinusoidal load was applied to the interface frame in a frequency sweep from 0.1 Hz to 4 Hz. The load point was offset from the middle of the 118" x 128" cantilevered bay of the WEC interface frame in accordance with the WEC model provided by SNL. The dynamic analysis procedure known as mode acceleration was used for this analysis. The resulting displacement response at the loaded node is shown in Figure 4-9.

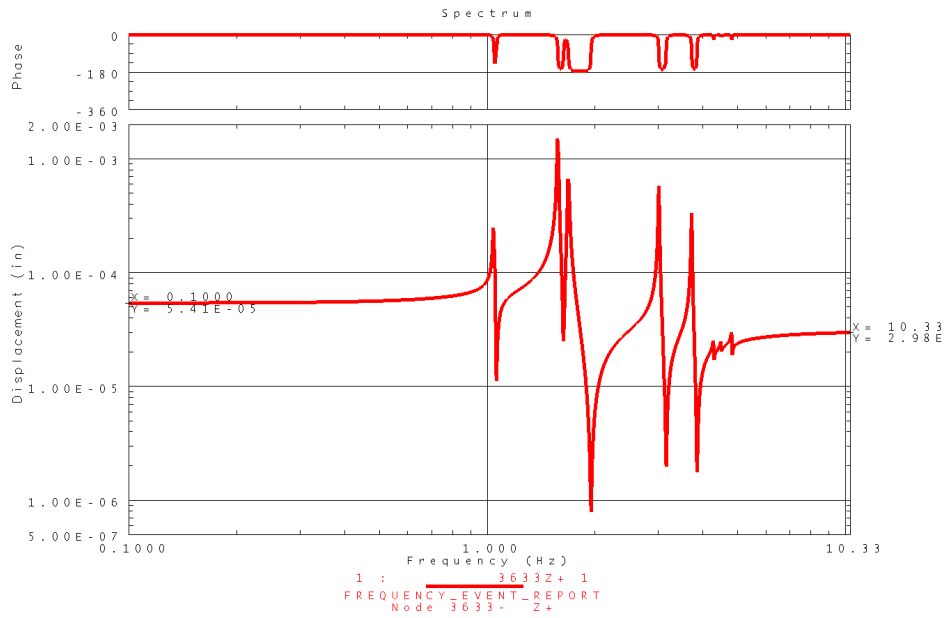


Figure 4-9. Driving point FRF for the WEC frame (based on a mode acceleration analysis).

Of special interest in this plot is the fact that there is almost no dynamic amplification of the excitation force below 1 Hz, as indicated by the horizontal line between 0 and 1 Hz. In other words, the structure is expected to behave in a quasi-static fashion in this frequency range. This should be of particular relevance to control system analysts interested in how the WEC may interact with the bridge.

Another point of interest in the Figure 4-9 plot is the value of the compliance at 0.1 Hz. This value (5.41E-5 in/lb) corresponds to a static stiffness of the system of 18,500 lb/in. This corresponds to the total compliance (or flexibility) of the entire structure, of which there are two components. The first is the expected component reflected in the overall mode shapes. The second component—often overlooked—is due to the local flexibility in the system. In our case, there is significant local flexibility in the bridge structural members that connect the WEC interface frame to the primary members in the bridge truss. To quantify the local flexibility contribution, the forced response analysis was repeated using the mode displacement method. A shortcoming of this approach is that it does not account for local (a.k.a. residual) flexibilities at the load point. Thus, the difference between the two results can quantify the local flexibility. The mode displacement analysis result is shown in Figure 4-10.

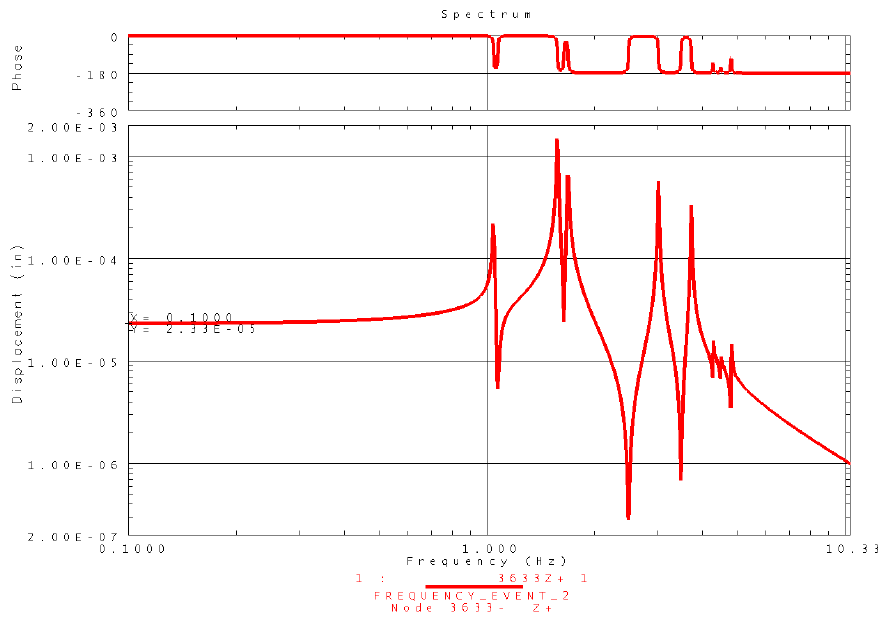


Figure 4-10. Driving point FRF for the WEC frame (based on a mode displacement analysis).

The static flexibility line in this case is at 2.33E-5 in/lb. This indicates that 3.08E-5 in/lb (from 5.41E-5 minus 2.33E-5) of flexibility can be attributed to local (i.e., not modal) effects. In other words, local flexibilities in the bridge are greater than overall bridge bending effects. This is important to point out in reference to the simplified model that SNL has requested, which is discussed next.

The single-degree-of-freedom (SDOF) model solicited by SNL in the statement of work was anticipated to look like that sketched in Figure 4-11.

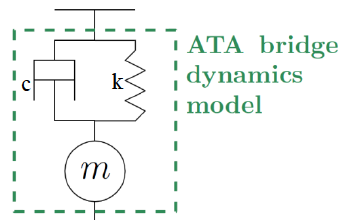


Figure 4-11. SDOF model as described by SNL.

In this case, the combination of m , k , and c that would produce the correct first bending mode frequency is as follows:

$$k = 18,500 \text{ lb/in}$$

$$m = 18500 / (2\pi 1.57)^2 = 190 \text{ lbf.s}^2/\text{in}$$

$$c = 0.0025(2 \times 190 \times 2\pi 1.57) = 9.4 \text{ lbf.s/in}$$

This simple model includes the residual flexibility noted in the above discussion but does so incorrectly, and an alternative model is proposed to correct this.

To reflect the residual flexibility noted earlier, it is important that the spring stiffness be separated into two parts in a modified model, as shown in Figure 4-12.

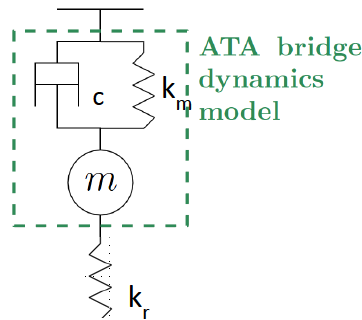


Figure 4-12. SDOF model as described by SNL but adjusted to account for local flexibility effects.

In this case, the combination of m , k_m , k_r , and c that would produce the correct first bending mode frequency and residual flexibility is as follows:

$$k_m = 42,900 \text{ lb/in}$$

$$k_r = 32,500 \text{ lb/in}$$

These springs will combine to produce a combined spring stiffness of 18,500 lb/in as needed at the WEC interface.

$$m = 42,900 / (2\pi 1.57)^2 = 441 \text{ lbf.s}^2/\text{in}$$

$$c = 0.0025(2 \times 441 \times 2\pi 1.57) = 22 \text{ lbf.s/in}$$

In the case that further flexibility (caused by other WEC interface components not already built into the model in Figure 4-12) needs to be incorporated, another spring can be added in series with k_r .

The simplified models presented above consist of SDOF models. Given that there are two modes of vibration in the frequency range of interest, it is expected that a two-degree-of-freedom (2DOF) model would be more representative of the bridge behavior. Such a model is presented in the Appendix A.

In the discussion about residual flexibility, it is important to point out a discrepancy between test and analysis results in this regard. Specifically, a difference in flexibility at excitation point 1 of 5.9 x

10^{-5} in/lb has been recorded. The reason for this difference is not fully understood, but it is believed that the following two factors could be contributing:

- The test predictions may contain inaccuracies because the quality of the modal data at low frequencies (<1 Hz) is somewhat questionable.
- There may be structural flexibilities in the system associated with interface gaps, inadequate bolt torque, and other localized effects. These effects may be present in a lightly loaded structure (i.e., the bridge during modal testing) but may disappear under realistic WEC operation loads.

Because of the uncertainty associated with these effects, it is recommended that sensitivity analyses be undertaken when the simplified bridge model is incorporated into SNL's WEC controls model. If it is found that the results of those control system analyses are sensitive to the interface residual flexibility, further work will be required to quantify the interface stiffnesses more reliably.

Finally, a static strength check was performed on the structure. In this case, a 1 g vertical load was applied in conjunction with a WEC load of 2.7 kN as specified by SNL. This load was also applied statically, as it is believed that a load of this magnitude will be implemented at frequencies below 1 Hz for which the response is predominantly static, as indicated by the FRF of Figure 4-9. The result of the stress analysis is shown in Figure 4-13.

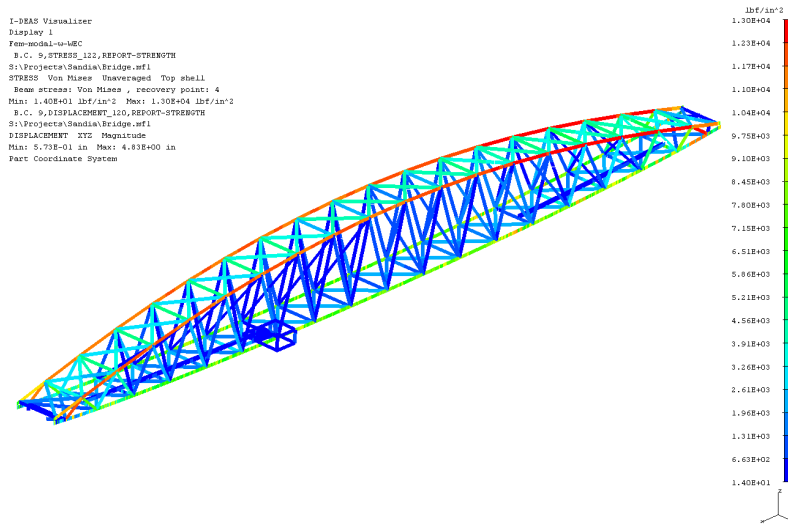


Figure 4-13. Nominal stresses in the bridge structure due to 1 g gravity load in conjunction with a 2.7 kN WEC vertical (down) load.

The stress plot shows that the peak nominal stress (13 ksi) is well within the allowable stress for A36 steel (21.6 ksi per AISC Design Specification¹). Of further assurance is the fact that the main stressing mechanism is the dead weight of the bridge and the WEC-induced stresses seem to be negligible. As was noted in ATA's proposal, the beam model used for this program cannot predict localized stress concentrations in the various members—especially at their end connections—so the stresses being reported are nominal stresses.

¹ AISC 360-10. "Specification for Structural Steel Buildings." American Institute of Steel Construction, June 2010.

5. CONCLUSIONS

Low-level impact loading modal testing was performed on the sea-keeping basin bridge at NSWCCD Carderock in Potomac, Maryland. This test identified two important modes of vibration in the 0–2 Hz frequency range of interest. These modes consist of a bending mode at 1.56 Hz and a torsional mode at 1.69 Hz. These modes needed to be quantified because it is believed that they may affect the dynamic performance of a WEC device that is to be mounted to this bridge for testing.

A finite element model of the bridge was constructed using 1-D beam elements throughout. This model was correlated with the modal test data by tuning the mass and stiffnesses of deck members. These variations confirm that the behavior of the bridge is more complex than that implied by the initial simple model that was based on the primary structure described in design drawings. The tuned analytical model provided very good agreement with the frequencies of the two important modes of vibration.

The finite element model was used to characterize the residual flexibility of the system and to show its importance in the dynamic performance of the bridge at low frequency. This information was not readily available from the test data. A simplified model of the bridge, including residual effects, has been presented so that SNL can use it to reflect the bridge behavior in simulations of their proposed WEC system.

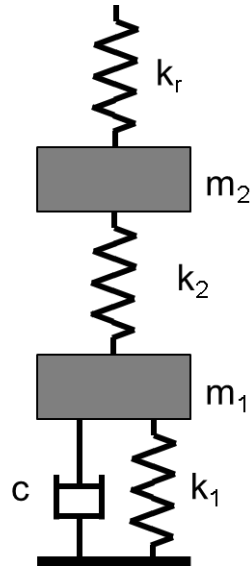
Caution has been raised about the accuracy of the analytical model because of a difference between test and analysis values in total stiffness at the WEC interface frame mounting points. It would be prudent to perform WEC analyses in which the total bridge stiffness is varied from the values listed in this report and the results checked for sensitivity. If the WEC performance is sensitive to the stiffness, then further work will be required to confirm the true value of this stiffness, especially at load levels consistent with the WEC testing.

The nominal stresses in the bridge structure have been found to be well within the allowable stresses typical of this form of construction. These stresses are dominated by dead load effects, with the WEC-induced dynamic loads being very low.

Appendix A

Two-Degree-of-Freedom (2DOF) Bridge Model

A simplified 2DOF model can be represented schematically as follows:



The following values for the variables shown will exhibit the correct dynamic behavior for the bounce and torsional modes of the bridge system (see Figure A-1 for a comparison between the frequency response functions for the simplified model compared to the full bridge model):

$$k_1 = 5.91E6 \text{ lb/in}$$

$$k_2 = 3.57E4 \text{ lb/in}$$

$$k_r = 3.87E4 \text{ lb/in}$$

$$m_1 = 5.60E4 \text{ lb-s}^2/\text{in}$$

$$m_2 = 346.7 \text{ lb-s}^2/\text{in}$$

$$c = 12E3 \text{ lb-s/in}$$

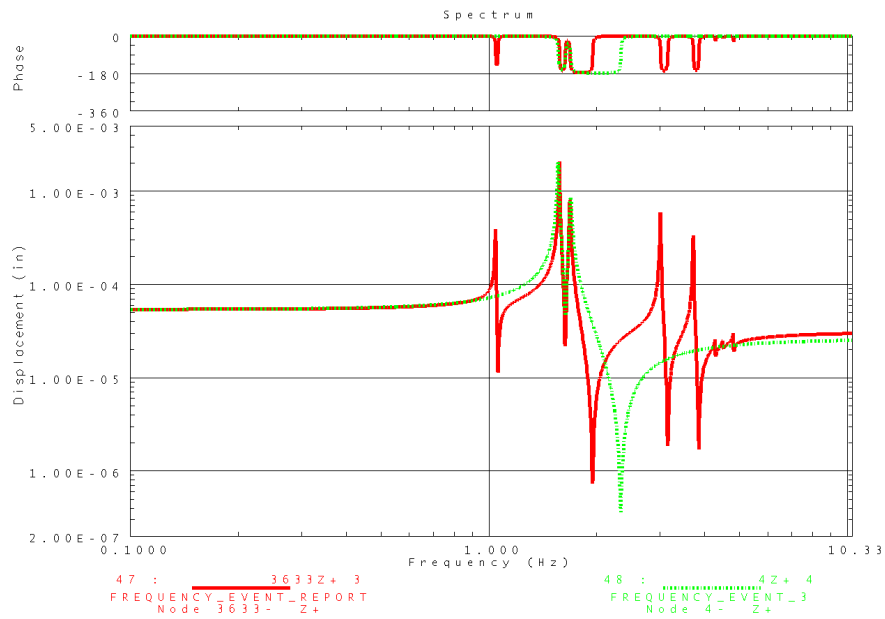


Figure A-1. Comparison of driving point FRF for full bridge model (red) compared with 2DOF model (green).

Three different simplified/reduced models have been presented in this report. A further option that could be the most convenient is the FRF function itself. Depending on how SNL perform their simulations, it may be possible to incorporate the dynamic behavior of the bridge directly by using the FRF as plotted (in red) in Figure A-1. This function can be transmitted in a text-formatted file at SNL's request.

DISTRIBUTION:

1 MS 0899 Technical Library, 9536 (electronic copy)

